

DEVELOPMENT AND IMPLEMENTATION OF OPTICAL
INSTRUMENTATION FOR THE INVESTIGATION OF A LIQUID
CRYSTALLINE RANDOM COPOLYESTER.

by

STEPHEN J. LUKACS JR.

A Dissertation submitted to the
Graduate School-New Brunswick
Rutgers, The State University of New Jersey
in partial fulfillment of the requirements

for the degree of

Doctor of Philosophy

Graduate Program in Chemistry

written under the direction of

Frederick H. Long

and approved by

New Brunswick, New Jersey

October, 1999

ABSTRACT OF THE DISSERTATION

Development and Implementation of Optical Instrumentation
for the Investigation of a Liquid Crystalline Random Copolyester.

by STEPHEN J. LUKACS JR.

Dissertation Director

Frederick H. Long

This thesis represents five years of graduate study in physical chemistry. Three years of which were devoted to the design and construction of modern optical instrumentation, such as second-harmonic and Raman spectroscopy, near field scanning optical microscopy, and time resolved and temperature dependent photoluminescence. The final two years were devoted to using the beforementioned techniques to study the structural and electronic nature and optical phenomena of a main-chain thermotropic liquid-crystalline random copolyester composed of 73% 4-hydroxybenzoic acid (HBA) and 27% 6-hydroxy-2-naphthoic acid (HNA), commonly known as copoly(HBA/HNA) or commercially as Vectra A. This study proved that copoly(HBA/HNA) possesses a strong

nonlinear, or second harmonic, response, a broad band absorption spectrum, and possesses strong photoluminescence. The strong nonlinear response is based on the net additive effect of permanent molecular electric dipoles oriented collinear with the main chain nematic director of the copolyester. Extruded thin films of copoly(HBA/HNA) possess the strong second harmonic response because of resonance effects and the highly ordered orientation of the molecular dipoles. The broad absorption spectrum is based on a distribution of strong π -orbital conjugation strengths and/or lengths of adjoining HNA monomeric subunits. This allows for photoluminescent excitation from the ultraviolet to the near infrared regions, which correspondingly leads to a strong fluorescence emission. The time-resolved relaxation of the fluorescence emission revealed a first-order stretched exponential decay profile. This is indicative of structural and/or energetic disorder inherent within the random copolyester and is based on the distribution of conjugation strengths and/or lengths between the adjoining HNA subunits. Temperature dependent studies of the time-resolved fluorescence revealed additional disorder at high temperatures which follow classical Arrhenius behavior to reveal a fluorescence emission relaxation barrier of 1.357 kcal/mole.

Acknowledgements

Personal

To my wife, Michele,

To my son, Azariah,

to my physics teacher, Binayak Dutta-Roy; in his humble manner filled the vacuum between physical reality and conceptual thought, and revealed that awareness, intent, and consciousness are the only true driving forces of the universe.

for the proper perspective,

“In the temple of Science are many mansions, and various indeed are they that dwell therein and the motives that have led them thither. Many take to science out of a joyful sense of superior intellectual power; science is their own special sport to which they look for vivid experience and the satisfaction of ambition; many others are to be found in the temple who have offered the products of their brains on this altar for purely utilitarian purposes. Were an angel of the Lord to come and drive all the people belonging to these two categories out of the temple, it would be noticeably emptier, but there would still be some men, of both present and past times, left inside. Our Planck is one of them, and that is why we love him.”

Albert Einstein
Essays in Science
Philosophical Library
New York (1934)

and finally, to my teacher, Azariah,

Professional

affiliated with Rutgers Chemistry:

Frederick Long, for being my graduate advisor.

Julian Burton, Milan Pophristic, & Martin Goldman, for putting up with me.

Stephen Cohen, for his help with the second harmonic studies.

Alexi Ermakov, for his help with the AFM.

Jim Elliott, for his help with the IR instrumentation.

Tom Emge, for his help with the X-ray crystallography.

Stephan Isied & Tarek Ghaddar, for their help with the fluorimetry.

and finally Martha Cotter & Nancy Bell, for seeing me through the hard times.

affiliated with industry:

Hyun Yoon & Celanese America, for donating the Vectra samples.

Nicolet, for the help with the FT-Raman.

Bill Cieslik & Hammammatsu, for the use and help of the Streak Camera.

Table of Contents

ABSTRACT OF THE DISSERTATION	II
ACKNOWLEDGEMENTS	IV
PERSONAL.....	IV
PROFESSIONAL	V
TABLE OF CONTENTS	VI
LIST OF FIGURES	IX
LIST OF TABLES	XIII
1. INTRODUCTION	1
1.1. GENERAL FOUNDATIONS	1
1.2. OPTICAL TECHNIQUES AND INSTRUMENTATION	1
1.3. OPTICAL PHENOMENON OF A RANDOM COPOLYESTER.....	3
2. MOLECULAR VIBRATIONS	7
2.1. GENERAL FOUNDATIONS	7
<i>Introduction</i>	7
<i>Light</i>	11
2.2. INFRARED SPECTROSCOPY	12
2.3. RAMAN SPECTROSCOPY	16
3. NONLINEAR OPTICS	26
3.1. MICROSCOPIC FOUNDATIONS	26
3.2. MACROSCOPIC FOUNDATIONS	30
3.3. NONLINEAR INSTRUMENTATION	32

4. PHOTOLUMINESCENCE	35
4.1. GENERAL FOUNDATIONS	35
<i>Introduction</i>	35
<i>Absorption</i>	36
<i>Fluorescence</i>	39
4.2. TIME-RESOLVED FLUORESCENCE	41
5. MICROSCOPY	45
5.1. GENERAL FOUNDATIONS	45
<i>Introduction</i>	45
<i>History</i>	45
<i>Applications</i>	47
<i>Design and Technical Considerations</i>	50
5.2. SHEAR FORCE MICROSCOPY	54
<i>Introduction</i>	55
<i>Probe Assembly</i>	55
<i>Sample to Probe Distance Control</i>	58
<i>Topological and Raster Scanning</i>	60
<i>Future Development</i>	62
6. VECTRA, A LIQUID-CRYSTALLINE COPOLYESTER	63
6.1. GENERAL FOUNDATIONS	63
<i>Introduction</i>	63
<i>Chemistry</i>	64
6.2. OPTICAL ABSORBANCE	68
6.3. MOLECULAR VIBRATIONS	71
6.4. PHASE TRANSITIONS	74
7. NONLINEAR RESPONSE OF VECTRA	78

7.1. GENERAL FOUNDATIONS	78
<i>Introduction</i>	78
<i>Monomeric History</i>	78
<i>Polymeric History</i>	83
7.2. MACROSCOPIC SHG.....	85
8. PHOTOLUMINESCENCE OF VECTRA.....	90
8.1. GENERAL FOUNDATIONS	90
<i>Introduction</i>	90
<i>Stretched Exponential Decay</i>	90
<i>Stretched Exponential Dynamics</i>	92
<i>Decay Profiling and Fitting</i>	95
8.2. PHOTOLUMINESCENCE.....	97
8.3. TIME-RESOLVED PHOTOLUMINESCENCE	102
<i>Experimental</i>	102
<i>Results</i>	104
<i>Discussion</i>	108
8.4. TEMPERATURE DEPENDENT PHOTOLUMINESCENCE	111
<i>Results</i>	111
<i>Discussion</i>	119
9. SUMMARY AND FUTURE WORK	124
REFERENCES	126
CURRICULUM VITAE.....	134

List of Figures

FIGURE 2.1.01. FREQUENCY RESPONSE CURVE FOR A FORCED HARMONIC OSCILLATOR, WHERE THE MAXIMUM ABSORPTION OCCURS AT THE NATURAL FREQUENCY VIA THE IMAGINARY COMPONENT.....	10
FIGURE 2.2.01. THE INFRARED SPECTROMETER.....	15
FIGURE 2.3.01. THE RAMAN SPECTROMETER.....	22
FIGURE 2.3.02. RAMAN SPECTRUM OF 4H-SiC WAFER TAKEN WITH 514.5 NM (2.41 eV) LASER LIGHT AT ROOM TEMPERATURE.	24
FIGURE 2.3.03. RAMAN SPECTRUM OF 4H-SiC WAFER TAKEN WITH 514.5 NM (2.41 eV) LASER LIGHT AT ROOM TEMPERATURE. SAME DATA AS FIGURE 2.3.02, BUT WITH AN EXPANDED VERTICAL AXIS.	25
FIGURE 3.3.01. THE SECOND-HARMONIC SPECTROMETER.	33
FIGURE 4.1.02. JABLONSKII DIAGRAM. THE FATE OF AN EXCITED STATE UPON ENERGETIC EXCITATION.....	38
FIGURE 4.2.01. THE TIME-RESOLVED FLUORESCENCE SPECTROMETER.	43
FIGURE 5.2.01. ARRANGEMENT OF A SFM.....	55
FIGURE 5.2.02. SCHEMATIC OF THE PROBE ASSEMBLY.....	56
FIGURE 5.2.03. BURLEIGH INCHWORM STEP CONTROL CIRCUIT.	57
FIGURE 5.2.04. SAMPLE TO PROBE DISTANCE Z CONTROL CIRCUIT.....	59
FIGURE 5.2.05. XY RASTER SCAN CIRCUIT.	61
FIGURE 6.1.01. CHEMICAL STRUCTURE OF VECTRA A910 OR COPOLY(HBA/HNA).	65
FIGURE 6.1.02. TORSIONAL ANGLES OF THE ESTER LINKAGE OF COPOLY(HBA/HNA).	67

FIGURE 6.1.03. PERMANENT DIPOLES DUE TO STRONG ELECTRON DONATING AND WITHDRAWING GROUPS, RESPECTIVELY, AND ELECTRON DELOCALIZATION WITHIN COPOLY(HBA/HNA).	68
FIGURE 6.2.01. GROUND AND EXCITED STATE OF HBA UPON OPTICAL ABSORPTION.....	69
FIGURE 6.2.02. UV-VIS ABSORPTION SPECTRA OF HBA, HNA, AND COPOLY(HBA/HNA) AT AMBIENT CONDITIONS.	69
FIGURE 6.3.01. INFRARED SPECTRA OF HBA, HNA, COPOLY(HBA/HNA) AT AMBIENT CONDITIONS.....	72
FIGURE 6.3.02. INFRARED AND FT-RAMAN SPECTRA OF COPOLY(HBA/HNA) AT AMBIENT CONDITIONS.....	74
FIGURE 7.1.01. <i>p</i> -BENZOIC AND <i>p</i> -CINNAMIC ACID DERIVATIVES, WHERE D IS THE SUBSTITUTED DONOR GROUP.	82
FIGURE 7.2.01. LINEARLY POLARIZED SECOND-HARMONIC RESPONSE VERSUS CHAIN ORIENTATION FOR 50 μ M COPOLY(HBA/HNA) FILM AT AMBIENT CONDITIONS.	87
FIGURE 7.2.02. VECTORS OF THE DONOR/ACCEPTOR GROUPS IN THE BENZYL AND NAPHTHYL MONOMERS, RESPECTIVELY, OF COPOLY(HBA/HNA).....	88
FIGURE 8.1.01. PROBABILITY DENSITY FOR THE INDICATED STRETCHING COEFFICIENTS ASSUMING A WILLIAM-WATTS LIFETIME τ_{ww} OF UNITY.	94
FIGURE 8.1.02. FLUORESCENCE DECAY PLOTTED AS $\ln(I(0)/I(t))$ VS. TIME, ON A LN-LN SCALED GRAPH.	97
FIGURE 8.2.01. FLUORESCENCE CONTOUR PLOT OF A 75 μ M COPOLY(HBA/HNA) FILM AT AMBIENT CONDITIONS.	98

FIGURE 8.2.02. FLUORESCENCE EXCITATION (A) AND EMISSION (B) SPECTRA FOR A 20 μM COPOLY(HBA/HNA) FILM AT AMBIENT CONDITIONS.....	100
FIGURE 8.2.03. PHOSPHORESCENCE CONTOUR PLOT OF A 75 μM COPOLY(HBA/HNA) FILM AT AMBIENT CONDITIONS.	101
FIGURE 8.3.01. TYPICAL TIME RESOLVED SPECTRUM FROM A STREAK CAMERA OF A 75 μM COPOLY(HBA/HNA) FILM AT AMBIENT CONDITIONS.	102
FIGURE 8.3.02. TYPICAL COPOLY(HBA/HNA) TIME RESOLVED DECAY DATA AGAINST VARIOUS EXPONENTIAL DECAY FUNCTIONS.....	104
FIGURE 8.3.03. TYPICAL COPOLY(HBA/HNA) TIME RESOLVED DECAY DATA LINEARIZED AND FIT AGAINST A FIRST- ORDER STRETCHED EXPONENTIAL DECAY FUNCTION.	105
FIGURE 8.3.04. WAVELENGTH DEPENDENCE OF THE STRETCHING COEFFICIENT α AND THE WILLIAMS-WATTS LIFETIME τ FOR A 75 μM COPOLY(HBA/HNA) FILM UNDER PARALLEL MOLECULAR ORIENTATION/PARALLEL EMISSION POLARIZATION AT AMBIENT CONDITIONS.....	108
FIGURE 8.3.05. PROBABILITY DENSITY FOR COPOLY(HBA/HNA), ASSUMING A WILLIAM-WATTS LIFETIME τ_{ww} OF UNITY.	110
FIGURE 8.4.01. TEMPERATURE-DEPENDENT FLUORESCENCE EMISSION MAXIMA OF A 75 μM COPOLY(HBA/HNA) EXTRUDED THIN FILM.....	112
FIGURE 8.4.02. TEMPERATURE DEPENDENCE OF THE STRETCHING COEFFICIENT α FOR A 75 μM COPOLY(HBA/HNA) EXTRUDED THIN FILM.	115
FIGURE 8.4.03. TEMPERATURE DEPENDENCE FOR THE WILLIAMS-WATTS LIFETIME FOR A 75 μM COPOLY(HBA/HNA) EXTRUDED THIN FILM.	116

FIGURE 8.4.04. ARRHENIUS PLOT OF THE AVERAGED FIVE WAVELENGTH BAND WILLIAMS- WATTS LIFETIME DATA FOR A 75 μM COPOLY(HBA/HNA) EXTRUDED THIN FILM....	117
FIGURE 8.4.05. ARRHENIUS PLOT AND LINEAR REGRESSION OF THE TEMPERATURE DEPENDENT DATA FOR A 75 μM COPOLY(HBA/HNA) EXTRUDED THIN FILM.....	118
FIGURE 8.4.06. GROUND AND EXCITED STATE OF HNA UPON OPTICAL ABSORPTION.	119
FIGURE 8.4.07. GENERATION OF AN ENERGY CONTINUUM IN A RANDOM COPOLY(HBA/HNA) MOLECULE OF 37 MONOMERIC SUBUNITS.....	120

List of Tables

TABLE 2.3.01. PEAK ASSIGNMENTS FOR 4 SI-C.	24
TABLE 5.2.01. BIT STATES TO CONTROL A SINGLE UP OR DOWN STEP IN A BURLEIGH INCHWORM.....	57
TABLE 6.3.01. PEAK ASSIGNMENTS OF THE VIBRATIONAL SPECTRA FOR COPOLY(HBA/HNA).	73
TABLE 6.4.01. PHASE TRANSITIONS OF COPOLY(HBA/HNA).....	75
TABLE 7.2.01. THICKNESS DEPENDENT SECOND-HARMONIC RESPONSE OF COPOLY(HBA/HNA).	89

1. Introduction

1.1. General Foundations

This thesis is the culmination of my five years of graduate study and understanding at the Department of Chemistry, Rutgers University, New Jersey. The first three years were almost entirely dedicated to the design and development of optical techniques and instrumentation. The final two years were dedicated to applying these techniques to a main-chain thermotropic liquid-crystalline random copolyester composed of 73% 4-hydroxybenzoic acid (HBA) and 27% 6-hydroxy-2-naphthoic acid (HNA), otherwise known as copoly(HBA/HNA).

1.2. Optical Techniques and Instrumentation

The classical definition for optic or optical is the interaction and manipulation of light through transparent materials, such as glass or quartz. This perspective led to the development of the light microscope and telescope, which are still in use to date. The modern definition includes the classical definition, as well as any interaction of light with matter. From this more general perspective arises the modern concept of spectroscopy. Spectroscopy is based on the quantum mechanical foundations of the absorption of energy from an incident time-varying electromagnetic field, light, by an atom or molecular species, and then dispersing this energy by various mechanisms. Chapters 2

through 5 detail the theory, design, implementation, and instrumentation of various modern optical, spectroscopic, and microscopic techniques.

Chapter 2 - Molecular Vibrations reveal the interactions of molecular vibrations with light. These interactions provide insight into the molecular and electronic structure of the sample. This chapter covers both infrared absorption and Raman spectroscopy.

Additionally, this chapter covers the detailed construction of the Raman spectrometer within our research laboratory.

Chapter 3 - Nonlinear Optics discusses the microscopic and macroscopic theory of second-harmonic generation with a material. Second-harmonic instrumentation is based on high-powered light sources, such as lasers, incident on a sample. The high-powered laser induces a nonlinear response of the sample, which can reveal structure, polarization, or symmetry effects of the chemical sample. This chapter also covers the detailed construction of a second-harmonic instrument within our research laboratory.

Chapter 4 - Photoluminescence discusses the theory of absorption of light energy to create an excited state within the sample. This excited state can then optically dissipate the high energy by fluorescence or phosphorescence emission to return to the ground state. Photoluminescence has its instrumental foundations based on low-powered incoherent sources, such as bulbs or tubes, but now has applications and usefulness using high-powered coherent laser sources. Time resolved and temperature dependent photoluminescence can reveal an extraordinary amount of information of a chemical

system. Additionally, this chapter details the construction of a time-resolved fluorimeter using a streak camera detector within our research laboratory.

Chapter 5 - Microscopy discusses a modern trend to design and develop light microscopes that break the resolution limits of classical light microscopes to observe molecular systems on the nanometer scale. This resolution power will allow scientists to observe large protein and DNA structures, such as a single viral complex or a cell membrane protein. This chapter also details the construction of an atomic force microscope (AFM), which will eventually lead to a near field scanning optical microscope (NSOM), within our research laboratory.

Therefore, Chapters 2 through 5 discuss the theory, implementation, and instrumentation of modern optical techniques. To be proficient in such instrumentation requires an understanding of classical optics, chemical and molecular interactions with light through quantum mechanics, electrooptical light sources and detectors, analog and digital electronics, data acquisition, and instrument control. The next major section of this thesis, Chapters 6 through 8, use the above optical techniques to study the optical responses of a liquid-crystalline copolyester.

1.3. Optical Phenomenon of a Random Copolyester

Copoly(HBA/HNA), or by its commercial identity, Vectra, is a main-chain thermotropic liquid-crystalline random copolyester composed of 73% 4-hydroxybenzoic acid (HBA)

and 27% 6-hydroxy-2-naphthoic acid (HNA). Samples containing only 4-hydroxybenzoic acid or 6-hydroxy-2-naphthoic acid are not liquid crystalline, therefore these samples are extremely difficult to process and handle on a commercial scale because they do not possess a melt phase transition. The chemical combination of the two monomeric subunits into a single molecular chain creates a phase transition between the glass and liquid phases, called the mesophase. The mesophase greatly lowers the processing temperature of the material to allow for commercial scale production.

Chapter 6 - Vectra, a Liquid-Crystalline Copolyester provides the general application, chemical, and structural, and phase background of copoly(HBA/HNA). Optically, this chapter provides information pertaining to the absorption and vibrational spectral responses, as well as the temperature dependent phase transitions, of the copolyester.

Chapter 7 - Nonlinear Response of Vectra reveals the second-harmonic response of copoly(HBA/HNA). This experimental work confirms prior observations of the large second-harmonic response observed, which is primarily due to resonance effects at 400 nm (3.10 eV) and the net additive effect of bi-directionally aligned permanent electric dipole moments. All of the dipoles are approximately aligned parallel to the nematic director, hence the first-order hyperpolarizability, or the second harmonic response, is strongest when the incident electric field is polarized parallel to the extrusion direction, which is also the direction of the nematic director.

Chapter 8 - Photoluminescence of Vectra presents the steady-state fluorescence and phosphorescence, as well as, the time-resolved and temperature dependent fluorescence of copoly(HBA/HNA). This detailed photoluminescence study of copoly(HBA/HNA) has revealed an enormous amount of structural, phase, and optical response information of copoly(HBA/HNA). Briefly, the copolyester films emit a strong fluorescence emission when excited with less than 1 mW 400 nm (3.10 eV) laser light. The random copolyester exhibits a moderate degree of static energetic and/or structural disorder on the time-resolved temperature independent fluorescence emission, owing to a first-order stretched exponential decay. The 400 nm (3.10 eV) incident light is absorbed by multiple adjoining HNA monomeric subunits connected via varying strength π -orbital conjugation bridges. These varying single bridges extend to the macroscopically observed varying conjugation lengths observed in the fluorescence emission, and are the reason for the static energetic and structural disorder innate to the fluorescence emission. The fluorescence emission is additionally induced, and hence the average emission lifetime decreases, with the introduction of the local HNA rotations of the β phase transition. The β phase transition is seen at room temperature, at which the disorder and lifetime will linearly increase and decrease, respectively. The increasing disorder is due to the introduction of dynamic conjugation strengths and/or lengths from the rotating HNA subunits. The linearly decreasing lifetime exhibits classical Arrhenius behavior owing to the activation energy of 1.357 kcal/mole for the fluorescence emission.

Although the Hoechst-Celanese Corporation has greatly profited from the commercial production of Vectra, which is primarily used to reinforce the strength of common

products, little is known about the photoluminescence of this copolyester. The experiments contained within this thesis should provide useful understanding to the optical properties of copoly(HBA/HNA). In addition to this thesis, the second-harmonic and time-resolved fluorescence results of copoly(HBA/HNA) has been published in the Journal of Physical Chemistry B, (1999), volume 103, pages 6648-6652, with a second paper currently being submitted to JPC B pertaining to the temperature dependent fluorescence emission of copoly(HBA/HNA).

The motivation to study the optical properties of copoly(HBA/HNA) is that copoly(HBA/HNA) is a chemically stable random copolymer that can be used to study resonance stabilization of the polarizability, and the mechanisms and dynamics of a moderately disordered polymer. These studies can provide insight into the chemical and photophysical mechanisms of this organic based copolyester. These studies may prove useful to understanding the photophysics of other polymeric systems, such as poly phenylene vinylene (PPV).

2. Molecular Vibrations

2.1. General Foundations

Introduction

Consider two balls connected by a mechanical spring. If the balls are displaced from the spring's equilibrium position, then there will be an increase in the potential energy of the system. This potential energy, associated with the spring's displacement from its equilibrium position, is the basis of a vibration. The characteristics of the vibration, frequency and amplitude, will depend on the masses of the balls, the initial potential energy, the nature of the spring, and any frictional or damping effects, either internal or external. This scenario can be modeled to the concept of a harmonic oscillator, which can be described by the following equation of motion ¹.

$$m \frac{d^2x}{dt^2} + b \frac{dx}{dt} + kx = 0$$

Equation 2.1.01

where m is the reduced mass of the two balls, b is the dampening coefficient, k is the spring constant and is considered the restoring force of the spring, and finally, x is the displacement from the equilibrium position. Classically, this concept is directly parallel to two atoms connected by a chemical bond.

The above and natural or unperturbed oscillator, described by a homogeneous differential equation, may be affected by an external force. To be effective, this external force must also oscillate as given by the following equation of motion.

$$\frac{d^2x}{dt^2} + 2\gamma \frac{dx}{dt} + \omega_0^2 x = \frac{F}{m} e^{-i(\omega t + \theta_0)}$$

Equation 2.1.02

in which the left side is the natural or unperturbed harmonic oscillator as shown above, where $\gamma = b/2m$, and $\omega_0 = \sqrt{k/m}$, known as the natural frequency of the vibration. The right side is known as the forcing term, in which F and ω are the amplitude and frequency, respectively, of the external force.

An analytical solution can be achieved for the latter differential complex equation.

$$x(t) = \frac{F e^{-i(\omega t + \theta_0)}}{m((\omega_0^2 - \omega^2) - 2i\omega\gamma)} + \text{c.c.}$$

Equation 2.1.03

where c.c. is the complex conjugate. The real displacement of the latter solution would be ¹

$$\text{Re}\{x(t)\} = \frac{F_1}{m} e^{-\gamma t} \sin(\omega_1 t + \theta_o) + \frac{F}{m\sqrt{(\omega_o^2 - \omega^2) + 4\gamma^2\omega^2}} \cos\left(\omega t + \theta_o + \tan^{-1}\left(\frac{2\omega\gamma}{\omega^2 - \omega_o^2}\right)\right)$$

Equation 2.1.04

The first transient term is a solution of the homogeneous differential equation, and will decay asymptotically depending on the initial amplitude F_1 and natural damping γ of the unperturbed vibrating system, in which $\omega_1 = \sqrt{\omega_o^2 - \gamma^2}$, known as the damped natural frequency. The second steady state term is a solution of the inhomogeneous differential equation, and will persist as long as the external oscillation is present and forcing the system. This formalism of the harmonic oscillator will be used as a base of application and understanding in the following chapters of this thesis.

The imaginary analog of Equation 2.1.04 as derived from Equation 2.1.03 would be the same except the cosine function would be replaced with a sine function, which is based on Euler's exponential to trigonometric formula. The real and imaginary components of the displacement correspond to the frequency resonance or phase matching and the magnitude or amplitude of the absorption, respectively. This is shown below in Figure 2.1.01.

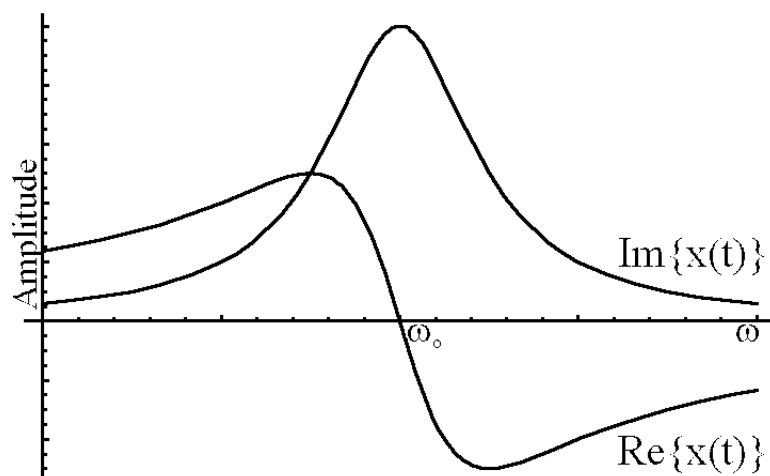


Figure 2.1.01. Frequency response curve for a forced harmonic oscillator, where the maximum absorption occurs at the natural frequency via the imaginary component.

The above treatment reveals fundamental issues prevalent in most spectroscopic techniques. The external force must oscillate with an amplitude, phase, and directionality comparable to that of the natural vibration. The directionality is not obvious in the above equation. However, if the external oscillation is normal to the natural oscillation, then the external force will have no effect on the vibration. This directionality can lead to molecular symmetry and sample orientation in the laboratory frame.

The difference of the natural ω_0 and forced ω frequencies introduces the concept of resonance. As ω approaches ω_0 , then the observed displacement x will reach a maximum, in which maximum resonance is at $\omega = \omega_0$. Conversely, if the incident or forcing frequency is far from the natural frequency, then the forcing term will have little, or zero, effect on the vibration. Finally, if the natural damping γ or the reduced mass m of the system is large, then no vibration will be observed.

Light

Light is a time-varying electromagnetic field. Ideal monochromatic light will be characterized by an amplitude and a single sinusoidal frequency. The relative amplitudes of the electric and magnetic field components are given by

$$E = cB$$

Equation 2.1.05

where c is the speed of light, in SI units. Therefore, for non-relativistic measurements, the electric wave component of light may be considered as the primary external force incident on a vibration. Additionally, since a light field is electric in nature, its influence on the molecule will be electric in nature. This influence is known as the electric dipole in a molecule. An electric dipole, either permanent or induced, will exist within a molecule, in whole or in part, due to neighboring atoms possessing different electronegativities.

A single two atom vibration within a complex molecule can not be observed. This is because all of the atoms are interconnected via various bonds. As atom A pulls, it may cause atom B to push, which would then affect atom C. Therefore, vibrational modes are actually observed, in which individual vibrations are observed as a constructive/destructive set, or superposition, of individual vibrations. The symmetry, or point group, of a molecule, leading to the concept of group theory, is the application of

these superpositions to a particular molecular system. Group theory can provide all of the vibrational modes of a specific molecule, along with any forbidden modes based on sample orientation to the incident light or internally destructive modes.

Infrared (IR) and Raman spectroscopy are two experimental techniques that allow researchers to observe the vibrational modes of a chemical system. The energy of a vibrational mode can simply presented as

$$E = hc\nu$$

Equation 2.1.06

or the energy E of the vibrational mode is the product of Planck's constant h , the speed of light c , and the wavenumber ν is related to the above natural frequency ω by $\omega = c\nu$. The wavenumber is usually expressed in cm^{-1} and can range from 200 to 4000 cm^{-1} , which is directly related to the energy of the vibrational mode ².

2.2. Infrared Spectroscopy

Experimentally, infrared spectroscopy provides a scanning monochromatic source of light incident on a sample. Absorbance of the light will occur at those energies in which the incident light and unperturbed vibrational modes are in resonance. A detector will measure this absorbance at the specific wavenumber of light to produce a 2D plot of transmission versus wavenumber.

The intensity of IR peaks are based on the permanent electric dipole moment of the molecule which is given by

$$\mu_o = \sum_i q_i X_i$$

Equation 2.2.01

where q_i is the charge and X_i is the position of the i^{th} particle. The latter relation is for a fixed and static atomic coordinate system. A molecule vibrating in space can be approximated by expanding the latter equation in a power series via

$$\mu = \mu_o + \sum_j \left[\frac{\delta\mu}{\delta x_j} \right]_0 x_j + \dots$$

Equation 2.2.02

where the 0 subscript denotes the equilibrium position, x_j is the normal coordinate for the j^{th} particle, and μ_o is the former static molecular dipole moment. The intensity A of the IR peak is then directly related to

$$A = \left[\frac{8\pi^2 N_A}{3hc^2} \right] \omega_o \left[\frac{\delta\mu}{\delta x_j} \right]^2$$

Equation 2.2.03

where N_A is Avogadro's number, ω_0 is the natural frequency of the vibration, and $[\delta\mu/\delta x_j]^2$ is the magnitude of the vibration ².

Conceptually, the magnitude of the vibration will depend on the magnitude of the electric dipole induced by electronegative atoms or groups, and its molecule's ability to stabilize this distribution of charge due to the dynamics of a vibrational mode. A vibrational mode on the molecular level is the harmonic motion of the nuclei. As the nuclei move, the electron charge distribution will induce motions of partial positive and negative regions within the molecule. If a molecule can stabilize these regions, usually through charge delocalization, then the vibration's magnitude will be large. Charge delocalization usually occurs with some degree of conjugation through π orbital bonding, such as in carbonyl or phenyl groups. This effect will then be observed as a large IR absorption in the spectrum.

IR spectrometers possess a broad spectrum source of IR radiation. This source is usually a super heated element which approximates a black body radiator producing light in the far infrared regions, usually 400 to 4000 cm^{-1} . This light is collected and focused into a 50% beam splitter to produce a beam intended to pass through the sample and a second beam to act as a reference beam. The two will then be recombined using a chopper, passed through a collimating lens, and then spectrally separated using a scanning monochromator. This processed light is then detected and recorded.

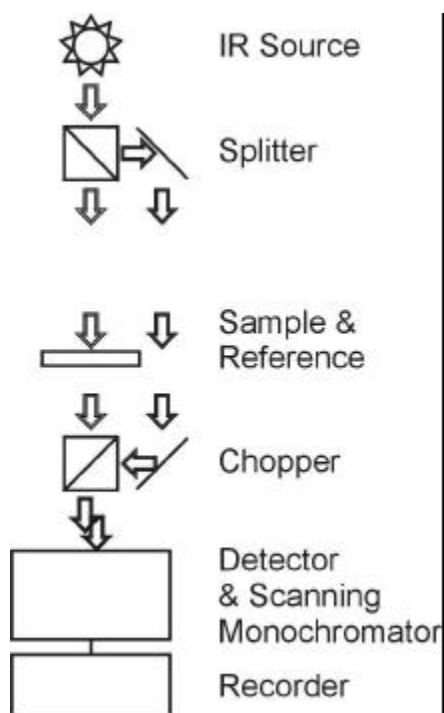


Figure 2.2.01. Configuration of the Infrared spectrometer.

Two types IR spectrometers exist, dispersive and Fourier transform instruments. The above description is the basic scheme of a dispersive apparatus. Dispersive instruments were commercially available first, however, their operation requires some degree of patience and the results may not be completely reproducible. The reason lies in the signal amplitude after the monochromator and the sensitivity of the IR detectors ³.

Fourier transform infrared (FT-IR) instruments possess the same basic scheme as dispersive. However, a scanning Michelson interferometer is placed prior to the beam splitter and the scanning monochromator is removed. Therefore, the full spectrum of the IR source is always incident on both sample and detector. The frequency components of the light, to create the spectrum, are separated by calculating the Fourier transform of the light pulses from the detector. This is called an interferogram. To perform this

frequency separation, the instrument need only know the scanning velocity, and hence the displacement from the central burst position at a particular time, of the mirror within the interferometer^{3,2}. Cooley and Tukey⁴ developed a means, called a fast Fourier transform (FFT), which greatly reduces the computational time required by an instrument to produce the interferogram. This FT-IR system allows a spectrum to be produced within seconds, as opposed to minutes for a dispersive IR instrument. In summary, the major advantages of FT-IR, over dispersive, are its greater sensitivity, rapid data collection, reproducibility, and reliability.

2.3. Raman Spectroscopy

The vibrational modes of a molecule are observed using IR spectroscopy, by direct observation of the permanent electric dipole moment. These same vibrational modes can be observed using Raman spectroscopy, by indirect observation via an induced dipole moment. This induced moment is called the polarizability. This being the case, Raman spectroscopy will often observe and detect those vibrational modes that are symmetry forbidden under IR spectroscopy. Employing both forms of spectroscopy allow for overlapping and complimentary data to be obtained to provide a more complete perspective of the vibrational modes of a molecule³.

In 1928, C.V. Raman and K.S. Krishnan⁵ proposed a scattering experiment similar to the Compton experiment. This technique would scatter visible light, as opposed to X-ray in the Compton experiment. Basically, a nonabsorbing monochromatic source of visible

light incident on a sample will produce scattered light, due to elastic and inelastic interactions of the photons with the molecule. The majority of the scattered light will be from the perfectly elastic interactions, which is called the Rayleigh scattering. This elastic scattering will not produce a shift or change in frequency from the incident beam.

A Raman spectrum is based on the inelastic scattering of the incident photons. A classical approach can be initiated by considering that the electric field component of the incident light E induces a dipole moment in the molecule by

$$P = \alpha E$$

Equation 2.3.01

where α is known as the polarizability of the molecule, and P is the induced dipole moment. Since the electric vector of the light is oscillating, then the polarization will also oscillate with the same frequency. The electric field is given by

$$E = E_0 \cos(\omega_0 t)$$

Equation 2.3.02

substitution will give

$$P = \alpha E_0 \cos(\omega_0 t)$$

Equation 2.3.03

Koenig² provides a simple treatment of the nature of Raman spectroscopy for a diatomic molecule. The polarizability can be approximated by the expansion

$$\alpha = \alpha_0 + (\delta\alpha/\delta x)x + \dots$$

Equation 2.3.04

and the nuclear displacement x from equilibrium is given by

$$x = x_0 \cos(\omega t)$$

Equation 2.3.05

where ω is the unperturbed or natural frequency of the vibration, and x_0 is the equilibrium position. Substitution into the induced polarization and the application of a trigonometry identity yields

$$P = \alpha_0 E_0 \cos(\omega_0 t) + \frac{1}{2} E_0 x_0 \left(\frac{\delta\alpha}{\delta x} \right) [\cos((\omega_0 + \omega)t) + \cos((\omega_0 - \omega)t)]$$

Equation 2.3.06

Therefore, each of the three terms will translate to three observed peaks in a Raman spectrum for a diatomic molecule. The first term is the elastic Rayleigh scattering which derives a zero shift in frequency from the incident monochromatic light. The peak will

have the greatest intensity because the magnitude of $\alpha_0 E_0$ is large comparable to the following terms. If $(\delta\alpha/\delta x) = 0$, then no Raman spectrum is observed. This is the basis of symmetry allowed Raman spectra ⁶.

If $(\delta\alpha/\delta x) \neq 0$, then two peaks will arise from the second and third terms. The resulting frequencies will be a superposition of the natural frequency and the incident light frequency. The second term will shift higher than the incident beam, called the anti-Stokes line, and the third term will shift lower, called the Stokes line. Although the above equation is based on classical mechanics, the Stokes lines will have higher intensity than the anti-Stokes lines. This is because the photons released under anti-Stokes will need to gain energy from the incident beam, and this has a lower probability than the loss of energy for a Stokes line.

In summary, the Raman spectrum arises from the superposition of the natural vibrational frequency with the incident light frequency. Each mode will possess both an anti-Stokes and a Stokes line. Molecules with many vibrational modes will possess a set of peaks, for instance Stokes, for each symmetry allowed mode. The inelastic shifting in energy of the scattered photons will convert to the units of a wavenumber. This Raman spectrum will then directly correspond to an IR spectrum, in which the wavenumber directly relates to the energy of the vibrational mode for a specific molecule. Due to symmetry considerations, certain modes that are forbidden in the IR spectrum will be Raman allowed, and vice versa. Therefore, the application of both techniques can provide a detailed and complete understanding of the vibrational modes of a molecular system.

Raman instrumentation did not fully develop until the advent of lasers, good monochromators, and sensitive detectors. Lasers provide an excellent source of narrow monochromatic light with a well-defined and coherent spatial profile. A laser monochromator can be used to filter any unwanted laser frequencies from the sample. This device is called an optical pre-filter and will filter out light from plasma emissions produced within an ion tube of a laser.

We have employed a Coherent Innova 70 Ar-Kr laser, Figure 2.3.01. This water cooled laser provides our Raman instrument with a dozen frequencies with continuous optical power up to 5 Watts. The optical pre-filter is a Spex 1450. It is designed to remove the plasma lines from the Innova's ion tube without destroying its own internal grating.

This filtered and monochromatic light is then focused onto a sample. Scattered light is collected by reflecting the incident light off the sample. A large focusing lens, with a short focal length, should be used to collect the light. These lens' specifications are critical to designing an instrument which will provide a good signal. A large diameter and a short focal length in the collection lens will ensure an excellent solid angle and collection of a large volume of light. This light is processed by the lens in such a way as to create a collimated beam. This beam is then focused using a second lens, called the collimator, into the entrance slit of a monochromator.

The primary collection lens employed is a 3 in (76.2 mm) diameter lens with a focal point of 3.5 in (88.9 mm). This lens provides an ergonomic working space which is balance by a large collection volume and solid angle. The secondary collimating lens is also 3 in (76.2 mm) diameter with a focal length designed to match the total dispersion of the internal optics of the monochromator, known as the F number, or F#. This dispersion matching ensures that little or no light is lost once the light is focused onto the monochromator slit.

The monochromator for a Raman instrument needs to adequately filter the Rayleigh scattering of the light. This is usually performed with two methods. The first is to insert an optical notch filter specific for the laser light incident on the sample. Optical technology has considerably advanced to provide holographic notch filters, which greatly reduce the intensity of the Rayleigh light without destroying the Raman signals. The only disadvantage to using these filters is one is required for each tunable laser frequency.

The best solution is to employ a monochromator with multiple gratings. We have employed a Spex 1877 Triple Monochromator. The first two gratings are designed to filter out the laser light by a factor of more than six. These filters are tunable to the incident laser wavelength. The light then is focused on a dispersive grating and introduced to a detector array. An array is usually a high resolution 2D array of solid-state photosensitive detectors, such as a charged coupled device (CCD). Most CCD's are also nitrogen cooled to greatly decrease the dark count of the detector, which increases

the array's sensitivity. This array allows a processing unit to simultaneously report a broad range of frequencies. This detector array is usually chosen over scanning the dispersion grating because of reproducibility and measurement speed.

Once the light signal is converted to an electrical signal, via the detector, the spectrum is recorded and processed using a computer. Calibration of the monochromator is performed using gas lamps, such as mercury.

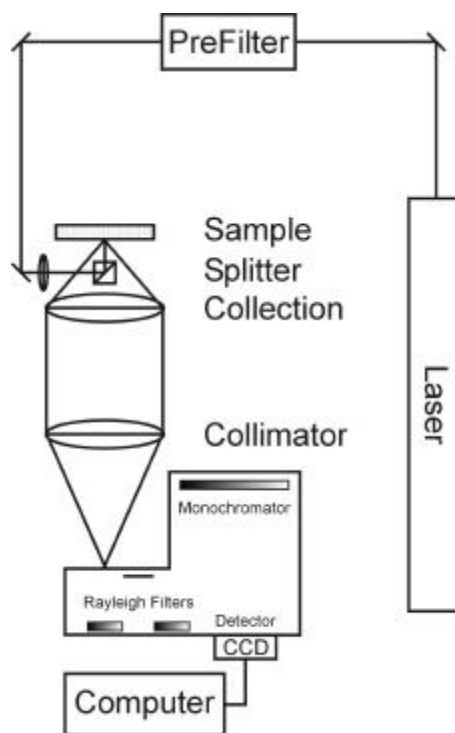


Figure 2.3.01. Configuration of the Raman spectrometer.

Burton *et al.*⁷ used the above Raman instrument to study the spatial characteristics of Silicon carbide (SiC) wafers. The performance of this instrument is superb. The resolution and precision of the Raman shift is less than 1 cm^{-1} , with proper calibration. This resolution allows for the accurate observation of narrow or closely positioned peaks, as seen with the centered peaks at 797.5 cm^{-1} in Figure 2.3.02 and 2.3.03, and at 195.5

cm^{-1} in Figure 2.3.03. This spectral resolution is primarily due to the optical pre-filter, the Rayleigh filters and monochromator within the Spex 1877, and the spatial resolution of the CCD detector array.

The signal intensity of this Raman spectrometer can be clearly seen in Figure 2.3.03. This spectrum did not undergo any signal processing, transformation, or noise reduction. This excellent signal is attributed to the large solid angle of the collection lens, the proper F# of the collimating lens, and the low dark-count, which greatly increases the sensitivity, of the CCD detector. The CCD's sensitivity can detect cosmic rays produced by the sun. These peaks are extremely narrow, typically less than 1 cm^{-1} , and are removed from the spectra using software. For further explanation of this SiC research, refer to Burton *et al.*⁷ for further information.

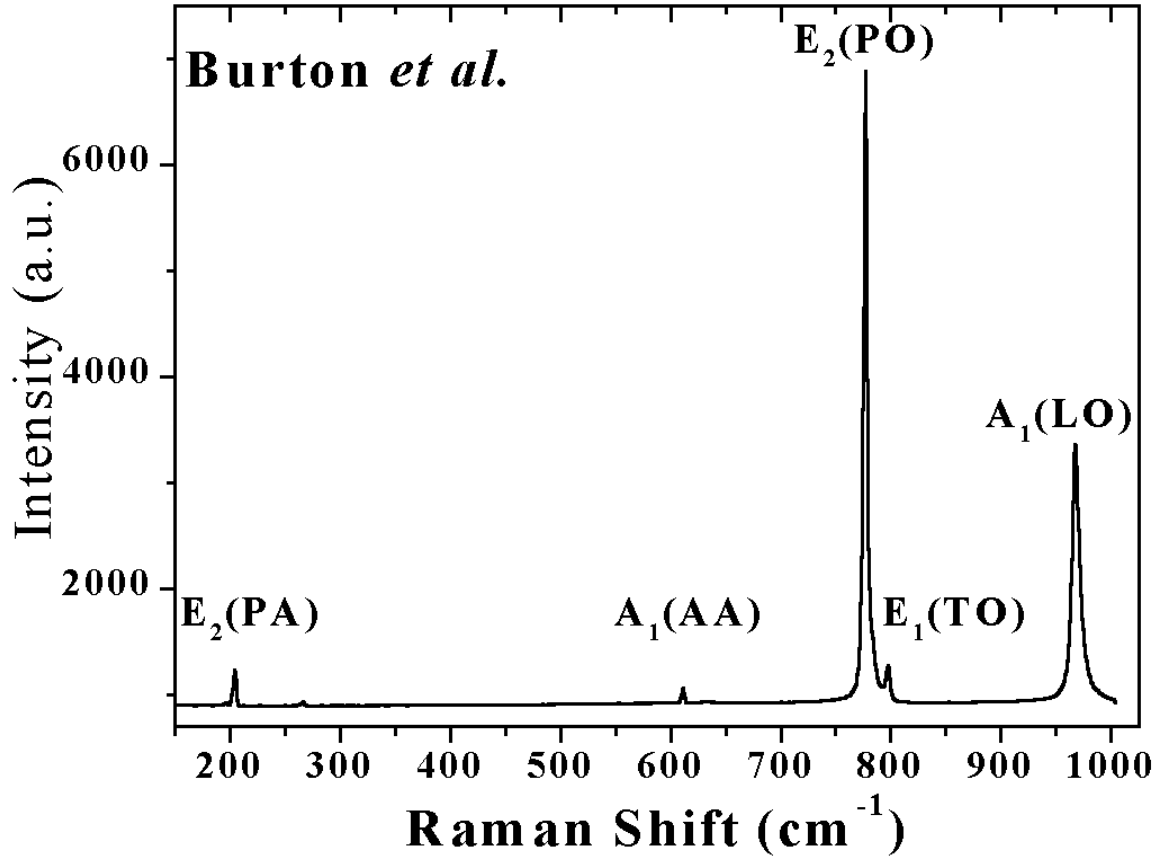


Figure 2.3.02. Raman spectrum of 4H-SiC wafer taken with 514.5 nm (2.41 eV) laser light at room temperature. Courtesy of Burton *et al.* ⁷.

4H-SiC Peak Raman Shift (cm^{-1})	Mode Symmetry
195.5	E_2 planar acoustic
203.5	E_2 planar acoustic
266.0	E_1 planar acoustic
610.5	A_1 axial acoustic
777.0	E_2 planar optic
797.5	$E_1(\text{TO})$ transverse optic
967.0	$A_1(\text{LO})$ longitudinal optic

Table 2.3.01. Peak assignment for peaks shown in Figure 2.3.02 and 2.3.03.

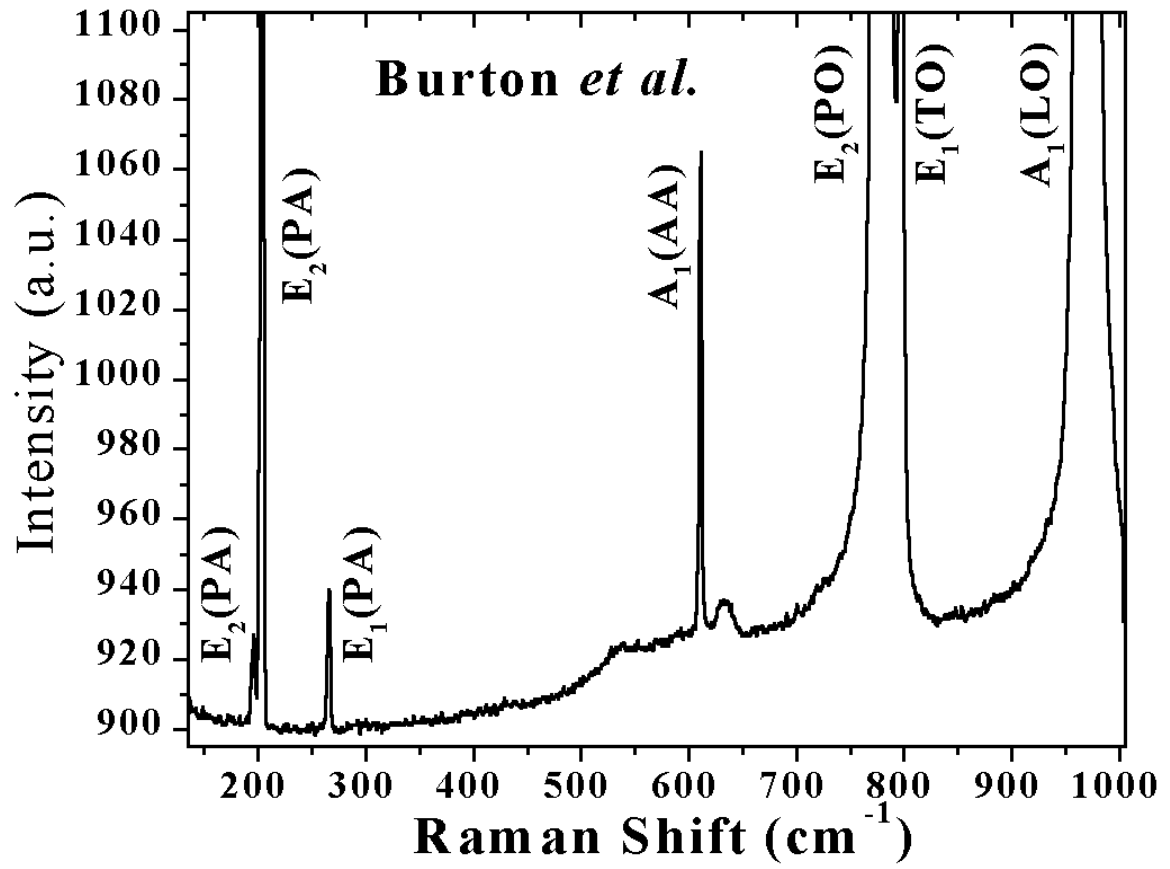


Figure 2.3.03. Raman spectrum of 4H-SiC wafer taken with 514.5 nm (2.41 eV) laser light at room temperature. Same data as Figure 2.3.02, but with an expanded vertical axis. Courtesy of Burton *et al.* ⁷.

3. Nonlinear Optics

3.1. Microscopic Foundations

Light sources, such as lasers, allow the researcher to study the nonlinear responses of materials. These sources possess sufficient power to induce second- and third-order polarizability, without burning transparent or nonabsorbing materials. This chapter is a natural extension of the previous chapter, in which the microscopic response will be understood as a perturbed harmonic oscillator, known as the anharmonic oscillator. This chapter will present both the microscopic, or single electric dipole, response via the anharmonic oscillator and the macroscopic, or bulk, response from the material's electric susceptibility.

An understanding of the nonlinear responses on an electric dipole can begin with the harmonic oscillator as discussed in the previous chapter. The harmonic oscillator was described by the following equation of motion, Equation 2.1.02.

$$\frac{d^2x}{dt^2} + 2\gamma\frac{dx}{dt} + \omega_0^2x = \frac{F(\omega, t)}{m}$$

Equation 3.1.01

This equation will lead to only a linear, or first-order, response of the medium. Any real system will also possess higher, or nonlinear, terms, which will naturally lead to upper

harmonics. High powered external driving forces, such as lasers, will naturally amplify these nonlinear terms to derive an observable response.

Nonlinear responses, or perturbations, are introduced by into the latter equation by expansion through a power series as follows ⁸.

$$\frac{d^2x}{dt^2} + 2\gamma\frac{dx}{dt} + \omega_0^2x + ax^2 + bx^3 + \dots = \frac{F(\omega, t)}{m}$$

Equation 3.1.02

This equation is known as the anharmonic oscillator and the higher-order power terms, $ax^2 + bx^3 + \dots$, are considered to be small in amplitude. The solution of the electric dipole displacement will be in the form of a power series.

$$x(t) = x^{(1)}(t) + x^{(2)}(t) + x^{(3)}(t) + \dots$$

Equation 3.1.03

If Equation 3.1.03 is substituted into Equation 3.1.02 then the hierarchy will follow

$$\begin{aligned} \frac{d^2x^{(1)}}{dt^2} + 2\gamma\frac{dx^{(1)}}{dt} + \omega_0^2x^{(1)} &= \frac{F(\omega, t)}{m} \\ \frac{d^2x^{(2)}}{dt^2} + 2\gamma\frac{dx^{(2)}}{dt} + \omega_0^2x^{(2)} + a(x^{(1)})^2 &= 0 \\ \frac{d^2x^{(3)}}{dt^2} + 2\gamma\frac{dx^{(3)}}{dt} + \omega_0^2x^{(3)} + 2ax^{(1)}x^{(2)} + b(x^{(1)})^3 &= 0 \end{aligned}$$

Equation 3.1.04

in which the first-order, or linear, $x^{(1)}(t)$ solution is Equation 2.1.03. The second-order $x^{(2)}(t)$ solution is solved by moving the $a(x^{(1)})^2$ term to the right side and treating it as a inhomogeneous driving term⁹. The third-order $x^{(3)}(t)$ would follow similarly, however its treatment is not covered further within this thesis.

Allow the electric charge on an electron q and the incident electric field E to be related to the driving force F as given by

$$F(\omega, t) = qE(\omega, t) = qE_1(e^{-i\omega_1 t} + e^{+i\omega_1 t}) + qE_2(e^{-i\omega_2 t} + e^{+i\omega_2 t})$$

Equation 3.1.05

which can be considered as two photons incident on the same point at the same time on the sample. Each photon has its own intensity E_i and frequency ω_i . The second order solution is

$$x^{(2)}(\omega_1, \omega_2, t) = x^{(2)}(0) + x^{(2)}(2\omega_1) + x^{(2)}(2\omega_2) + x^{(2)}(\omega_1 + \omega_2) + x^{(2)}(\omega_1 - \omega_2) + c.c.$$

Equation 3.1.06

where c.c. is the complex conjugate and the sum and difference frequency generations are the first two solutions, the second harmonic generations of each incident frequencies are

second two solutions, and the optical rectification, or zero frequency, component is the final solution. The analytical solution for each of the above terms are provided below 10

$$\begin{aligned}
 x^{(2)}(0, t) &= -\frac{aq^2}{m^2} (g^2(\omega_1)E_1^2 + g^2(\omega_2)E_2^2) \\
 x^{(2)}(2\omega_1, t) &= -\frac{aq^2}{m^2} g^2(\omega_1)g(2\omega_1)E_1^2 e^{-2i\omega_1 t} + \text{c.c.} \\
 x^{(2)}(\omega_1 \pm \omega_2, t) &= -\frac{2aq^2}{m^2} g(\omega_1 \pm \omega_2)g(\omega_1)g(\omega_2)E_1E_2 e^{-i(\omega_1 \pm \omega_2)t} + \text{c.c.}
 \end{aligned}$$

Equation 3.1.07

where

$$g(\omega_i) = ((\omega_0^2 - \omega_i^2) - 2i\omega_i\gamma)^{-1}$$

Equation 3.1.08

In the laboratory a laser can provide a single intense frequency. In this case, we can allow $\omega_1 = \omega_2 = \omega$, and $E_1 = E_2 = E$, therefore the solution simplifies to

$$x^{(2)}(2\omega, t) = -\frac{2ae^2E^2}{m^2} \left(\frac{g(\omega)}{\omega_0^2} + 2g^2(\omega)g(2\omega)e^{-2i\omega t} + \frac{1}{\omega_0^2((\omega_0^2 - \omega^2)^2 + 4\omega^2\gamma^2)} e^{-2i\omega t} \right) + \text{c.c.}$$

Equation 3.1.09

where the first-term is the optical rectification, the second-term is the sum of the sum-frequency and both second-harmonic generations, and the third term is the difference-frequency generation.

3.2. Macroscopic Foundations

The above treatment can be moved into the laboratory, macroscopic, frame by allowing the above single oscillator to be represented as single dipole moment.

$$p = -qx$$

Equation 3.2.01

the bulk, or macroscopic, dipole moment P would simply be a collection of these single oscillators.

$$P = Np = -Nqx$$

Equation 3.2.02

where N is the number of dipoles, or number density, within the incident beam. This macroscopic response can also be understood using the material's dielectric constant κ .

$$P = \epsilon_0(\kappa - 1)E = \epsilon_0\chi E$$

Equation 3.2.03

where ϵ_0 is the permittivity of free space, κ is the dielectric constant of the material, E is the incident electric field, and χ is the effective susceptibility. This susceptibility can be expanded in a power series

$$P = \epsilon_0 (\chi^{(1)}E + \chi^{(2)}E^2 + \chi^{(3)}E^3 + \dots)$$

Equation 3.2.04

Allow the external electric field to be simply represented by

$$E = E_0 \sin(\omega t - kz)$$

Equation 3.2.05

Substituting Equation 3.2.05 into 3.2.04 will yield

$$P = \epsilon_0 (\chi^{(1)}E_0 \sin(\omega t - kz) + \chi^{(2)}E_0^2 \sin^2(\omega t - kz) + \chi^{(3)}E_0^3 \sin^3(\omega t - kz) + \dots)$$

Equation 3.2.06

and applying trigonometric identities follows

$$\begin{aligned} P &= \epsilon_0 (\chi^{(1)}E_0 \sin(\omega t - kz) + \dots \\ &\dots + \frac{1}{2}\chi^{(2)}E_0^2 [1 - \cos(2\omega t - 2kz)] + \dots \\ &\dots + \frac{1}{4}\chi^{(3)}E_0^3 [3\sin(\omega t - kz) - \sin(3\omega t - 3kz)] + \dots \end{aligned}$$

Equation 3.2.07

and therefore the second-harmonic terms are

$$P^{(2)}(0, \omega, -\omega) = \frac{\epsilon_0 \chi^{(2)} E_0^2}{2}$$

$$P^{(2)}(-2\omega, \omega, \omega) = -\frac{\epsilon_0 \chi^{(2)} E_0^2}{2} \cos(2\omega t - 2kz)$$

Equation 3.2.08

the second-harmonic polarizability $P^{(2)}(-2\omega, \omega, \omega)$ must be an odd function, while the cosine function is clearly an even function. This limit forces $\chi^{(2)}$ to be an odd function, which means that the material must be non-centrosymmetric, or does not possess an inversion center. If the material is centrosymmetric then a second-harmonic signal will not be observed; only optical rectification will be observed.

3.3. Nonlinear Instrumentation

Experimentally, second-harmonic generation (SHG) is when two photons of the same frequency are scattered from the material simultaneously. This source of light is easily provided by lasers, for laser light is highly coherent. Laser light is also intense, which allows for the amplification of the second-harmonic response from the material. We have employed a Coherent Innova 400 Ar-Kr multi-frequency laser, Figure 3.3.01. This laser is an optical pump for a Coherent Mira 900, which is a Ti-Sapphire crystal laser. It will absorb the continuous multi-frequency light from the Innova 400 and create pulses

centered at 800 nm (1.55 eV) and 13.6 ns apart. This pulsed light can then be introduced to the sample to create a 400 nm (3.10 eV) second-harmonic signal.

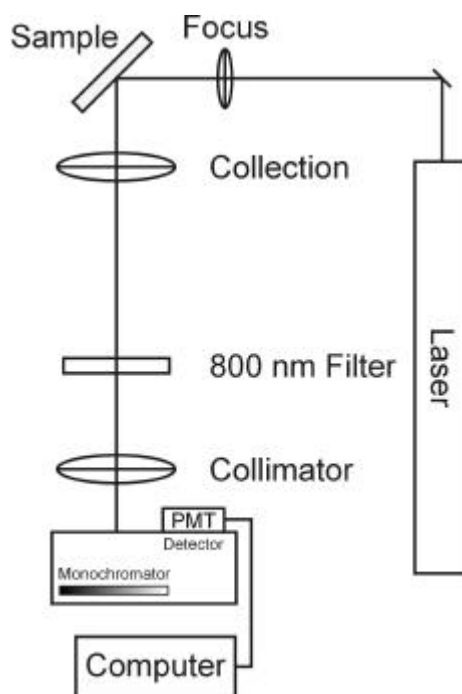


Figure 3.3.01. Configuration of the second-harmonic spectrometer.

This light can be focused using a 1 in (25.4 mm) glass lens directly onto the sample. This light is scattered, as in Raman, and should be collected with a large diameter, small focal length lens. We have employed a 2 in (50.8 mm) diameter, 4 in (101.6 mm) focal length glass lens which is focused into a cylindrical lens. A 6 in (152.4 mm) focal length cylindrical lens is used to focus the light onto the entrance slit of the monochromator. The light is then spectrally differentiated by a grating and reflected to a peltier-cooled photomultiplier tube (PMT) detector. Cooling of the PMT lowers its dark count, and thus increases its sensitivity.

This electrical signal from the PMT is fed into a Stanford Research SR445 preamplifier which amplifies the signal and matches the impedance of the signal for the SR400 photon counter. The SR400 will count the photons incident on the PMT and relay this intensity information into a customized LabView program within an Apple MacIntosh PowerPC. The monochromator can be scanned about the center 400 nm (3.10 eV) signal to ensure that the signal's bandwidth matches that of the 800 nm (1.55 eV) incident light.

4. Photoluminescence

4.1. General Foundations

Introduction

Light is an electromagnetic field oscillating with time and propagating through space. The initial interaction is called absorption and based on the conservation of energy, the matter will increase in energy from the ground state to an excited state. The interaction of light with matter is the basis of optical phenomena, photochemical reactions, and radiatively generated heat.

Energy, in general, can be light or of a purely electric or magnetic nature, such as an electric current. This energy can be absorbed by matter, which then begets an electronically excited state. The excited matter will then dissipate this excited state through either a radiative or nonradiative process. The latter process will generate a new chemical product, thermal energy, or metastable species, as outlined in Figure 4.1.01. The process that has the highest probability of occurring will possess the fastest and lowest energy kinetic response. In other words, the matter will dissipate the excess energy as fast as possible through the processes available to the specific material, local environments, and dynamic states.

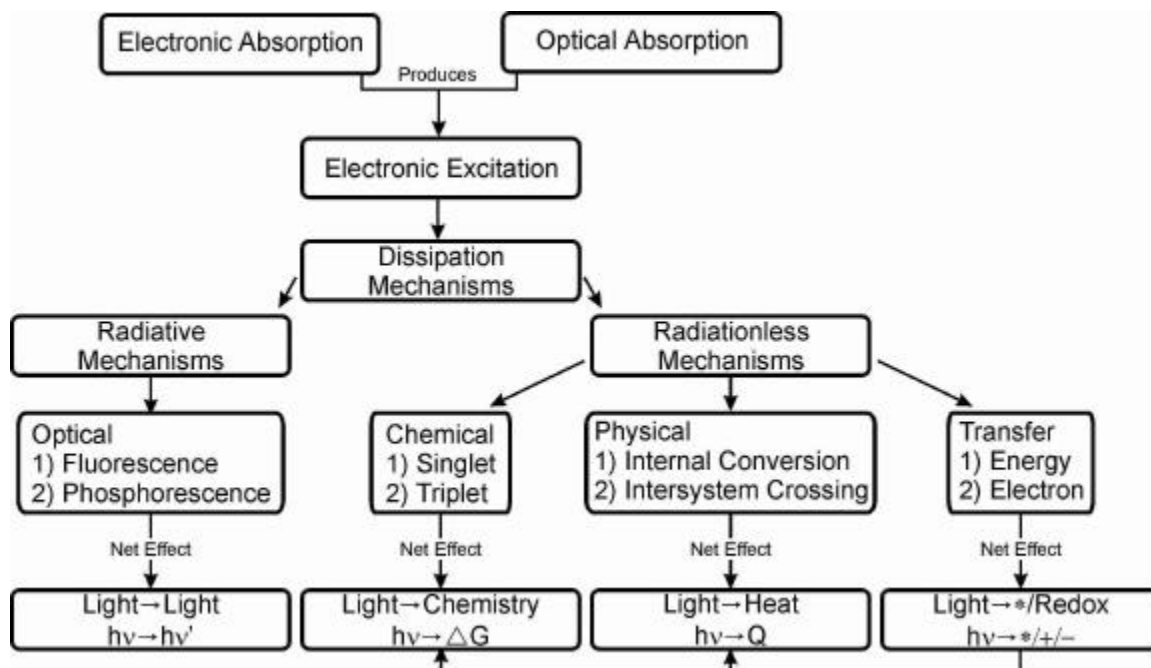


Figure 4.1.01. Processes of energy interaction with matter ¹¹.

Radiative processes will produce photons, or light energy, which will be emitted in the form of photoluminescence. This photoluminescent response can be detected in the form of fluorescence or phosphorescence. The energy of both of these emissions is less than the absorbed energy. This excess energy is usually converted to thermal energy, via internal conversion.

Absorption

An absorption spectrum is produced by introducing broad spectrum light to the sample and measuring the amount of light transmitted by the sample. The absorbance is linearly proportional to the molar absorptivity of the sample, as given by Beer's Law

$$A(\lambda) = \epsilon(\lambda)lc$$

Equation 4.1.01

where ϵ is known as the molar absorptivity, l is the path length of the light beam through the sample, and c is the concentration of the sample in solution. The molar absorptivity is the sample's optical response at a particular excitation wavelength λ . As shown above, it is directly related to the absorption. An absorption spectrometer will scan the wavelengths to obtain an absorption profile. A UV-VIS spectrometer will typically range in wavelength from 200 to 800 nm (6.20 to 1.55 eV).

Absorption of light will excite an electron from the highest occupied molecular orbital (HOMO) to the lowest unoccupied molecular orbital (LUMO). This process will conserve the spin of the excited electron, therefore absorption will derive a singlet excited state. The below Jablonskii diagram, Figure 4.1.02, illustrates this absorption from the ground (HOMO) state S_0 to the excited (LUMO) state S_1 .

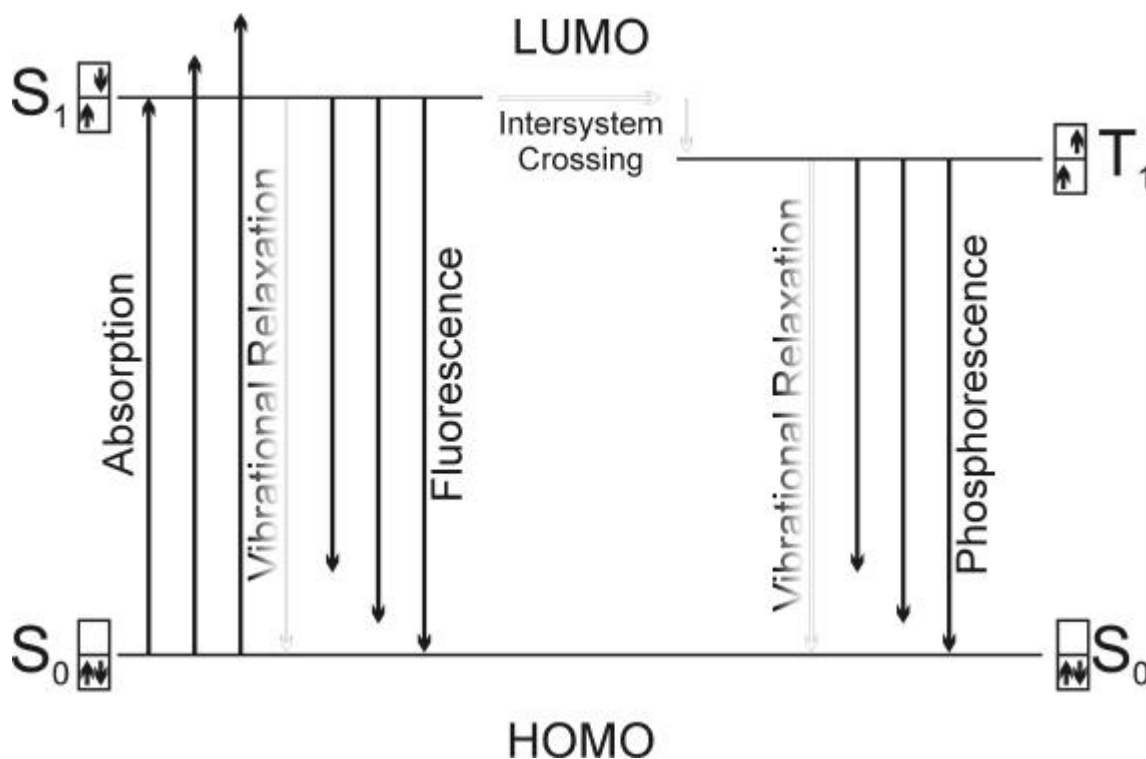


Figure 4.1.02. Jablonskii diagram. The fate of an excited state upon energetic excitation.

The triplet excited state T_1 will typically be lower in energy than the singlet excited state S_1 , as shown. The mechanism of converting from the excited singlet to the triplet is called intersystem crossing. It is a nonradiative process that will be followed by vibrational relaxation to compensate for the lowering of the energy.

The excited electron is in either the singlet S_1 or triplet T_1 state. Once the electron is in an excited state, a number of competing processes will occur. These may be either continued excitation to higher levels, chemical reaction, or one of a number of relaxation processes. For instance, the excited state electron residing in S_1 can be further excited to level S_2 , S_3 , etc., and similarly for the triplet state.

Fluorescence

Relaxation from an excited state to the ground state can proceed by a few processes. In most cases, the fastest optical process is fluorescence, which is the radiative emission of a photon from the singlet excited state S_1 to the singlet ground state S_0 . Phosphorescence is the radiative emission of a photon from the triplet excited state T_1 to the single ground state S_0 . The intersystem crossing, which precedes the phosphorescent emission, is usually a more timely process than fluorescent mechanisms. Therefore, fluorescence will occur at a higher rate and greater probability than phosphorescence. Basically the triplet route is a two step process, the nonradiative intersystem crossing with some loss into vibrational relaxation, followed by the radiative phosphorescent emission.

A completely nonradiative relaxation begins with internal conversion, in which an isoenergetic state of the ground state is produced. The excessive vibrational energy of this “hot” ground state will be carried away by successive molecular collisions. This thermally excited ground state may also lead to thermal reactions. Intersystem crossing is more probable than internal conversion because of the ease of spin inversion.

Inference has been made to the competition of relaxation processes. Once absorption occurs, the extinction of the excited singlet state S_1 will decay with a rate based on ¹²

$$\frac{d[S_1]}{dt} = k_{\text{abs}} - (k_f + k_{\text{isc}} + k_{\text{ic}} + k_{\text{rxn}})[S_1] = 0$$

Equation 4.1.02

where $[S_1]$ is the concentration of the excited singlet state, k_{abs} is the rate of formation of the excited state, k_f is the rate of fluorescence, k_{isc} is the rate of intersystem crossing, k_{ic} is the internal conversion, and k_{rxn} is the rate due to chemical reaction. A similar rate equation will exist for the triplet excited state T_1 where its rate of formation is the loss due to intersystem crossing k_{isc} of the excited singlet state S_1 .

The primary quantum yield is the rate of a specific relaxation process relative to the rate of absorption. For instance, the quantum yield for fluorescence is

$$\Phi_f = \frac{k_f[S_1]}{k_{\text{abs}}} = \frac{k_f}{(k_f + k_{\text{isc}} + k_{\text{ic}} + k_{\text{rxn}})}$$

Equation 4.1.03

or the quantum yield is simply a ratio of rate constants. The lifetime of the fluorescence directly follows from its rate

$$\tau_f = \frac{\Phi_f}{k_f} = (k_f + k_{\text{isc}} + k_{\text{ic}} + k_{\text{rxn}})^{-1}$$

Equation 4.1.04

In summary, an excited singlet state will have a statistically determined fate based on the kinetics of the relaxation and reaction processes. The process that will predominate will be that mechanism that possesses the fastest rate.

4.2. Time-Resolved Fluorescence

Time-resolved fluorescence begins with a pulsed light source. We have employed a Coherent Innova 400 optical pump for a laser oscillator/amplifier system. The Innova will provide 25 W of continuous multiline light for the Coherent Mira 400 Ti:sapphire crystal based oscillator. The oscillator will create mode-locked pulses centered at 800 nm (1.55 eV), a pulse width of approximately 120 fs, a repetition rate of 76 MHz (13.2 nm separation), and 1.2 W average power. The Ti:sapphire of the amplifier, a Coherent RegA 4000, will also absorb energy from the continuous Innova. Pulses from the oscillator will be used to simulate pulse generation in the amplifier to generate highly amplified pulses centered at 800 nm (1.55 eV), a pulse width of approximately 250 fs, a repetition rate of 250 kHz (4.00 μ s separation), and 900 mW average power.

If the lifetime of the system being studied is less than approximately 10 ns, then the Mira can be used as an optical source. For those system's with longer lifetimes, then the RegA will be used. This light is centered at 800 nm (1.55 eV), which can be further modified with Uniwave fs Tripler. This instrument contains a frequency doubler, to produce 400 nm (3.10 eV) light, and a frequency tripler, to produce 267 nm (4.64 eV) light. The tripler will produce femtosecond pulses centered at 267 nm (4.64 eV) from the RegA with an average power output of 50 mW. Tunable second or third harmonic light, respectively, could be generated if the Uniwave is coupled to the Coherent OPA 9400. The OPA will accept the RegA output to produce a tunable wavelength output. The light

from the Mira, RegA, OPA, doubler, or tripler can be focused on the sample. The source chosen for the experiment will depend on the lifetime of the fluorescence, the intensity or average power of the light, and the wavelength required to excite the sample.

The light is focused, Figure 4.2.01, on the sample using a 1 in (25.4 mm) diameter lens with a focal length of 4 in (101.6 mm). The sample will absorb the incident light to produce the excited singlet state S_1 . A finite lifetime will persist for this state until radiative relaxation occurs through fluorescence. This emission is collected using a 2 in (50.8) diameter, 2 in (50.8 mm) focal length lens. This light will pass through a broad spectral range beginning at 420 nm, but filter the incident light, which is at 400 nm. This is to ensure that the laser light does not overpower the fluorescent signal. This filtered light is focused onto the entrance slits of a monochromator, which is then channeled to a Hamamatsu Streak Camera.

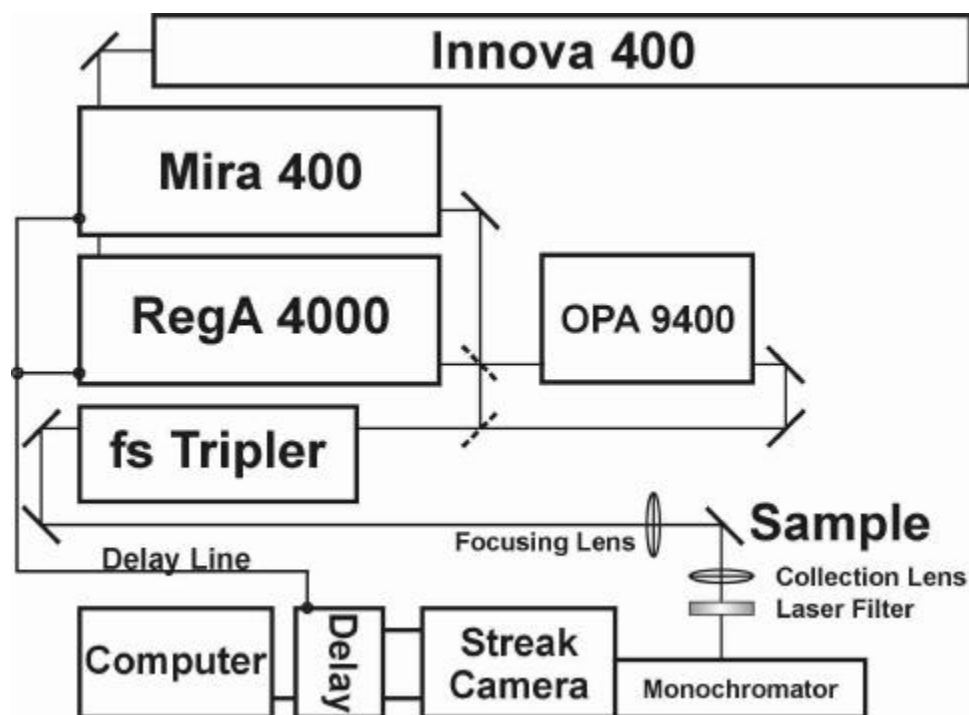


Figure 4.2.01. Configuration of the time-resolved fluorescence spectrometer.

The streak camera is designed to obtain three dimensional data: time, wavelength, and intensity. This data can be sliced at constant wavelengths to provide relaxation profiles. Additionally, the data can be sliced at a constant time, usually zero time, to reveal the fluorescence spectra. In summary, the streak camera is an excellent detector that allows simultaneous retrieval of both time-resolved and wavelength dependent spectra.

The operation of the streak camera is used in conjunction with the attached monochromator. The monochromator will separate the wavelength components of the fluorescence signal in the x-axis. This is automatically registered on the x-axis of the CCD within the camera. The photons from the monochromator are incident on a photoelectric material, which ejects electrons into a vacuum tube upon absorption of photons from the monochromator. A ramping voltage is applied across the tube, in the negative y-axis, and will separate the electrons based on their time of emission from the photoelectric material. This separation directly relates to the time-decay of the fluorescence and is expressed on the y-axis of the CCD within the camera. A single run will last from 5 minutes to an hour, in which each pixel on the CCD will register electron hits. These hits will translate to light intensity. Therefore, the x-axis is the wavelength dependent spectra, the y-axis is the time-resolved spectra, and the z-axis is the intensity dependent on both the wavelength and time.

The range and resolution of the wavelength components will primarily depend on the grating within the monochromator and the x-axis pixel resolution of the CCD. The time resolution will depend on the stability and repeatability of the triggering circuits of the Mira and RegA. The Mira is directly connected to the timing circuits of the stream camera, via the delay line and delay circuitry. These timing circuits control the phase delay of the ramping voltage. Any noise or jitter from the Mira will determine the final time resolution of the streak camera. Either an electrical or optical delay may be employed; determined by which one will provide the least noise or jitter to the streak camera. The magnitude of the ramping voltage will determine the time range of the experiment.

5. Microscopy

5.1. General Foundations

Introduction

The purpose of microscopic instrumentation is to provide researchers with a means to see fine objects beyond the resolving power of the naked eye. The classical, or far-field, light microscope allows researchers to see the agents of disease, primarily down to the size of a single bacterium ($\sim 1 \mu\text{m}$). Viral particles ($\sim 50 - 200 \text{ nm}$), however, eluded researchers until the development of the electron microscope. The electron microscope provided much greater resolution than the optical microscope because of the smaller wavelengths associated with the electron.

History

Near-field (NF) microscopy was first conceived to extend the resolution beyond the minimum optical resolution characterized by Abbe's diffraction limit of $\lambda/2$ found in classical far-field (FF) optical systems, like the light microscope. In 1928, Synge¹³ first proposed the use of narrow apertures and suggested an apparatus that closely parallels modern NF instruments. In 1972, Ash and Nichols¹⁴ first demonstrated the

effectiveness of NF in the microwave region. They were able to achieve a resolution of $\lambda/60$.

The early foundation of visible NF was performed by Fischer^{15,16}. They studied the scattering from narrow holes in a dark field. This work later developed into the first reflection¹⁷ and individual particle plasmons¹⁸. The most currently significant work was performed in 1986^{19,20} by applying a micropipette optical source to the apparatus. This early work paved the way to the modern application of fiber optical sources and fluorescent near-field (NF) probes.

Modern NF instruments stem from primarily three developments, photon tunneling through an evanescent wave, plasmon microscopy, and photon mapping during STM. The first^{21,22,23} was performed by scanning a glass stylus across the sample which is illuminated from the other side by a source such as total internal reflection. The second^{24,25,26,18} was performed by propagating surface plasmons. This technique is extremely sensitive to thin absorbing layers and topographic irregularities. Finally, the third^{27,28} provided almost atomic resolution by detecting the emitted photons during STM from metal and semiconductor surfaces.

This chapter will be concerned with the development of a NF instrument founded on fiber optical sources or detection. This technique is commonly called near-field scanning optical microscopy (NSOM). The basic configuration requires a tapered fiber optic to raster scan the sample to create an image.

Applications

NF techniques and instruments have been developed and adapted to suit a wide variety of materials and optical phenomena. For instance, any electrical or optical response, like photocurrent propagation, photoluminescence, hyperpolarizability, or optical absorption, can be exploited using NF techniques to study the fine structure and response within any material.

Nurmikko *et al.*²⁹ have exploited NF techniques to study the electron-hole pair recombination in semiconductors on the submicron scale. Specifically, they used the high spatial resolution of NF to study the transport properties in heterostructures, such as InGaN. These transport properties are characterized by short-carrier diffusion lengths which were resolved down to the 100 nm scale.

They illuminated the sample with an evanescent light source produced by impinging two laser beams of equal wavelength through a prism, thus causing interference by total internal reflection. The interference of the two beams produced a highly definable evanescent wave that will have a spatial profile dependant on the wavelength of light and the angles of the two incident beams within the prism. This spatial profile is then used to excite the InGaN sample, which dissipates the energy by photoluminescent emission. A fiber optic probe, with a 100 nm aperture, was used to scan the surface and collect the

emission. This NF experiment proved that the electron-hole annihilation is caused by local effects with a range of less than 100 nm.

In an earlier work, Nurmikko *et al.*³⁰ used optical NF in conjunction with shear or atomic force microscopy (AFM). This work proved that microstructural defects, or pinholes, have little impact on the band-edge radiative efficiency of the InGaN layers in thin InGaN/GaN epilayers and quantum wells. The instrument employed allowed them to see the structural defects using AFM while simultaneously monitoring the spatially and spectrally resolved photoluminescence via optical NF.

Most techniques used in FF optical microscopy can be adapted for NF microscopy. For instance, traditional polarized light microscopy has been adapted into a NF instrument to study the birefringent contrast of a polymer containing spherulites³¹. These spherulites are polymer crystallites growing radially from its center. Williamson *et al.*³² studied these structures in polyhydroxybutyrate using the simultaneous combination of AFM topology and optically polarized NF. The resolution of the instrument was found to be 200 nm, and proved that the twisting nature of the ribbon crystallites, as seen in the AFM images, correlates with the birefringent concentric ring structure, as seen in the NSOM images.

Trautman *et al.*³³ were able to retrieve static and dynamic emission spectra of single molecules of 1,1'-dioctadecyl-3,3,3',3'-tetramethylindocarbocyanine (diI) scattered on a polymer bed of polymethylmethacrylate (PMMA). The PMMA acts as an optically inert

medium in which to individually mount the emitting species of diI. The basic procedure involved scanning the sample for a single diI emitter, which is a single molecule of diI, then fix the fiber collector to that position and switch the collection to spectrally disperse and create an emission spectrum. The results of the experiment revealed a shifting of emission maxima and time dependencies, which is attributed to varying local environments. They also found that the single molecule spectral lines were narrower than the multimolecular lines as found in FF experiments. This was attributed to inhomogeneous broadening due to a distribution of molecular environments.

Fluorescence *in situ* hybridization (FISH) is a cytochemical technique used to introduce fluorescent tags into the base-pair sequencing of chromosomes. Fluorescent FF microscopy has been used to study DNA with FISH, however the best reported resolution is 300 nm. Moers *et al.* ^{34,35} used the combination of topological AFM and a FISH-based optical NF instrument to study human metaphase chromosomes. They reported resolutions better than 100 nm using the NF technique. Also, obtaining the simultaneous topological and optical scans of the chromosome allowed for easy identification of the chromosome structure with the location of the DNA probes.

This section has provided a brief overview of the value of NF techniques and instrumentation in research. It can be used in a variety of techniques and modes and most FF techniques can be adapted to a NF analog. The samples may range from semiconductors, to polymers, to lipids, to human proteins and DNA within a single cell.

Most researchers report a resolution of 100 nm, or better, which greatly compliments X-Ray, TEM, SEM, STM, and classical FF microscopy.

Design and Technical Considerations

The technique begins with a standard single-mode telecommunications fiber optic, which has an outer diameter of 125 μm and a 4 to 5 μm inner core. The tip is heated by flame ³⁶, laser ^{37,38}, or electric arc ³⁹ and mechanically pulled to create the taper. Tapers can also be created or enhanced with chemical etching. The taper forces total internal reflection down to a certain diameter and angular limit, at which point strong oscillatory and evanescent emission of light occurs. This emission is further suppressed by coating reflective metals, such as aluminum, along the transverse sides of the taper. The final product will be a tapered fiber optic with a focusing exit aperture with a diameter of 20 - 100 nm.

Betzig ³⁸ was the first to realize that the resolving power rested in the properties of the fiber optic aperture. Betzig reported that the fiber optic may be used for either the source or collection in which he yielded a 12 nm resolution with approximately 10^4 to 10^6 increased intensity from those reported prior to 1991. Additionally, he reported that the image contrast is highly polarization dependent. It was his opinion, that the complexities of taper fabrication and the manner of quantifying resolution is subjective. Further research, both theoretical and experimental, is required to understand the nature of resolution in the nm realm.

Valaskovic³⁷ revealed a number of characteristic taper shapes are created by various heating and pulling parameters. He has shown a time dependent functionality in the heating temperature and the melted viscosity of the fiber during taper fabrication. He has identified six different taper shapes, of which 2 shapes offer the best results for NSOM. Aperture size and incident power are the primary concerns to fiber fabrication. Minor changes in fabrication greatly affect the taper angle or length, which in turn greatly affects the resolution and emitted intensity. The problem most confronted by Valaskovic was that the taper shape, angle, and length are coupled in the fabrication process. He proposed that new nanofabrication techniques should be developed to separate these dependencies to provide better control over the fabrication process.

Coupling a good fiber aperture with the NSOM apparatus requires that the aperture be placed within 10 nm of the sample. This is because the strongly confined light quickly diverges once the light is emitted from the probe tip. The 10 nm tip-sample distance control has been performed by two methods, laser interference⁴⁰, and shear force^{41,42,43,44}. These methods will provide additional surface topography data in an NSOM experiment.

The laser interference, deployed by Keller⁴⁰ *et.al.*, uses the sample reflected interference pattern from the fiber optic aperture. A second fiber optic is used to collect the interfering light from the reflective side of the sample. Keller reports an accuracy of 15 nm or better for distances within 1 μm . Keller deployed this method to circumvent the

problems encountered in shear force regulation. Shear force approach curves are found to be dependent on ambient conditions, such as humidity.

Shear force ^{41,42,43,44} is by far the most widely used method for controlling the tip-sample distance in NSOM. The method employs introducing a resonant mechanical vibration into the rigid fiber optic. The resonance may be that of the fiber or of the sample/stage. If the resonance is introduced into the fiber, the fiber will experience a dampening when approaching the sample. If the resonance is introduced into the sample, then absorption of its resonant frequency will occur when the vibrating fiber approaches the sample. Both techniques deploy piezoelectric transducer (PZT) ceramics to control the distance and introduce and detect the resonant frequencies.

Sample to fiber probe distance can be controlled by exploiting the characteristics and fine control of the raster scanning PZTs. Consider two sets of PZTs, one set to control the sample to probe distance, which will double as XY raster scanner, and the other set to detect the distance from the sample. The latter detection scheme is performed by introducing a mechanically resonant vibration into the PZT as described by Sadrid ⁴⁵. The fiber will act as a forced harmonic oscillator, in which the forcing vibration is introduced electrically into the detection PZT and is near mechanical resonance of the system. The equation of motion is the same as Equation 2.1.02.

$$ma(t) + \mathbf{g}v(t) + kx(t) = F \sin(\mathbf{w}t)$$

Equation 5.1.01

where m is the effective mass, γ is the is damping coefficient, and k is the spring constant of the fiber optic. F is the driving force introduced into the PZT with the vibrational frequency ω . The magnitude of the displacement is

$$X(\omega) = \frac{F / k}{\sqrt{\left(1 - \frac{\omega^2}{\omega_0^2}\right)^2 + \left(\frac{\omega}{Q\omega_0}\right)^2}}$$

Equation 5.1.02

where ω_0 is the undamped natural frequency, $Q = d/\gamma\omega_0 = \omega_0/\Delta\omega$ is the quality of the resonance, where $\Delta\omega$ is the width or the resonance at $1/\sqrt{2}$ of maximum amplitude, and d is the sample distance.

Froehlick⁴⁶ studied the physical response found in NSOM and compared these results against the above equation. Froehlick, and other investigators^{47,48,49}, suggest that the observed decrease in amplitude is a result of viscous damping due to air or a contaminating hydration layer between the probe tip and the sample. This effect would cause γ , and thus Q , to change most radically in the above relation.

Once the fiber is fabricated and is integrated into the NSOM apparatus using tip-sample distance control, then the light source can be applied to the sample. Two methods are deployed in photon collection, classical FF and fiber optic. Classical FF microscope

objectives can be used to collect light from the fiber optic source. The fiber source is essentially a point source with the light diverging as a function of the fiber and sample. A 40X or 100X microscope objective will then act as an excellent light collector because the size of the lens will collect most of the light, even at large oblique angles. The light from the objective is focused onto a pin-hole which is then detected by a PMT.

Fiber optic detection requires fabrication of a lens on the end of the fiber to act as a small objective lens. This system requires careful alignment of the collection fiber with the source fiber or focusing lens. This system basically requires two PZT positioning systems with tip-sample z distance control on the source fiber and intensity detection and feedback coupled to XY positioning of the collection fiber.

The processing of the data may stem from three primary sources, sample topography of the shear force, optical reflection, and optical transmission from the sample. Keller⁴¹ *et al.* showed that there is a direct correlation between the topographical shear force data and the optical reflection data from the sample. Reflection and transmission NSOM can be used for imaging, linear and non-linear spectroscopy, and time resolved experimentation. These methods and the sample preparation are just now being developed to prove NSOM as a valuable research instrument in the future for the nm realm.

5.2. Shear Force Microscopy

Introduction

The shear force microscope (SFM) employed constitutes a shear force probe assembly, a sample stage, electronic circuit controls, and a computer, as shown in Figure 5.2.01. The sample stage can be designed to hold a standard microscope slide or cover slip. The sample will be mounted in the direction of the probe assembly to allow for the probe tip to come in direct and close proximity to the sample.

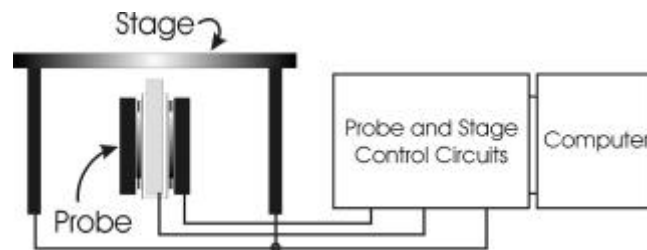


Figure 5.2.01. Arrangement of a SFM.

The control circuits are used to introduce a resonance vibration into the probe and detect the dampened resonant vibration through the sample and stage. This detection of the resonant vibration through the sample is used in a feed-back mechanism to control and measure the sample to probe distance. These circuits are also used to monitor the status of the instrument and collect the data, which is stored in the computer.

Probe Assembly

The probe assembly lies at the heart of the SFM. It constitutes a Burleigh Inchworm, a cylindrical piezoelectric transducer (PZT) ceramic, a shear force probe or stylus, control circuits, and a computer, as shown in Figure 5.2.02.

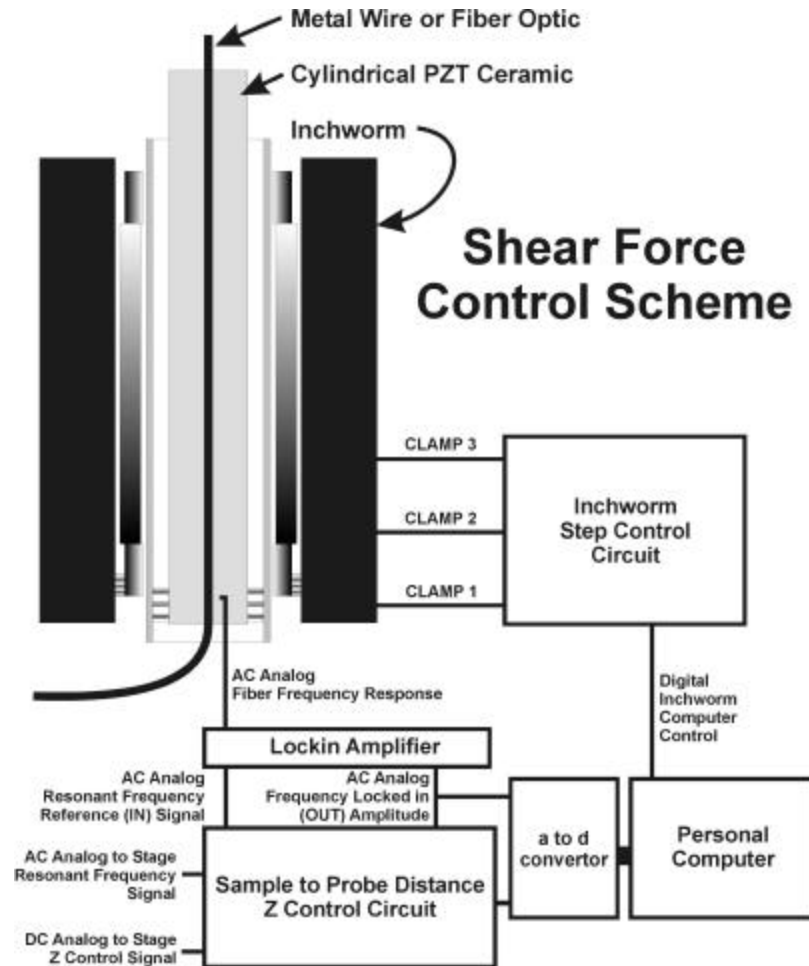


Figure 5.2.02. Schematic of the Probe Assembly.

The construction of a SFM begins with a high-voltage low-noise electrical supply. A minimum voltage of 300 V is required to drive the Burleigh Inchworm. This device is used to allow for coarse distance control between the sample and the probe. The Inchworm is a PZT based device composed of two PZT clamps and a translational PZT. The design allows for discrete submicron steps controllable with a switching circuit as shown in Figure 5.2.03.

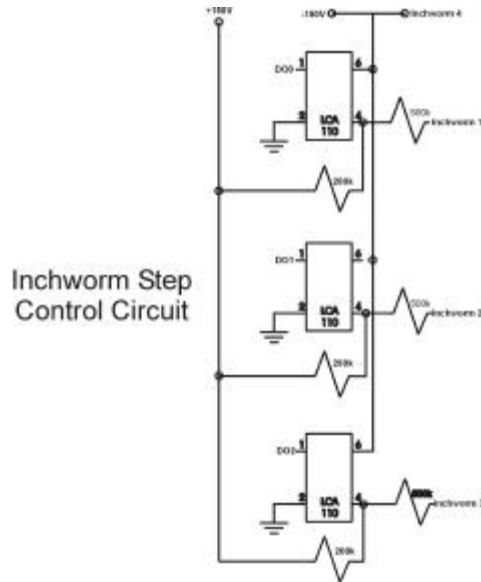


Figure 5.2.03. Burleigh Inchworm Step Control Circuit.

This circuit requires three digital signals, DO0, DO1, and DO2, from a digital control board within a computer. Borland Delphi is an object-oriented pascal language for Microsoft Windows 95 and NT. This language was used to create a custom designed program to control the Inchworm, and the instrument in general. The program is designed to send a series of bit-wise commands to the digital out ports of the control board. The commands and sequence to discretely move the Inchworm up and down are as follows.

Inchworm Step Up bit = state and position of PZT	Inchworm Step Down bit = state and position of PZT
4(100) = clamp 1 & 2	3(011) = clamp 3, release 1 & 2
0(000) = clamp 1, 2, & 3	1(001) = clamp 2 & 3
1(001) = clamp 2 & 3, release 1	0(000) = clamp 1, 2, & 3
3(011) = clamp 3, release 2	4(100) = clamp 1 & 2, release 3
2(010) = clamp 1 & 3	6(110) = clamp 1, release 2
6(110) = clamp 1, release 3	2(010) = clamp 1 & 3

Table 5.2.01. Bit states to control a single up or down step in a Burleigh Inchworm.

This Inchworm system will move approximately 0.3 to 0.4 μm in a single step. The step size can be increased by applying a greater voltage across the PZTs.

The series of Burleigh Inchworms for ultra-high vacuum work provide a translational inner cylindrical shell. A cylindrical PZT ceramic can be mounted within this shell. The NF fiber optic can then, in turn, be mounted within this PZT cylinder, as shown in Figure 5.2.02.

Sample to Probe Distance Control

As stated, the Inchworm provides coarse control of the sample to probe distance. A resonant frequency is introduced into the stage of the instrument to provide fine control of the sample to probe distance. The amplitude of this frequency is closely monitored from the fiber using a lock-in amplifier. This amplitude, in turn, then regulates the z control circuit. This circuit monitors the amplitude of the resonant frequency and will adjust the output voltage the cylindrical PZT ceramic to maintain a constant sample to probe distance. The distance is controlled by adjusting the average output voltage from the circuit. In other words, this scheme is the basis of a feed-back loop. The monitored amplitude is constantly reevaluated and fed-back into the PZT voltage control to maintain a constant distance.

The z control circuit introduces both an AC and DC voltage across the PZT ceramics of the stage. The AC signal is the resonant frequency of the stage to probe coupling. This

coupling is primarily due to acoustic absorption from the stage to the probe. This frequency is first scanned to determine the resonant frequency of the coupling. The circuit is then set to this frequency and sent to the lock-in amplifier for reference, Figure 5.2.04 Section A. Automatic frequency tuning (LCA110 #1), in Figure 5.2.04 Section B, is designed to automatically adjust the resonant frequency of the probe. This feature ensures that as environmental factors slightly change the resonant frequency of the coupling, then the lock-in amplifier is equally compensated. This feature ensures that the sample to probe distance is maintained throughout for extended periods of time.

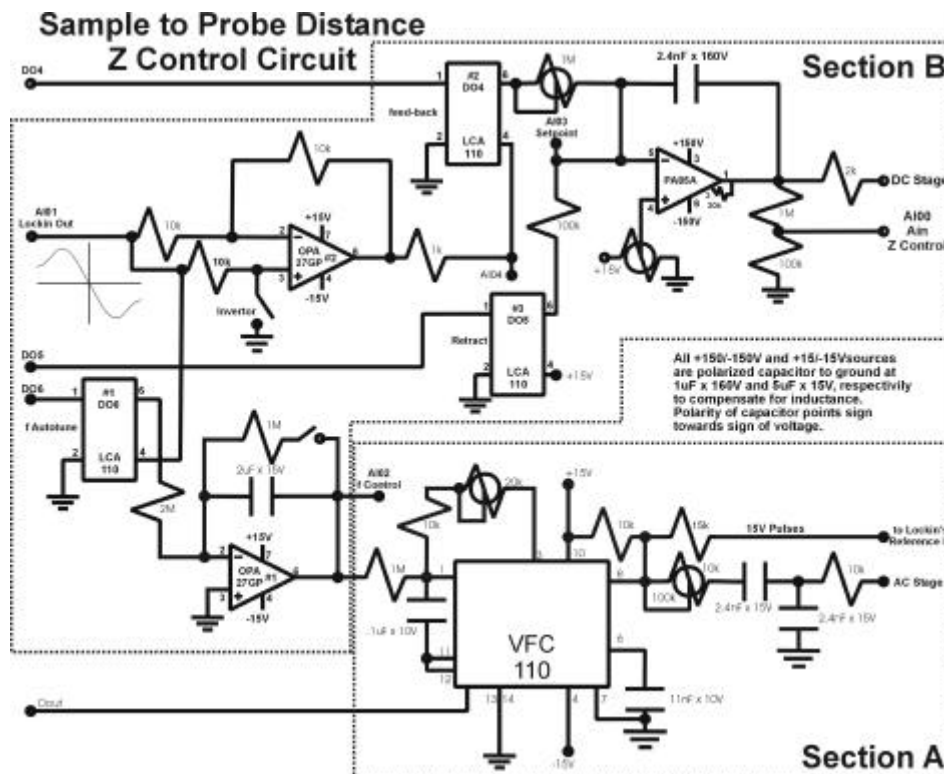


Figure 5.2.04. Sample to Probe Distance Z Control Circuit. Section A contains the tuning circuitry to scan and set the probe's resonant frequency. Section B contains the setting, monitoring, and feed-back control for the sample to probe distance.

The DC voltage controls the length, and thus the sample to probe distance, of the PZT ceramics of the stage. Once the lock-in amplifier possesses the reference resonant

frequency, then automatic frequency tuning (LCA110 #1) is switched off and feed-back (LCA110 #2) is turned on. When LCA #1 is off, then the integrating circuit of OPA27GP #1 remains constant. This has the effect of fixing the frequency of the circuit. This constant frequency is then monitored by the switched on feed-back circuit. The integrating PA85A amplifier will ensure that its output voltage compensates for any phase shifts received from the lock-in amplifier. It performs this compensation by comparing the difference between the set-point voltage (pin 4) and the lock-in signal (pin 5). If a difference exists then the z control voltage will be adjusted to compensate. This compensation will return the difference to zero. The circuit allows the user to adjust the set-point of the amplifier. Its range is from 0 to +15 V, in which 0 V is a far sample to probe distance and +15 V is close. The level of the set-point will be determined by the rigidity of the probe and the detailed desired in the topograph.

Topological and Raster Scanning

Once the sample to probe distance is controlled, then the sample can be scanned to provide a surface topography plot. The stage is easily manipulated in the xy plane to allow for raster scanning of the sample. Scanning is controlled by the computer by using two analog out ports in a digital to analog converter. One of the ports are used to control the x position and the second port is for the y position. The computer program is designed to output analog voltages to these ports. The circuit will simply amplify the analog DC voltages to control the set of PZT ceramics supporting the sample stage. The first set of high-power operational amplifiers will amplify the signal from the computer

by a factor of ten. The second set of operational amplifiers will simply invert the latter voltage. This inverted signal will be connected to the opposite, or negative, side of the PZT ceramics on the stage.

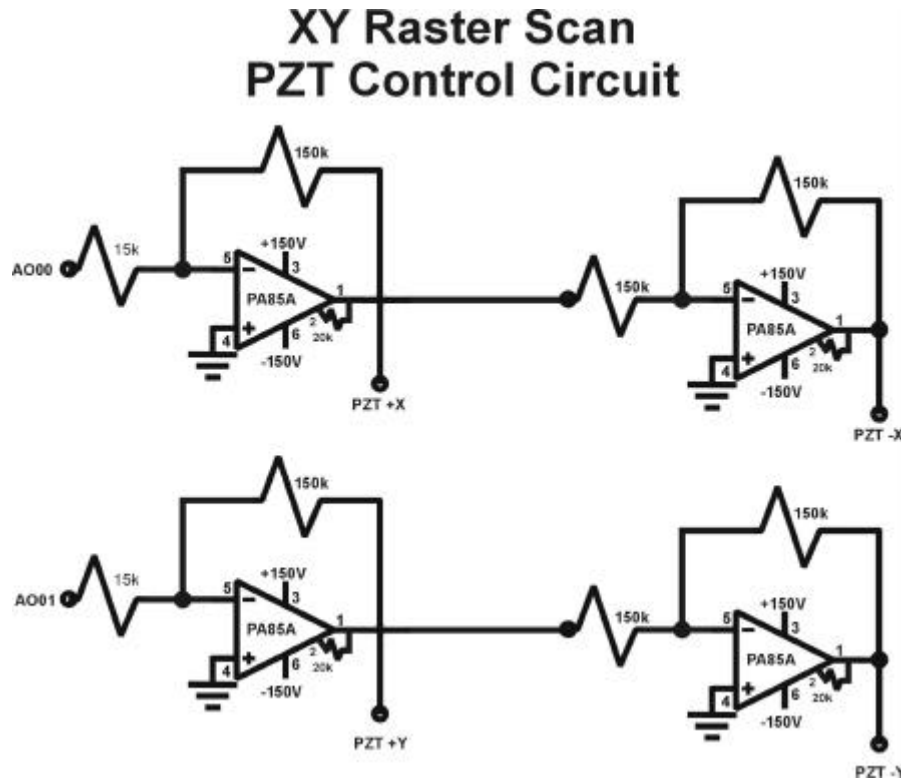


Figure 5.2.05. XY Raster Scan Circuit. Each of the two circuits are designed to independently control the x and y positions of the microscope stage.

The A_{in} output of Figure 5.2.04 can be connected to an analog in port and converted to a digital signal in a computer. This value will possess a range from -10 to $+10$ V and can be directly stored as surface topography data of the sample. It is this output that Keller *et.al.*⁴¹ showed to correspond to the reflected optical response of the sample at any single point. Each point can then be raster scanned using the circuit in Figure 5.2.05.

The computer will know the output voltages corresponding to the x and y positions of the stage. Therefore, an array is created within the computer to store this three dimensional

data. This data can then be converted to an image by translating the position to an image pixel and the A_{in} voltage output to a color palette, which projects the illusion of depth.

Future Development

This shear force microscope can be further modified to provide optical and spectrographic images, in addition to those topographic images. The instrument could be configured by two techniques. The fiber probe will act as source or collection. In the first instrumental scenario, laser light is introduced into the fiber probe which is incident on the sample. A method of detecting the sample response is then employed. If the sample was an electronic or solid-state device, optical response can be measured by detecting the electrical current produced from the incident light excitation. If the sample is biological or polymeric, then an optical method can be employed. The optical signal can be collected using a microscope objective which focuses the light from the probe into a detector, such as a charged coupled device (CCD) or a photomultiplier tube (PMT).

In the second instrumental scenario, laser light is incident on the sample using conventional FF optics. This light would be focused onto the sample. The fiber probe would then be used to collect the optical response from the sample. The fiber would then be coupled to a detector, such as a CCD or PMT.

6. Vectra, a Liquid-Crystalline Copolyester

6.1. General Foundations

Introduction

Vectra is a commercially produced thermoplastic developed and manufactured by Celanese LTD, Charlotte, North Carolina. It is produced in forms of film sheets, molds, and yarns to encompass a broad range of commercial applications. Extruded film sheets are used in the structural reinforcement of commercial products to increase their strength and durability. For example, Vectra has been widely used in sporting equipment, such as tennis rackets, sailcloth, boat hulls, skis, and golf clubs. It is also used in the reinforcement of automobile tires. Injection molded Vectra is a highly electrically resistant material and has found a high demand in electrical and computer products, such as connectors, plugs, and electrical insulators, in general. Vectran[®] is the commercial trade name of the class of Vectra products spun into multi-filament yarns. These yarns are used for military, mountaineering, and yachting ropes. Vectran[®] was also deployed in the airbag construction of Pathfinder's mission to Mars in July 1997. These airbags were used to cushion the landing of the Pathfinder onto the planet's surface.

In recent years, researchers have discovered the pure and applied motivations for studying the optical properties of certain oriented organic polymers^{50, 51, 52}. In

particular, Vectra lies within a class of liquid-crystalline polymers that possess extremely long conjugation length, a high degree of structural and crystalline orientation, and a highly directed and intense permanent dipole moment. These basic characteristics allow Vectra to possess strong hyperpolarizability and fluorescence. These optical properties may lead to increased commercial applications in optical devices such as light emitting diodes, light sources, and flat panel displays.

Chemistry

Vectra is a main-chain thermotropic liquid-crystalline polymer (LCP) composed of random monomeric units of 4-hydroxybenzoic acid and 6-hydroxy-2-naphthoic acid. Vectra A is a member of a class of random copolyester LCPs composed solely of 4-hydroxybenzoic acid (HBA) [CAS 99-96-7] and 6-hydroxy-2-naphthoic acid (HNA) [CAS 16712-64-4]. Unlike the majority of other LCPs investigated for optical applications, Vectra is a main-chain LCP; it does not possess additional substituent or side groups. Vectra is also a thermotropic LCP, which possesses an inherent mesophase without the use of solvents.

This thesis specifically focuses on the optical properties with a monomeric composition ratio of 73 / 27 HBA / HNA, Figure 6.1.01, commercially known as Vectra A910. All further references to this compound will be referred to as copoly(HBA/HNA).

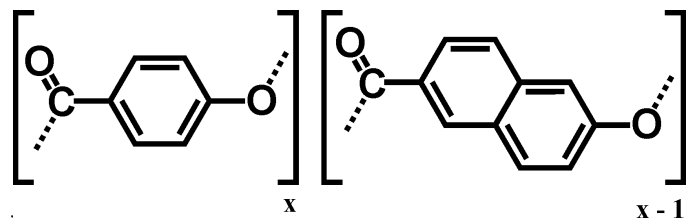


Figure 6.1.01. Chemical structure of Vectra A910 or copoly(HBA/HNA).

Traditionally, 2,6-disubstituted naphthalene groups are incorporated into main-chain polymers to introduce a transverse offset directly into the polymer backbone. This has the effect of creating an additional crankshaft motion. Specifically, this has the effect of reducing the linearity and persistence length⁵⁰ of the HBA homopolymer, therefore creating the mesophase. “The random nature of the copolymer reduces the crystallite melting point to ~300°C compared with a value of the order of 450°C for the homopolymer.”⁵³ Henceforth, monomeric ratios can be varied to synthesize a copolymer with different solid crystal and isotropic liquid melting points, which will define the temperature range of the mesophase or liquid crystal state. Commercially, an optimum LCP has a low and broad temperature range for the liquid crystal phase to increase the ease and flexibility of melt material processing⁵⁴.

X-ray crystallographic studies^{55, 56} reveal that aperiodic diffraction lines along the extended copolymer chain correspond to a completely random monomeric sequence. However, even with the existence of a random sequence, longitudinal registration does occur between molecules⁵⁷. This registration directly leads to highly ordered domains, as compared to completely disordered and amorphous regions, within the LCP film.

These domains were observed via X-ray⁵³, dark-field transverse electron microscopy⁵⁸, and polarized FTIR⁵⁹ which are randomly distributed throughout the polymer film. In extruded samples, these domains are roughly 40 - 90 nm long by 15 - 20 nm wide in the direction of extrusion⁵⁸.

Extruded thin films possess the highest degree of molecular orientation as compared with injection molded and multi-filament yarns. The reason for this is extrusion inherently forces alignment of the molecular chains in the direction of extrusion. Extrusion will generate three primary regions of orientation based on the depth from the sample surface: the central, outer, and skin layers. The central core layers possess the lowest degree of orientation, while the outermost skin layers possess the highest. Kaito *et al.* performed attenuated total reflection (ATR) infrared spectroscopy in which exponentially decaying intensity is a function of sample depth. These measurements prove that the skin layers are less than 20 μm thick, however the primary optical interactions will occur in this region because of the greater orientational and crystalline order.⁵⁹ It is these properties that make the extruded thin films especially attractive for optical study.

An important aspect of copoly(HBA/HNA) is the three torsional bond angles within the ester linkage, Figure 6.1.02. The torsional angles determine the degree of conjugation between adjacent aromatic, benzyl or naphthyl, rings. Hofmann *et al.*⁵⁷ employed molecular modeling to confirm the X-ray data. They found that in the extended chain ($\tau_2 = \pm 180^\circ$), adjacent aromatic planes will possess an angular displacement of $\pm 60^\circ$ in the solid or crystalline state. This is primarily due the steric stress between the carbonyl

oxygen and the aromatic hydrogen placed on torsion τ_2 . This torsion has the net effect of creating a helix through the length of the extended molecule. Gas phase *ab initio*⁶⁰ calculations indicate that the energy maximum for this nonplanar torsion is on the order of 2 kcal/mole.

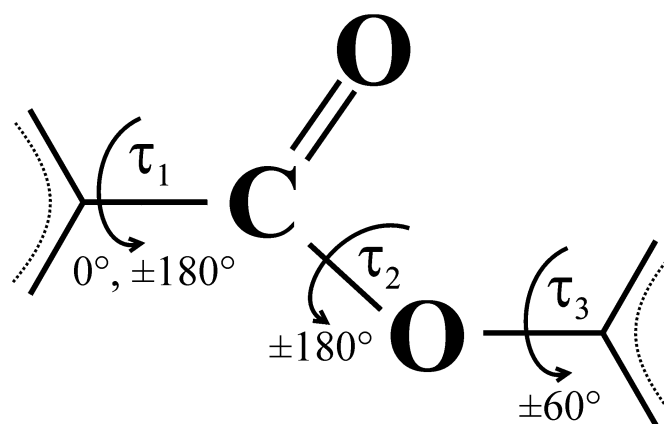


Figure 6.1.02. Torsional angles of the ester linkage of copoly(HBA/HNA).

An optical aspect of copoly(HBA/HNA), is the presence of an oriented unidirectional permanent polarization or electric dipole moment within a single molecule. The ester oxygen acts as a donor of charge into its neighboring aromatic π -orbitals. The carbonyl oxygen will then accept this charge, as shown in Figure 6.1.03. This donor-acceptor pair creates a strong permanent electric dipole with an approximate net direction along the nematic director. As opposed to related LCPs, such as poly(ethyleneterephthalate) (PET) or the polymer comprised of 50% HNA, 25% terephthalate, and 25% *p*-aminophenol (Vectra B), the unique tandem polymerization of the copoly(HBA/HNA) orients the polymer producing a large dipole moment. The non-centrosymmetric character of the polymer chain was demonstrated by the observation of bulk second harmonic generation by Wanatabe *et al.*⁶¹ The other LCPs mentioned above do not have a significant second-order nonlinear optical response.

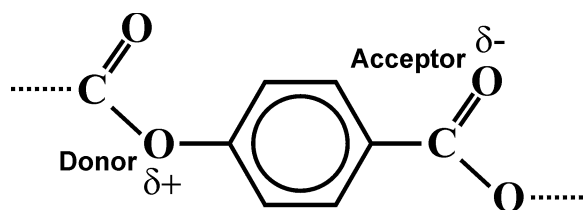


Figure 6.1.03. Permanent dipoles due to strong electron donating and withdrawing groups, respectively, and electron delocalization within copoly(HBA/HNA).

As can be seen in the above figures, increasing the total number of double bonds within a molecule will increase the total delocalization and thus increase conjugation within the molecule. Increased conjugation increases the first and second-order hyperpolarizabilities with trends following the free electron model adapted to π orbitals⁶². These increased first and second-order hyperpolarizabilities are experimentally detected as strong second and third harmonic generations, respectively.

6.2. Optical Absorbance

A thorough discussion of the absorption of a material was discussed in Chapter 4 - Photoluminescence. Absorption of the incident light will excite the electron from the singlet ground state S_0 to the singlet excited state S_1 . Spectra were obtained on a Hewlett Packard 8452A Diode Array Spectrometer. The monomeric samples were prepared by dissolving 1 mM HBA and HNA crystals in 100% ethanol. The copoly(HBA/HNA) was formed into a 10 μm extruded thin film. All samples were studied at ambient temperature and pressure.

The absorption spectrum of HBA, Figure 6.2.02 Spectrum A, has a strong absorption band ranging from 200 to approximately 290 nm (6.20 to 4.28 eV). This absorption will form the excited state as seen in Figure 6.2.01.

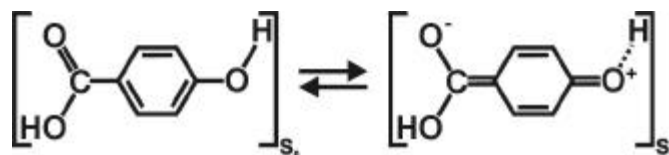


Figure 6.2.01. Ground and excited state of HBA upon optical absorption. HNA will have a similar excited state.

The absorption spectrum of HNA, Figure 6.2.02 Spectrum B, has a strong and broad absorption from 200 to approximately 340 nm (6.20 to 3.65 eV). This absorption is considerably broader because of the increased conjugation length between the electron donating alcohol group and the electron withdrawing carbonyl group.

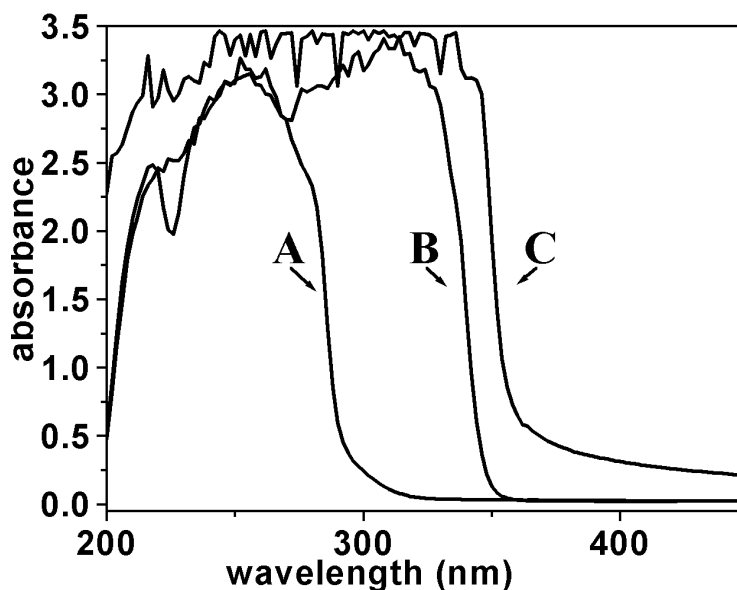


Figure 6.2.02. UV-VIS absorption spectra of 4-hydroxybenzoic acid (A) in 1 mM ethanol, 6-hydroxy-2-naphthoic acid (B) in 1 mM ethanol, and 10 μ m copoly(HBA/HNA) (C) extruded film at ambient conditions.

The absorption spectrum of copoly(HBA/HNA) encompasses the absorption ranges of both HBA and HNA. This is simply due to its copolymer composition of both aforementioned monomers as well as the increased conjugation strength and/or length. As discussed in the above introduction, partial or full conjugation will exist within the ester linkage and thus between adjacent aromatic groups. The degree of conjugation will ultimately depend on the planarity of the adjacent aromatic groups.

The long tail extending beyond 350 nm (3.54 eV) in the copoly(HBA/HNA) absorption spectrum is also due to long conjugation lengths. This tail extends into the infrared region which can be observed in the FT-Raman spectrum, Figure 6.3.02. A single copoly(HBA/HNA) molecule can extend to thousands of subunits, or on the order of hundreds of nanometers in length. A perfectly planar molecule will possess a conjugation length of the entire molecule. In a real system, however, a distribution of conjugation lengths will exist for the bulk material. The absolute conjugation length and degree will depend on the degree of planarity between the adjacent aromatic groups. Therefore, a distribution of conjugation lengths and/or strengths will exist within a single molecule. This distribution will lend itself to absorption of lower energy as compared to its monomeric content.

In summary, copoly(HBA/HNA) possesses a strong absorption profile. Its absorption is stronger and broader than both of its monomeric subunits. This is primarily due to a distribution of conjugation lengths and strengths within a single molecule, which leads to the above absorption in the bulk material. This absorption profile is a primary

contributor to a strong second-harmonic signal, Chapter 7 - Nonlinear Response of Vectra, and photoluminescent response, Chapter 8 - Photoluminescence of Vectra.

6.3. Molecular Vibrations

A thorough discussion of the molecular vibrations of a material were discussed in Chapter 1 – Molecular Vibrations. Infrared spectra were obtained on a Matheson FT-IR Model RS-2. The monomeric samples were prepared by pressing solid HBA and HNA crystals into translucent pellets. The copoly(HBA/HNA) was formed into a 10 μm extruded thin film. All samples were studied at ambient temperature and pressure.

The most notable difference between the monomers and the copolymer, Figure 6.3.01, is the broad band between 2000 and 3500 cm^{-1} . This broad peak is due to dimer formation between the monomers. A dimer is formed by hydrogen bonding between an the carbonyl oxygen and a hydrogen from an adjacent monomer 6.3.

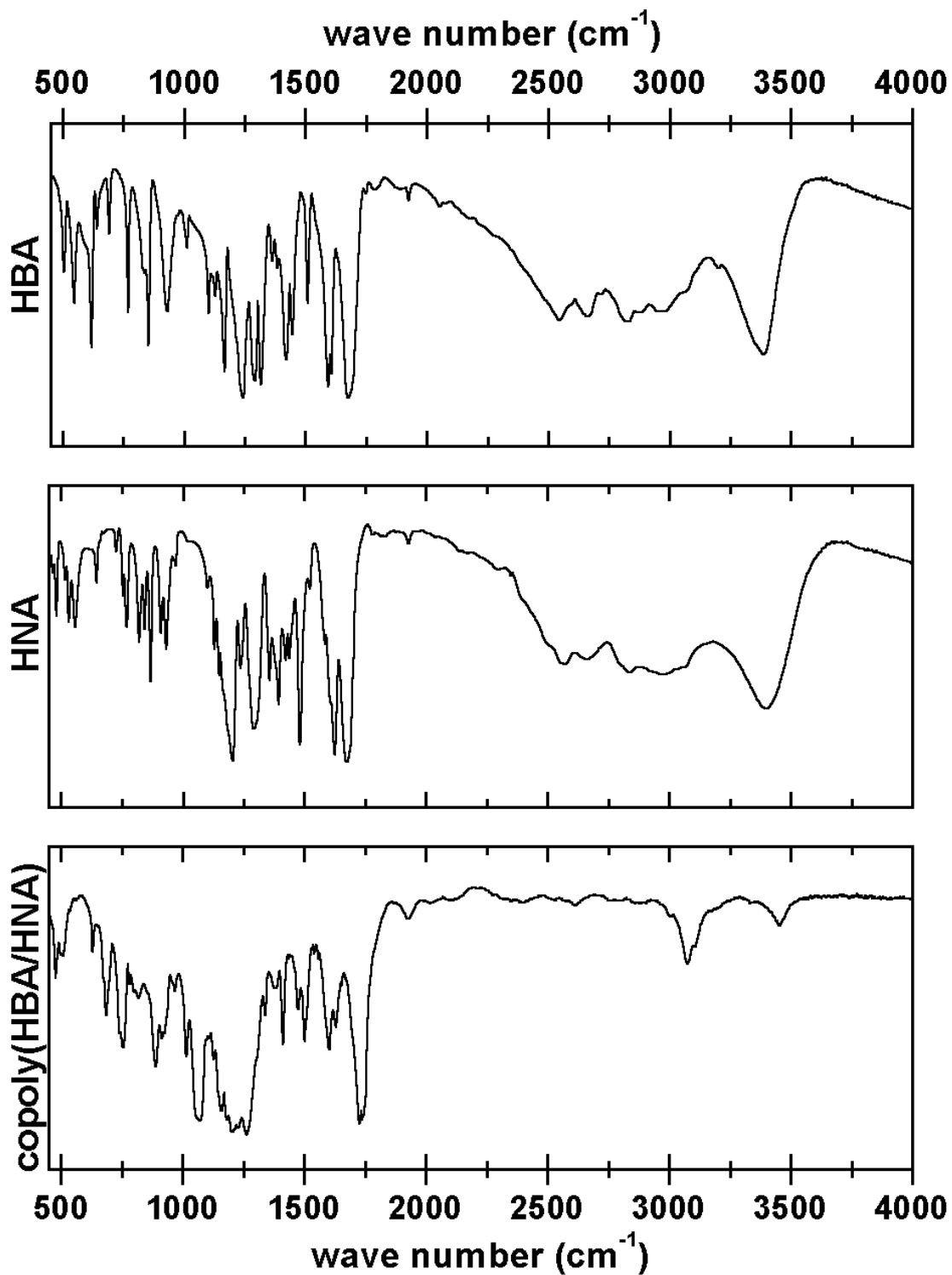


Figure 6.3.01. Infrared spectra of 4-hydroxybenzoic acid (HBA) in a solid pellet, 6-hydroxy-2-naphthoic acid (HNA) in a solid pellet, and 10 μm copoly(HBA/HNA) extruded film at ambient conditions.

The following table lists the peak assignments to generally explain the vibrational modes present within these molecules.

Mode	Maximum / Center	Range	Type
Ring-hydrogen bend	885.2 max	854.3-946.9	Doublet
C-O-C stretch	1074.2 max	1027.9-1097.3	Singlet
O=C-O-C stretch	1230.4 center	1137.8-1322.9	Broadened
Ring breathing	1560.2 center	1454.1-1666.2	Two mirrored doublets
C=O stretch	1727.9 max	1666.2-1816.6	Singlet
Ring-hydrogen stretch	3081.7 max	2970.0-3189.7	Singlet
Overtone	3455.8 max	3371.0-3533.0	Singlet

Table 6.3.01. Peak assignments of the vibrational spectra for copoly(HBA/HNA).

Figure 6.3.02 shows the comparison between the above copoly(HBA/HNA) infrared spectrum and its Raman spectrum. Copoly(HBA/HNA) possesses a strong absorption profile that interferes with any Raman signal in the visible region. To obtain the Raman spectrum of copoly(HBA/HNA) we used a Nicolet Magna 760 with a FT-Raman Module. This system employs a laser source of 1064 nm (1.17 eV). This light is sufficiently removed from the strong absorption band to allow for detection of the Raman signal. The base-line drift of the FT-Raman spectrum indicates the presence of some absorption, even in the infrared region.

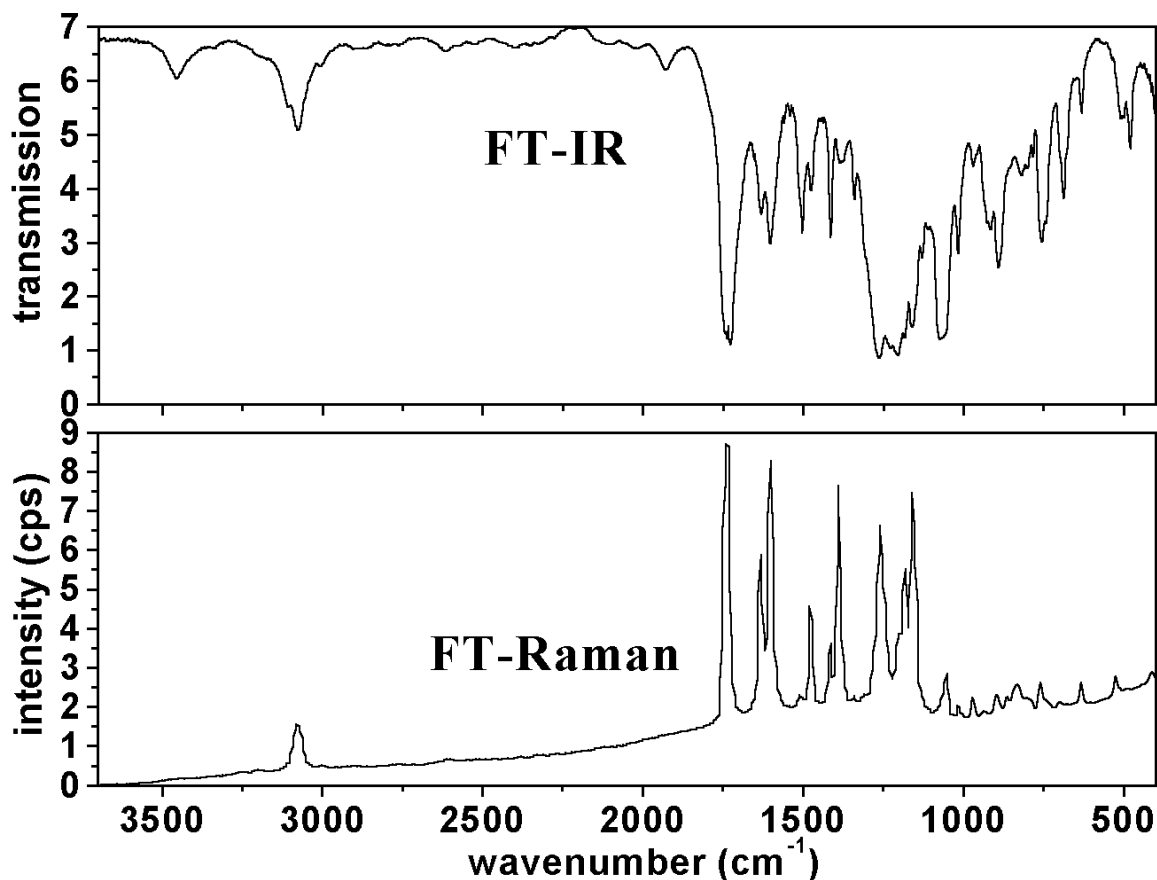


Figure 6.3.02. Infrared and FT-Raman spectra of copoly(HBA/HNA) at ambient conditions.

In conclusion, copoly(HBA/HNA) is a main-chain thermotropic LCP that has carved a strong niche in the commercial and industrial markets. Its optical properties are based on its high degree of orientation in extruded films, its permanent dipole moment, and its delocalization of charge creating a distribution of conjugation lengths.

6.4. Phase Transitions

Copoly(HBA/HNA) is a copolyester that exhibits numerous complex temperature-dependant phase transitions, which have been studied since the middle of the 1980's

using various experimental techniques. Copoly(HBA/HNA) possesses four phase transitions in the range of -80 to 400 °C. These phase transitions are called the γ , β , α or T_g , and T_m from -60 to 280 °C for 73:27 copoly(HBA/HNA), as summarized in the below Table 6.4.01. The temperature, and respective activation energy, of each of these phase transitions have been identified by various techniques, including thermal expansion ⁶³, dynamic tensile and shear moduli relaxation ⁶⁴, dielectric relaxation ^{65, 66, 67}, X-ray ^{68, 69, 70}, and positron annihilation ⁷¹. Differential scanning calorimetry (DSC) was performed by most of the latter researchers to confirm and correlate their results.

Phase Transition	Temperature (°C)	Symbol
Nematic → Isotropic (Melt)	+280	T_m
Crystal → Nematic (Glass)	+100	T_g or α
Local HNA Rotations	+25	β
Local HBA Rotations	-60	γ

Table 6.4.01. Phase Transitions of Copoly(HBA/HNA).

The highest temperature transition is known as the nematic mesophase to isotropic melt, or T_m . This melt usually occurs at 280 °C for the 73:27 HBA/HNA copolyester ^{66, 67} and 288 °C for the 75:25 HBA/HNA copolyester ^{70, 71}. This melt is characterized by a macroscopic shrinkage of the polymer along the nematic director, with disorientation and full translational motion of the molecular chains.

The next highest phase transition is called the α transition, which occurs at approximately 100 °C ^{66, 64, 63, 71}. This transition is similar to a glass transition, or T_g , in a normal polymer ⁶⁴ and is characterized by the material changing from a glassy or more crystalline state to a mobile nematic mesophase. The activation energy of this rotation

was found to be roughly 170 kcal/mole from the dielectric studies ⁶⁶. Additionally, Yoon *et al.* ⁶⁷, found that the dielectric constant ϵ' and loss ϵ'' exponentially increase with respect with temperature. This is due to ionic conduction within copoly(HBA/HNA) and begins in the 100 °C region.

Thermal expansion ⁶³ plots revealed that the axial expansion was small but negative, or it contracts in the direction of nematic director. The lateral expansion was large and positive, or it rapidly expands perpendicular to the nematic director. Based on this study, copoly(HBA/HNA) clearly shows a transition due to a linearly decreasing axial expansion in the range of, and is attributed to, the α transition. Therefore, the copolyester is contracting axially and expanding laterally, in which case the effect is amplified once the copoly(HBA/HNA) reaches 100 °C. These results indicate that the thermal expansion is based on intrachain molecular segments rotating in concert, otherwise known as a segmental crankshaft motion ⁵⁰.

The β phase transition occurs at roughly room temperature, 25 °C, and corresponds to the local rotations of the naphthalene groups ^{66, 64, 63, 67, 71}. In addition to local HNA rotations, Yoon *et al.* ⁶⁷ via dielectric relaxation, and by Green *et al.* ⁶³ by thermal expansion, found that the β transition has a glass transition component that is accompanied by reduced conformational constraints. The activation energy of this rotation was found to be 25 ± 5 kcal/mole from the dielectric studies ⁶⁶.

The lowest temperature phase transition is called the γ transition, which occurs at a temperature of $-60\text{ }^{\circ}\text{C}$ ^{66, 64, 67}. This transition is attributed to the local rotations of the phenylene groups. The activation energy of this rotation was found to be 12 ± 3 kcal/mole from dielectric relaxation results ⁶⁶.

The lowest temperature phase transitions, γ and β , are due to the phenylene and naphthalene groups locally rotating within a chain, respectively. Hummel and Flory ⁷² suggest that the carbonyl unit τ_1 is strongly coupled to the adjacent aromatic group through resonance stabilization, as envisaged in Figure 6.1.02. Rotation about τ_2 would cause the entire chain to reorient, which is not possible due to the long chain length and solid packing inherent to the copolyester. Hence, only the ether oxygen to aromatic torsion τ_3 is available for rotation. Since torsional rotations will only occur at τ_3 , then the phenylene or naphthalene, with their ester groups, will rotate as a single unit.

In summary, copoly(HBA/HNA) possesses four phase transitions. The first two correspond to the γ and β phase transitions, or the local HBA and HNA rotations, at -60 and $25\text{ }^{\circ}\text{C}$, respectively. The local HNA rotation also has a small component of a glass transition. The third corresponds to the α phase transition, or segmental crankshaft motions, at $100\text{ }^{\circ}\text{C}$. And the final corresponds to the full polymeric or isotropic melt, or full molecular motion and reorientation, at $280\text{ }^{\circ}\text{C}$. These transitions have a marked effect on the microscopic and macroscopic properties of the copolyester.

7. Nonlinear Response of Vectra

7.1. General Foundations

Introduction

This chapter is the presentation of the nonlinear response of Vectra, or copoly(HBA/HNA). The generalized theory and instrumentation of nonlinear optical responses, hyperpolarizability, and second-harmonic generation (SHG), is presented in Chapter 3 – Nonlinear Optics. The chemical foundations of Vectra, otherwise known as copoly(HBA/HNA), are presented in Chapter 6 - Vectra, a Liquid-Crystalline Copolyester. As will be shown, Vectra possesses an extremely strong second-harmonic signal. This strong response is the primary motivation for its use as an optical material, such as in polymer-based LEDs and LCDs.

Monomeric History

Early research comprised studying the SHG components of its monomeric subunits, primarily 4-hydroxybenzoic acid (HBA). These SHG components comprise the permanent dipole moment, degree and length of conjugation through the π bonding orbitals, and chemical orientation leading to the centricity of the molecule. Since 2,6-disubstituted naphthene derivatives are chemically and electronically analogous to *para*-

disubstituted benzene derivatives, inferences from these benzene based systems can be extrapolated to their naphthene derivatives. In fact, the naphthene derivatives will possess a higher degree of conjugation, and thus increased hyperpolarizability, as compared to its benzene analogs.

In 1978, Dulcic and Sauteret⁷³ studied the second-harmonic response of *para*-disubstituted benzenes in a dimethylsulfoxide solvent. The substitutions were based on donor-acceptor pairs. Their data indicated that an increased response is observed when an increased permanent dipole moment is created across the aromatic ring due to a strong donor-acceptor potential. They also found that the first electronic absorption maxima will increase, respectively, which corresponds to a red-shifted lowering of energy. Therefore, Dulcic explicitly stated that an increase of the second-harmonic response correlates to an increase in the absorption shift.

Their explanation of the increase SHG in *para*-disubstituted benzene derivatives are based on the mesomeric perturbation effects. This effect is based on understanding the wavefunction of the molecule by including the substituents as an integral part of the π bonding system of the aromatic ring. The donor substituent possesses a high lying occupied orbital, while the acceptor possesses a low lying vacant orbital. The π electron system allows interaction of this potential to produce a somewhat charged asymmetric ground state wavefunction and a highly charged asymmetric excited state wavefunction. Therefore, this electronic asymmetry would comprise a non-centrosymmetric molecule,

lending itself to a second-harmonic response. This effect was also discussed in sections 6.1 and 6.2 of this thesis.

In 1965, Terhune *et al.*⁷⁴ developed an instrument using a giant energy pulsed ruby laser which was tightly focused in a solution. Scattered light was collected perpendicular from the incident beam at the focal point within the solution. This scattered light was derived from both inelastic, Raman, and elastic, Rayleigh, collisions of the photons with the solute and solvent molecules. The Raman scattering was confirmed against infrared absorption spectra. The Rayleigh scattering led to the further development to HRS in the early 1990's by Clays *et al.*^{75, 76} using a Q-switched Nd-YAG laser. It is important to note that the average incident radiation at the focal point is far below the thresholds for stimulated Raman and Brillouin scattering, self-focusing or self-defocusing, and dielectric breakdown. Additionally, Clays stated that HRS is the only modern technique that can measure the first hyperpolarizability, or microscopic second-harmonic response, from a solute without having to independently determine the dipole moment and the second-order hyperpolarizability of the molecule. This has an enormous advantage over electric-field induced second-harmonic generation (EFISHG), which was the only technique available for measuring nonlinear optical effects in solution prior to HRS.

In 1996, Ray *et al.*^{77, 78, 79, 80} performed a series of experiments that confirm the experimental results of Dulcic. Ray performed hyper-Rayleigh scattering (HRS) measurements on disubstituted derivatives of benzoic and cinnamic acids. These derivatives comprised the carboxylic acceptor with varying donor functional groups.

Ray found that all compounds studied possess relatively strong hyperpolarizability, $20 - 80 \times 10^{-30}$ esu. Each species possesses an acidic and basic form, where the corresponding conjugate base routinely exhibits a stronger response than the acid form. The basic form exhibited a response approximately twice that of the acidic form. This is understood by knowing that the basic form possesses a strong permanent dipole moment, where electron transfer occurs between the donor group and the carboxylic group. The acidic form possesses a weak dipole moment based on partial charge transfer between these respective groups.

Additionally, Ray reported the second-harmonic response of the ortho, meta, and para configurations of the disubstituted benzoic derivatives. Although all three configurations possess strong responses, ortho derivatives consistently possessed the smallest, and para possessing the largest hyperpolarizability. An analysis of the data indicates that the ortho derivatives possess a nonlinear response because of the resonance structures between the extreme acid and base scenarios. This innate resonance will allow for charge stabilization throughout the π bonding orbitals. Its response is the lowest of the three configurations because of the small charge separation, and thus small dipole strength, inherent in the ortho configuration. The meta configuration, although greater than ortho, was only slightly higher than that of the ortho configuration. The meta configuration has a much greater charge separation than ortho, however, the meta configuration does not possess stable resonance structures⁵¹. Therefore, the lack of stable resonance structures for the meta configuration will cancel the nonlinear effect imposed by the greater charge

separation. The para configuration had an appreciably higher response, approximately by a factor of 1.5, than both the ortho and meta configurations. The para configuration has the greatest charge separation and the ability to stabilize the charge through resonance.

Cinnamic acid is similar in structure to benzoic acid, except that it possesses an additional ethylene group between the aromatic ring and the carbonyl group, as shown in Figure 7.1.01. Therefore, cinnamic acid derivatives will have a similar electronic mechanism, as compared with analogous benzoic derivatives, except cinnamic derivatives will possess a longer conjugation length⁸⁰. The latter will lead to a stronger hyperpolarizability, approximately by a factor of 1.5, and a red-shift of the first electronic absorption maximum.

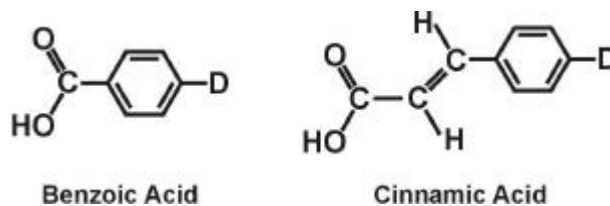


Figure 7.1.01. *p*-Benzoic and *p*-Cinnamic Acid derivatives, where D is the substituted donor group.

This fundamental comparison of benzoic and cinnamic acid derivatives is crucial to the understanding of conjugation length in copoly(HBA/HNA). An increase in conjugation length lowers the energy of the charge separations within the molecule. The greater the conjugation length the greater the number of resonance structures, which inherently will lower the energy and stabilize the charge distributions within the molecule. The greater the ability of the molecule to stabilize its charge distribution will red-shift or lower its first electronic absorption maximum. This red-shifting is the first sign the molecule has lowered its internal energy. Once the molecule possesses a greater ability to stabilize the

charge distribution, and thus absorb greater energy, then an enhancement of the hyperpolarizability will be seen in the molecule. This concept is revealed in the charge separation and resonance structures of the ortho, meta, and para configurations, as well as the charge separation through increased conjugation length between the analogous benzoic and cinnamic acid derivatives⁸¹⁻⁸⁰.

Polymeric History

In 1994, Asada *et al.*⁸² measured the macroscopic nonlinear response of copoly(HBA/HNA). They used a Q-switched Nd-YAG laser source to produce an incident pulsed beam of 1064 nm (1.17 eV). They reported a response of 5×10^{-12} m/V for uniaxially d_{33} oriented extruded thin films, when compared against the d_{11} quartz standard.

In 1996, Watanabe *et al.*⁶¹ continued a more detailed study than that of Asada⁸². They confirmed Asada's nonlinear response of 5×10^{-12} m/V for samples of uniaxially-oriented extruded films of copoly(HBA/HNA). Additionally, they reported two new observations. First, the sample orientation, or chain polarization, is sensitive to the relative angle of the incident linearly polarized light. The second-harmonic response was maximized when the incident electric field was collinear with the chain polarization, also known as the extrusion direction or the nematic director. Conversely, the second-harmonic response was minimized when the incident field was perpendicular to the incident polarization.

Secondly, Watanabe found that only those molecules above a minimum polymerization length would produce a second-harmonic response. They found that films of copoly(HBA/HNA) with a viscosity above 2.6 dL/g produce a nonlinear response. They were unable to determine the mean chain length or molecular weight of this polymerization threshold because of the insolubility of copoly(HBA/HNA) in conventional solvents. Therefore, copoly(HBA/HNA) must exceed a minimum polymerization threshold, and thus a critical dipole moment must be achieved, to produce a second-harmonic response.

Further work by both groups ⁸³⁻⁸⁴⁻⁸⁵, reconfirmed the previously discussed results, as well as, that the polymer has C_s symmetry with a mirror plane rotationally disordered about the molecular axis. The latter work was based on orientational calculations with comparison to the experimental results.

Samples of copoly(HBA/HNA) can be extruded into thin polymer sheets. These sheets will have a distribution of chain orientations given by the order parameter S , which is given by ⁵²

$$S = \frac{1}{2}(3\langle \cos^2 \alpha \rangle - 1)$$

Equation 7.2.01

where α is the angle between the director and the rod-like molecules and the $\langle \cos^2 \alpha \rangle$ indicates an average angular distribution between the molecular orientations

and the nematic director. An order parameter of one has all molecules in perfect alignment, and that of zero is completely disoriented. X-Ray crystallography^{86, 61} and polarized attenuated total reflection (ATR) / Fourier-transform infrared (FTIR) and spectroscopy^{59, 87} reports order parameters of 0.80 to 0.96 for various thicknesses of extruded copoly(HBA/HNA). In fact, the polarized ATR/FTIR experiments prove that that the order parameter is greater at the surface of the sample, called the skin, as opposed to the inner core or bulk. Therefore, thinner samples, those of whom possess little or no core, will have the highest order throughout the entire thickness of the sample sheet.

7.2. Macroscopic SHG

The instrumentation used to perform all second-harmonic measurements on copoly(HBA/HNA) were discussed in Section 3.3 – Nonlinear Instrumentation of this thesis. In summary, 800 nm (1.55 eV) pulsed red light was introduced to a sample of copoly(HBA/HNA), resulting in 400 nm (3.10 eV) pulsed blue light. The resultant light was filtered to exclude any incident 800 nm (1.55 eV) light and was passed through a scanning monochromator. The second-harmonic light was converted to an electrical signal using a photomultiplier tube (PMT). The electrical signal was processed by photon counting, and then analyzed by a computer.

The resultant spectral profile was scanned and compared against the source spectral profile. This test ensured that the collected 400 nm (3.10 eV) was indeed that produced from scattered light arising from second-harmonic generation. Any homogeneous or

inhomogeneous broadening of the second-harmonic light would imply the presence of other optical mechanisms or interferences. Under all conditions, the second-harmonic response of copoly(HBA/HNA) had the same spectral profile and band-width as that of the source light.

Another experiment that was employed, was to tune the wavelength of the source light by 800 ± 20 nm . If the resultant second-harmonic signal correspondingly varies by 400 ± 10 nm, then it could be concluded that the resultant light is indeed second-harmonic light. Therefore, these two experiments prove that when 800 nm (1.55 eV) light, of sufficient power, is incident on copoly(HBA/HNA), that second-harmonic light is produced and can be observed and studied at a wavelength of 400 nm (3.10 eV).

Standardization of the copoly(HBA/HNA) second-harmonic response was performed and compared against a y-cut d_{11} quartz crystal. We estimate that the macroscopic or bulk second-harmonic response, $\chi_{zzz}^{(2)}$, where z is along the direction of the polymer chain, is 1.3×10^{-10} m/V⁸⁸. As discussed, Asada *et al.*⁸²⁻⁸⁵ and Wanatabe *et al.*⁶¹ report a value of 5×10^{-12} m/V, with an incident source of 1064 nm (1.17 eV). This difference is attributed to the two-photon resonance of the polymer at 400 nm (3.10 eV). This resonance effect can be seen by associating the finite absorbance of copoly(HBA/HNA) at 400 nm (3.10 eV), as discussed in Section 6.2 - Optical Absorbance and specifically illustrated in Figure 6.2.02.

The bulk second-harmonic response for copoly(HBA/HNA) was studied at various sample orientations. The incident 800 nm (1.55 eV) light is linearly polarized with additional optical processing through prism-based polarizers. The extruded sample sheet is placed on a rotating stage to allow for measurement of the second-harmonic response at various chain orientations. The data, with a $\cos^2\theta$ fit, of the second-harmonic response versus relative chain orientation is presented in Figure 7.2.01.

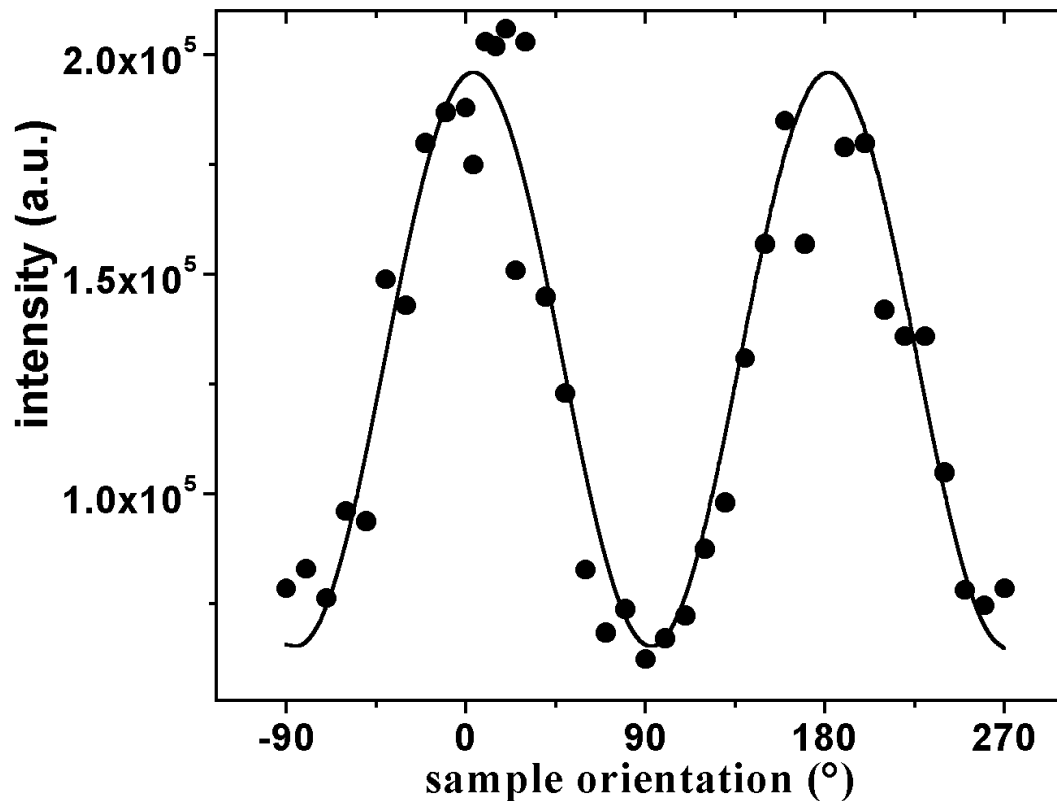


Figure 7.2.01. Linearly polarized second-harmonic response versus chain orientation for 50 μm copoly(HBA/HNA) film at ambient conditions.

The above data reveals that a strong second-harmonic response occurs when the nematic director is in direct alignment with the electric field of the incident light. The aligned (0° or 180°) effect has a factor of five in its response as compared to the completely unaligned (90° or 270°) orientation, as confirmed by Watanabe *et al.*⁶¹. This

observation simply reveals that the maximum second-harmonic response is observed when the electric field is parallel with the nematic director of the copolymer.

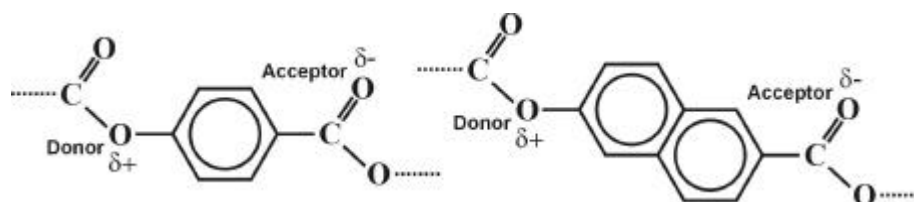


Figure 7.2.02. Vectors of the donor/acceptor groups in the benzyl and naphthyl monomers, respectively, of copoly(HBA/HNA).

The nematic director would correspond with the average direction of permanent dipole moments inherent within the monomeric subunits, as shown in Figure 7.2.02. These molecular schemes reveal that there does exist an angle between the vector of the dipole and that of the chain polymerization, also known as the nematic director. However, a distribution of dipole directions will exist with a net effect collinear with the nematic director. Therefore, the bulk second-harmonic response would be dependent on this net effect of dipole vectors, which would be approximately parallel to the nematic director.

The second-harmonic responses of the incident electric field being parallel and perpendicular to the molecular polarization were retrieved to produce the orientational ratio. This ratio is the parallel response divided by the perpendicular response for various thicknesses of the extruded copoly(HBA/HNA) thin film samples. The ratios are given in Table 7.2.01.

Thickness (μm)	Parallel/Perpendicular Ratio
75	1.679×10^1
25	4.691×10^1
15	3.048×10^2
10	6.323×10^4

Table 7.2.01. Thickness dependent second-harmonic response of copoly(HBA/HNA).

where the SHG increase can be attributed to the orientation of the sample. The orientation of a sample will depend on its thickness, extrusion velocity, and cooling method, for instance cooling by quenching or annealing.

Kaito *et al.*⁵⁹ stated that the skin layer of an extruded sample is less than 20 μm which exhibited an order parameter of greater than 0.90. Therefore it can be concluded that the above 10 mm sample had no outer or inner core. This sample had the greatest orientation throughout the sample depth, which correspondingly produced the greatest nonlinear response. The thicker samples produced significant orientational responses, however the bulk or core contributed to a lack of alignment, therefore their ratios were correspondingly less than the thinnest sample.

8. Photoluminescence of Vectra

8.1. General Foundations

Introduction

This chapter is the presentation of the photoluminescence of Vectra, or copoly(HBA/HNA). The generalized theory and instrumentation of photoluminescence is presented in Chapter 4 – Photoluminescence. The chemical foundations of Vectra, otherwise known as copoly(HBA/HNA), are presented in Chapter 6 - Vectra, a Liquid-Crystalline Copolyester. As will be shown, Vectra possesses an extremely strong fluorescent signal. This strong response is the primary motivation for its use as an optical material, such as in polymer-based LEDs and LCDs.

Stretched Exponential Decay

This section is provided as a basis to understand the time-resolved fluorescence lifetimes observed in Section 8.3 - Dynamic Photoluminescence and Section 8.4 - Thermal Photoluminescence. All time-resolved fluorescence measurements on copoly(HBA/HNA) clearly indicate a first-order stretched exponential decay, as given by

$$I(t) = I(0) \exp(-(t/\tau)^\alpha)$$

Equation 8.1.01

where I is the intensity of the fluorescence, t is time, τ is the lifetime, and α is the stretching coefficient. The stretching coefficient will range from zero to one, in which a value of one is the classical first-order decay. This function is formally known as the Kohlrausch-Williams-Watts (kww), or simply the Williams-Watts (ww), relaxation process^{89,90} and was used to empirically fit experimentally generated relaxation data⁹¹.

In 1863, Kohlrausch⁹² first used stretched exponential behavior to describe mechanical relaxation data. In recent years, stretched exponential decays have been observed in a great many physical^{93,94,95}, chemical^{96,97,98}, and specifically polymeric^{99,100,101,102} systems. This extensive work, in a wide variety of systems, has demonstrated that stretched exponential kinetics are correlated with energetic and/or structural disorder.

Time-resolved photoluminescent measurements of poly(phenylenevinylene) (PPV)^{102,103}, and related luminescent polymers, have shown similar stretched exponential behavior. Physically, the stretched exponential is due to a distribution of decay rates. This distribution of decay rates in the polymer chain is usually associated with a distribution in chain or conjugation lengths^{104,105}. In the case of copoly(HBA/HNA), there is also a distribution of random monomers which make up the polymer. Therefore,

it is possible that the random nature of the copolyester units is the origin of the disorder that causes the stretched exponential decay.

Stretched Exponential Dynamics

The introduction of the stretching coefficient α to a classical first-order decay allows the decay to possess an infinite average lifetime, commonly known as dispersive or fractal time^{93, 106, 107}. An infinite average lifetime simply means that there exists a finite probability that a significant portion of the time dependant processes will occur after the total time of the experiment. For example, in the case of a fluorescence emission, an infinite average lifetime is such that there will be a portion of excited state relaxations after the experiment is complete. In other words, the relaxation process is described by a distribution of lifetimes.

For this section only, allow Equation 8.1.01 to be rewritten as

$$I(t) = \exp(-(t / \tau_{ww})^\alpha)$$

Equation 8.1.02

where $I(0)$ has been normalized to one and τ_{ww} is the lifetime in a Williams-Watts relaxation decay. If $I(t)$ is considered as arising from a superposition of exponential decays then the latter equation can be written as

$$\exp(-(t/\tau_{ww})^\alpha) = \int_0^\infty \exp(-t/\tau) \cdot \rho_{ww}(\tau) d\tau$$

Equation 8.1.03

where $\rho_{ww}(\tau)$ defines the distribution function of the Williams-Watts decay. Lindsey *et al.* 108 and Montroll *et al.* 109 rewrote the above expression to derive

$$\exp(-s^\alpha) = \int_0^\infty \exp(-sx) \cdot \lambda(x, \alpha) dx$$

Equation 8.1.04

where $\lambda(x, \alpha)$ is the inverse Laplace transform of $\exp(-s^\alpha)$. Using the substitutions

$$\begin{aligned} x &= \tau_{ww} / \tau \\ s &= t / \tau_{ww} \\ \lambda(x, \alpha) &= \frac{\tau_{ww}}{x^2} \cdot \rho_{ww}\left(\frac{\tau_{ww}}{x}\right) \end{aligned}$$

Equation 8.1.05

one can derive through contour-integration

$$\lambda(x, \alpha) = \frac{1}{\pi} \int_0^\infty \exp(-xu) \cdot \exp[-u^\alpha \cos(\pi\alpha)] \cdot \sin[u^\alpha \sin(\pi\alpha)] du$$

Equation 8.1.06

and thus

$$\rho_{ww}(\tau) = \frac{\tau_{ww}}{\tau^2} \cdot \lambda\left(\frac{\tau_{ww}}{\tau}, \alpha\right)$$

Equation 8.1.07

which can be numerically evaluated in computer software such as Mathematica. The parameter τ is the relative proportion or probability of a relaxation occurring at a particular lifetime τ_{ww} . Therefore, if one assumes a lifetime τ_{ww} of unity, then a plot of Equation 8.1.07 will reveal the distribution curve for lifetimes τ_{ww} at a particular stretching coefficient. The probability density $\tau \rho(\tau)$ is plotted versus τ/τ_{ww} , as seen in Figure 8.1.01.

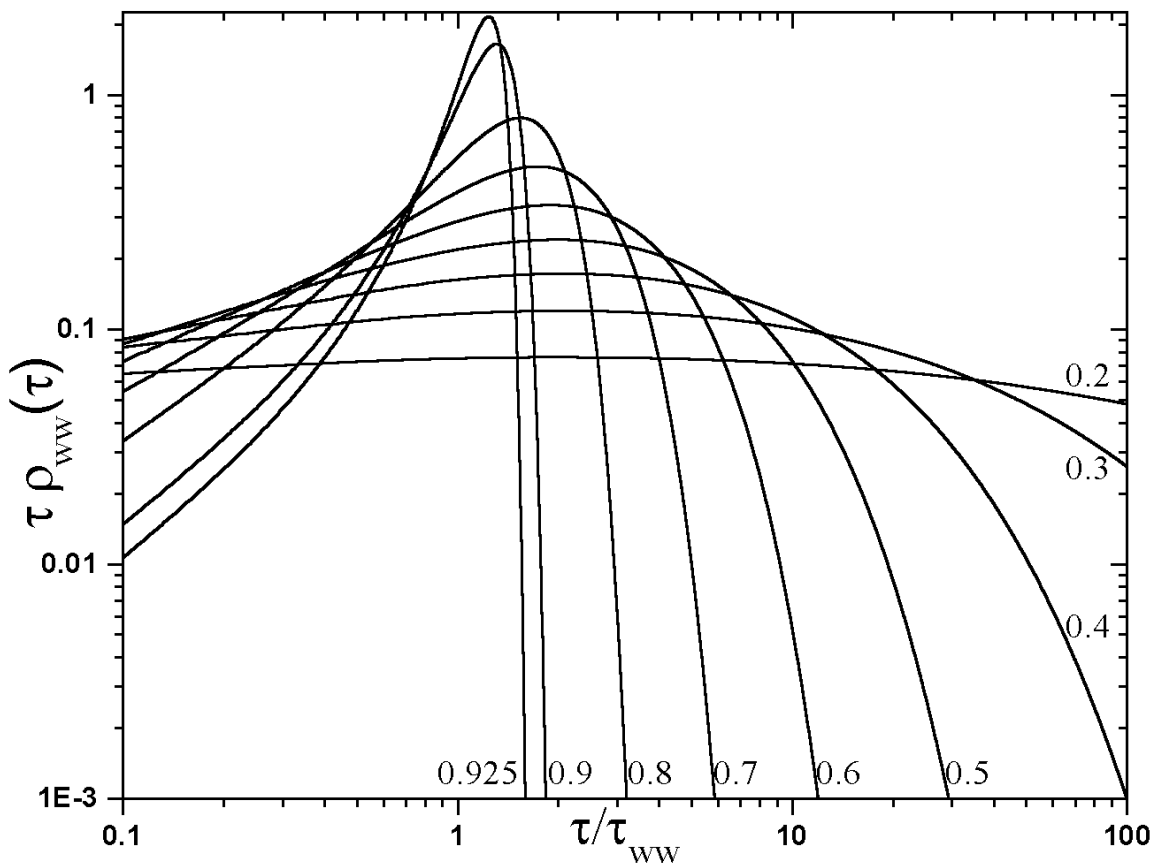


Figure 8.1.01. Probability density for the indicated stretching coefficients assuming a William-Watts lifetime τ_{ww} of unity.

If the stretching coefficient is unity, or a classical first-order decay, then the distribution would be a Dirac delta function centered at the lifetime, in this case one. It can be observed in Figure 8.1.01, and Equation 8.1.07, that as the stretching coefficient decreases the probability distribution profile broadens. Therefore, as the stretching coefficient decreases, an increase in the number of different lifetimes occurs or the probability of any single lifetime will decrease. It is for this reason that as the stretching coefficient decreases, it is assumed that the disorder of the system under study increases.

Decay Profiling and Fitting

The stretched exponential decay data were imported into an off-the-shelf software program, such as Microcal Origin for PCs, or Wavemetrics Igor for the Macintosh. These packages allow for user-defined expressions, equations, or algorithms to fit the experimental data to a function. Although these packages allow for the raw, unprocessed stretched exponential function, Equation 8.1.01, to be entered as a fitting expression, it has been determined that the values of α and τ can vary depending on the choice of the initial fitting parameters. To achieve more consistent and accurate results, it has been advantageous to linearize the stretched exponential function. This process begins with by taking the natural logarithm of both sides of Equation 8.1.01, which yields the intermediate step

$$\text{Ln}\left(\frac{I(0)}{I(t)}\right) = \left(\frac{t}{\tau}\right)^\alpha$$

Equation 8.1.08

taking the natural logarithm again will yield the final result of

$$\text{Ln}\left(\text{Ln}\left(\frac{I(0)}{I(t)}\right)\right) = \alpha \text{Ln}(t) - \alpha \text{Ln}(\tau)$$

Equation 8.1.09

Therefore, plotting the data as the ln-ln of the intensity ratios on the y-axis against the ln of time on the x-axis will allow for a linear regression with the slope as α and the y-intercept as $-\alpha \text{Ln}(\tau)$, or

$$\begin{aligned}\alpha &= m \\ \tau &= \exp(-b/m)\end{aligned}$$

Equation 8.1.10

where m is the slope and b is the y-intercept of the linear regression. An example of the plotted data and the linear regression is shown in Figure 8.1.02.

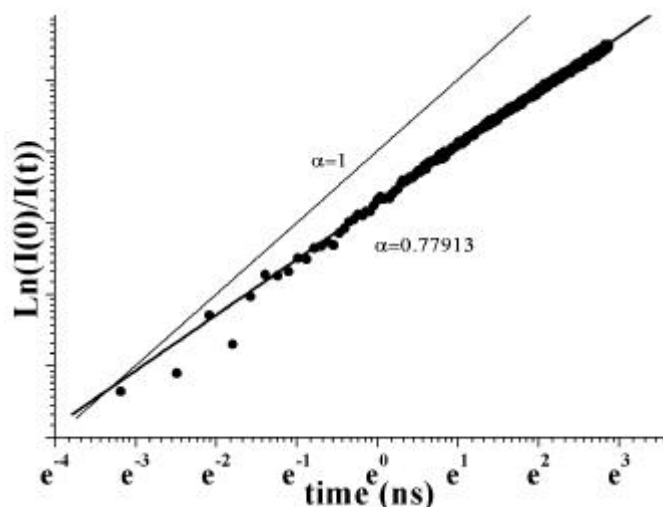


Figure 8.1.02. Fluorescence decay plotted as $\text{Ln}(I(0)/I(t))$ vs. time, on a ln-ln scaled graph.

This method of processing the stretched exponential data ensures accurate and consistent fitting. It also allows a standard assessment of the fit deviation through the regression variance or correlation. As can be seen in Figure 8.1.02, an excellent data-to-regression fit is observed with a linear correlation of 0.99792.

8.2. Photoluminescence

The static or steady-state photoluminescence of copoly(HBA/HNA) was observed using two instruments. A Hitachi Fluorescence Spectrometer Model F-4500 was used to obtain the fluorescence and phosphorescence response of copoly(HBA/HNA) at ambient conditions. This spectrometer will provide a three dimensional profile of the excitation on the x-axis, emission on the y-axis, and the corresponding intensity profile on the z-axis. The second instrument was a Spex FluoroMax Spectrofluorometer. It provides

separate two dimensional excitation and emission spectra. The results from both instruments were used to compliment each other.

The fluorescence of copoly(HBA/HNA) is seen in Figures 8.2.01 and 8.2.02. Figure 8.2.01 is a fluorescent contour plot of the excitation and emission versus the intensity. There exists a single strong peak with a maximum excitation of 380 nm (3.26 eV) and emission of 422 nm (2.94 eV).

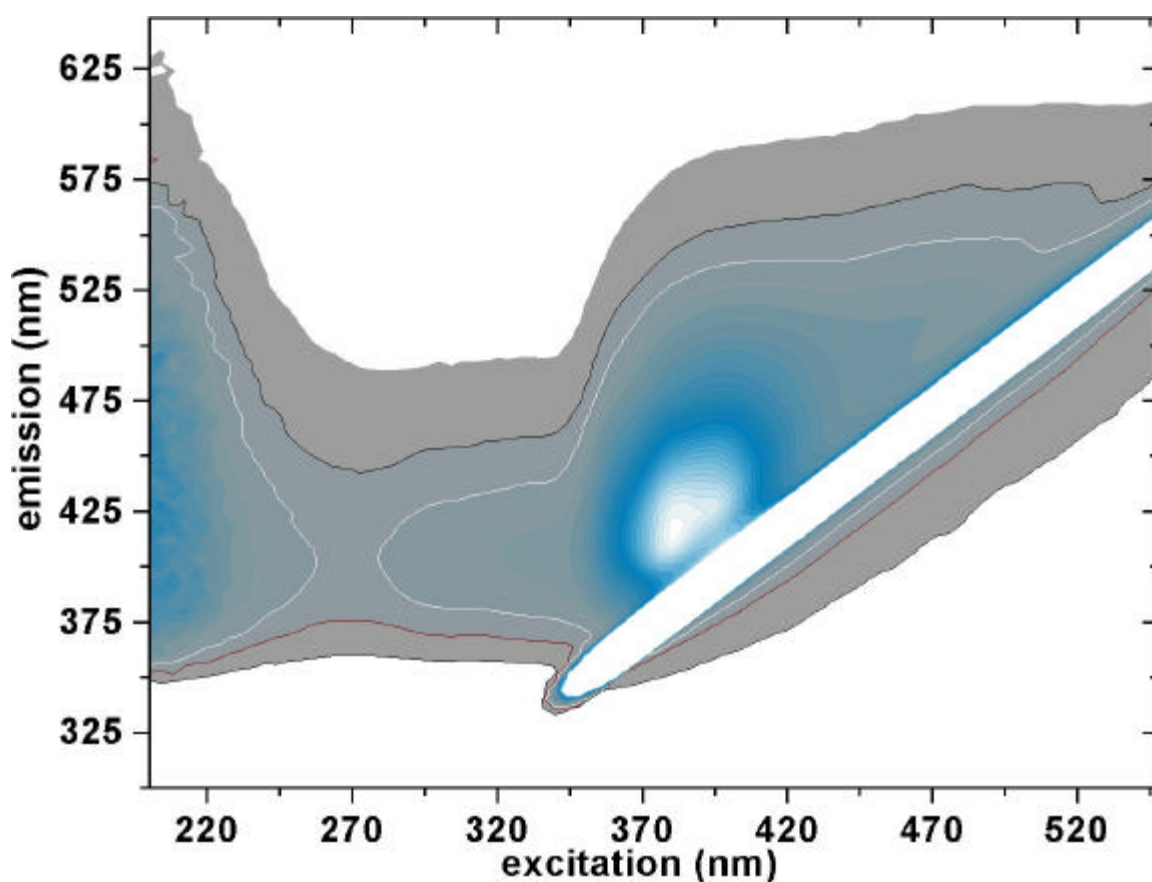


Figure 8.2.01. Fluorescence contour plot of a 75 μm copoly(HBA/HNA) film at ambient conditions.

The fluorescent contour plot clearly shows that there exists only a single fluorescence peak. The long white diagonal strip through the contour plot is simply the source light scattering from the lamp.

Figure 8.2.02 is the traditional method for reporting excitation and emission responses. In excitation mode, the FluoroMax will scan the entrance or incident monochromator on the sample. A fixed collection monochromator and detector will monitor the polymer's fluorescent response, in this case 420 nm (2.95 eV). The excitation mode will reveal the maximum excitation wavelength for the sample. Figure 8.2.02.A shows that the maximum excitation wavelength for copoly(HBA/HNA) is 372 nm (3.33 eV).

In emission mode, the FluoroMax will allow the user to fix the excitation or incident light at the maximum excitation wavelength, in this case 380 nm (3.26 eV). The collection monochromator is then scanned to produce the emission spectrum. Figure 8.2.02.B shows that the maximum emission wavelength of copoly(HBA/HNA) is 422 nm (2.94 eV).

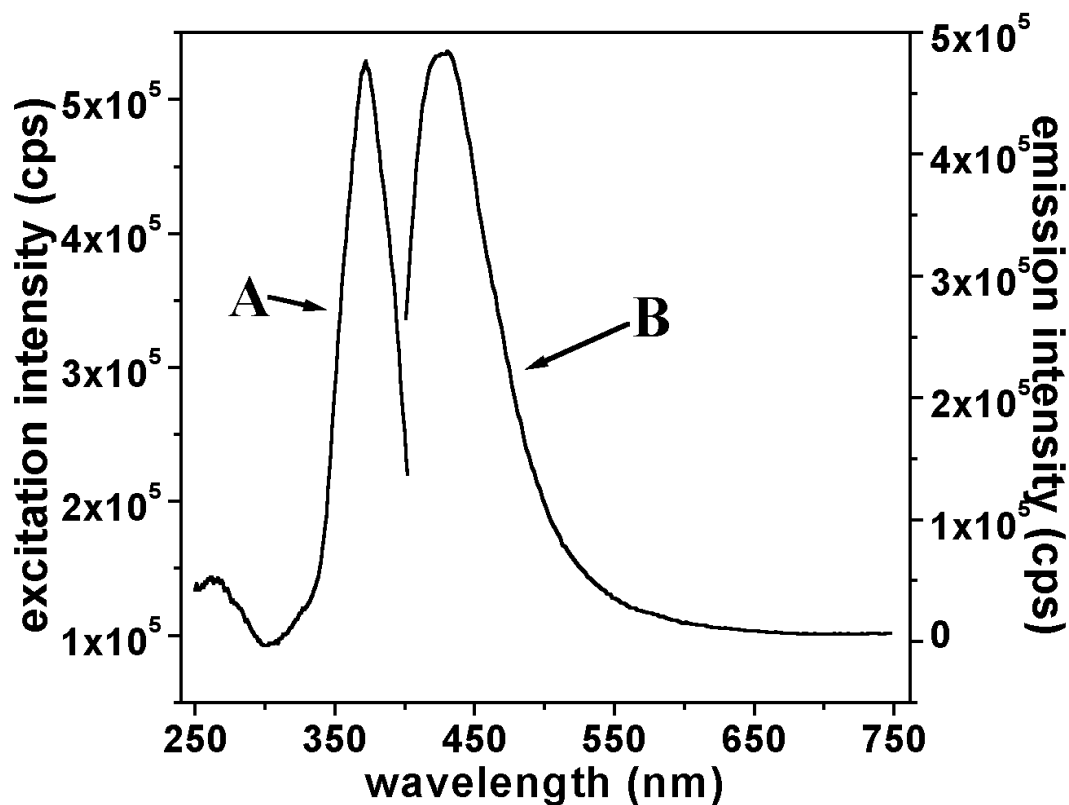


Figure 8.2.02. Fluorescence excitation (A) and emission (B) spectra for a 20 μm copoly(HBA/HNA) film at ambient conditions. Excitation was monitored at 420 nm (2.95 eV) and emission was excited at 380 nm (3.26 eV).

In summary, both spectrofluorometers reveal consistent fluorescent responses.

Copoly(HBA/HNA) will absorb light in the range of 372 to 380 nm (3.33 to 3.26 eV) for an optimum fluorescence emission. The excited polymer will fluoresce at a maximum of 422 nm (2.94 eV), with a long tail extending into the infrared region.

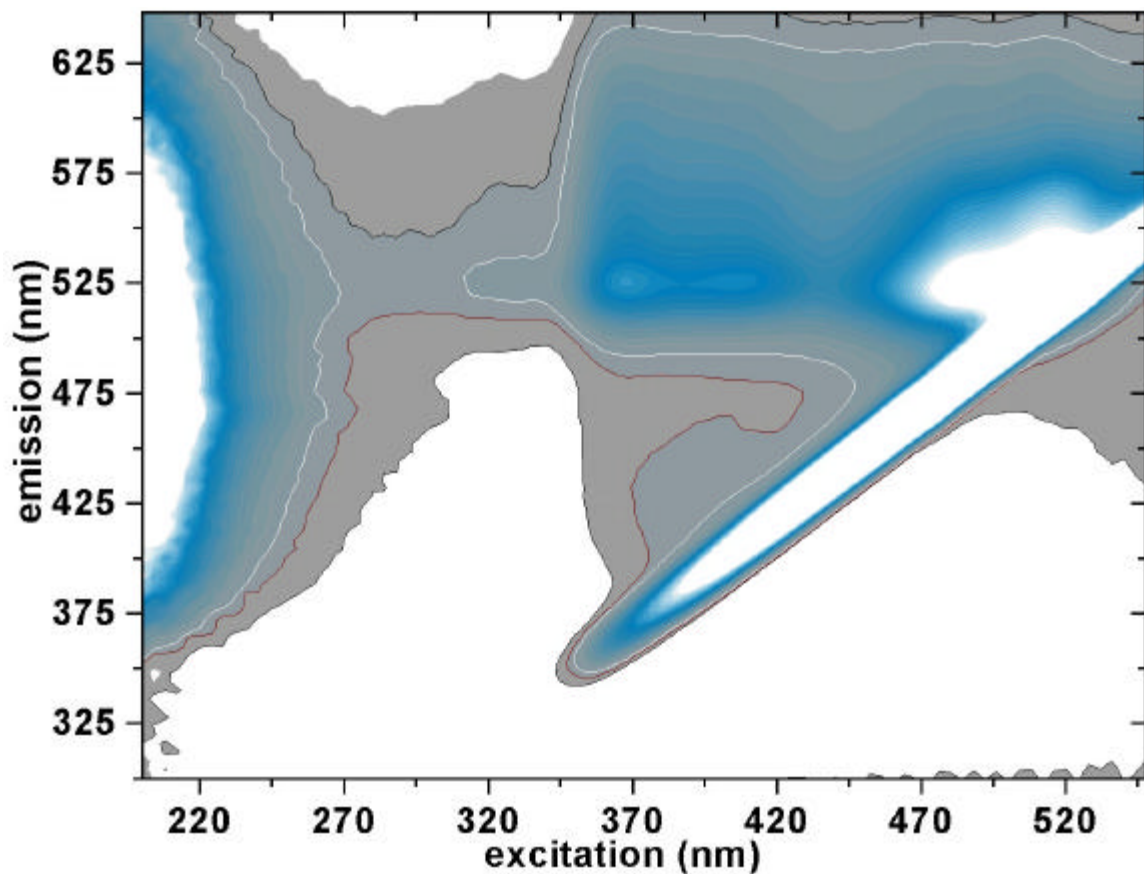


Figure 8.2.03. Phosphorescence contour plot of a 75 μm copoly(HBA/HNA) film at ambient conditions.

Figure 8.2.03 reveals that copoly(HBA/HNA) does phosphoresce with two broad peaks. The first peak has an excitation range of 367 to 410 nm (3.38 to 3.02 eV) and an emission maximum at 525 nm (2.36 eV). The second peak is stronger than the latter first peak, and has an excitation range of 473 to 530 nm (2.62 to 2.34 eV) and an emission range of 512 to 551 nm (2.42 to 2.25 eV). Both phosphorescent peaks have long tails that extend into the near infrared.

8.3. Time-Resolved Photoluminescence

Experimental

A detailed study of the time-resolved fluorescence response of copoly(HBA/HNA) has been studied using the streak camera apparatus as described in Chapter 4 – Photoluminescence. The streak camera provides the data in three dimensional arrays in which the x-axis is wavelength in nm, the y-axis is time in ns, and the z-axis is intensity. A typical time resolved contour plot of copoly(HBA/HNA) is shown in Figure 8.3.01.

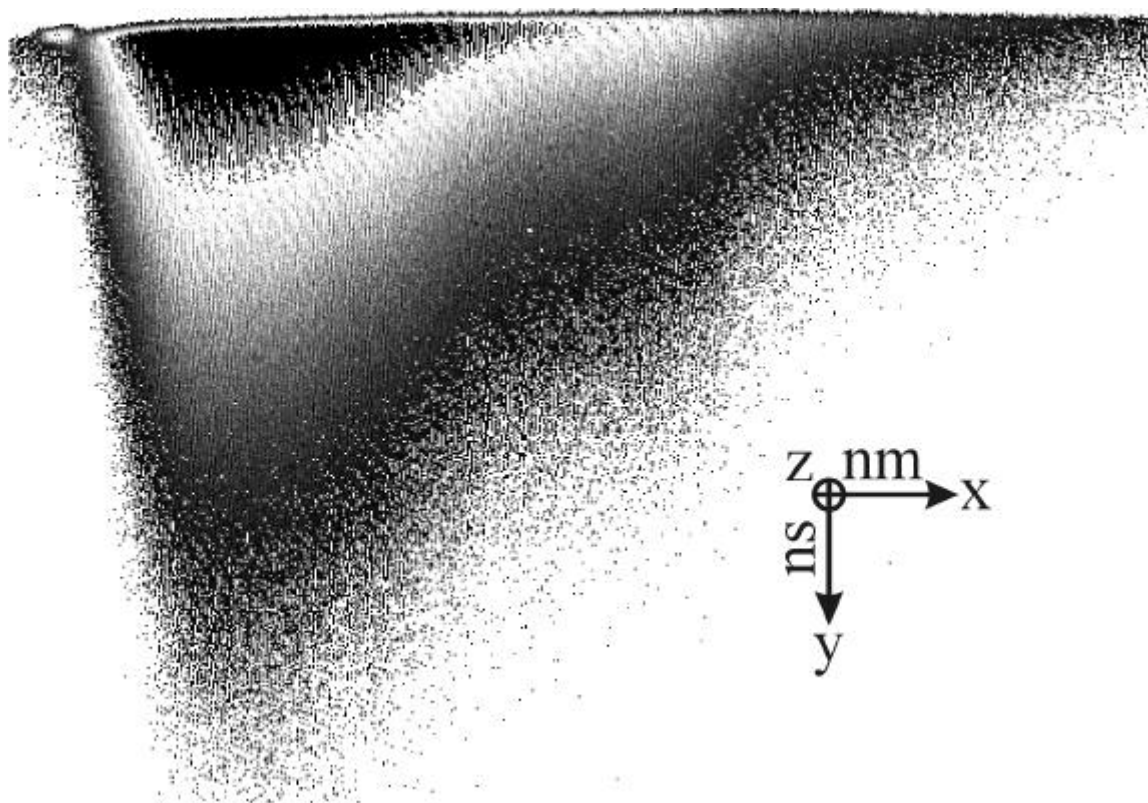


Figure 8.3.01. Typical time resolved spectrum from a streak camera of a 75 μm copoly(HBA/HNA) film at ambient conditions.

The wavelength and time components of the above contour map are derived by designating thin x-axis or y-axis slices, respectively. The y-axis or x-axis data, respectively, within these slices are then averaged to generate a classical two dimensional plot. For example, to retrieve the time decay at a particular wavelength, a thin slice can be designated with the long axis parallel to the time (y) axis and centered about the desired wavelength. A conversion utility can then iterate for each time and calculate the average intensity within the wavelength width. All time resolved slices were within ± 5 nm of the desired wavelength. In other words, the time slice translates the three dimensional data into a classical two dimensional time decay profile centered at a particular wavelength. In summary, the streak camera allows for the simultaneous collection of time resolved data at various wavelengths.

The initially collected data was first fit using various fitting functions, as shown in Figure 8.3.02. The relaxation functions used were the classical first-, second-, and third-order exponential decay and the stretched first- and second-order exponential decay. The classical first-order decay produced the worst results, with a χ^2 of ten times that of the stretched first-order exponential. Additionally, if the data did in fact conform to a classical first-order decay, then fitting the data against the stretched exponential decay would simply converge the stretching coefficient α to unity.

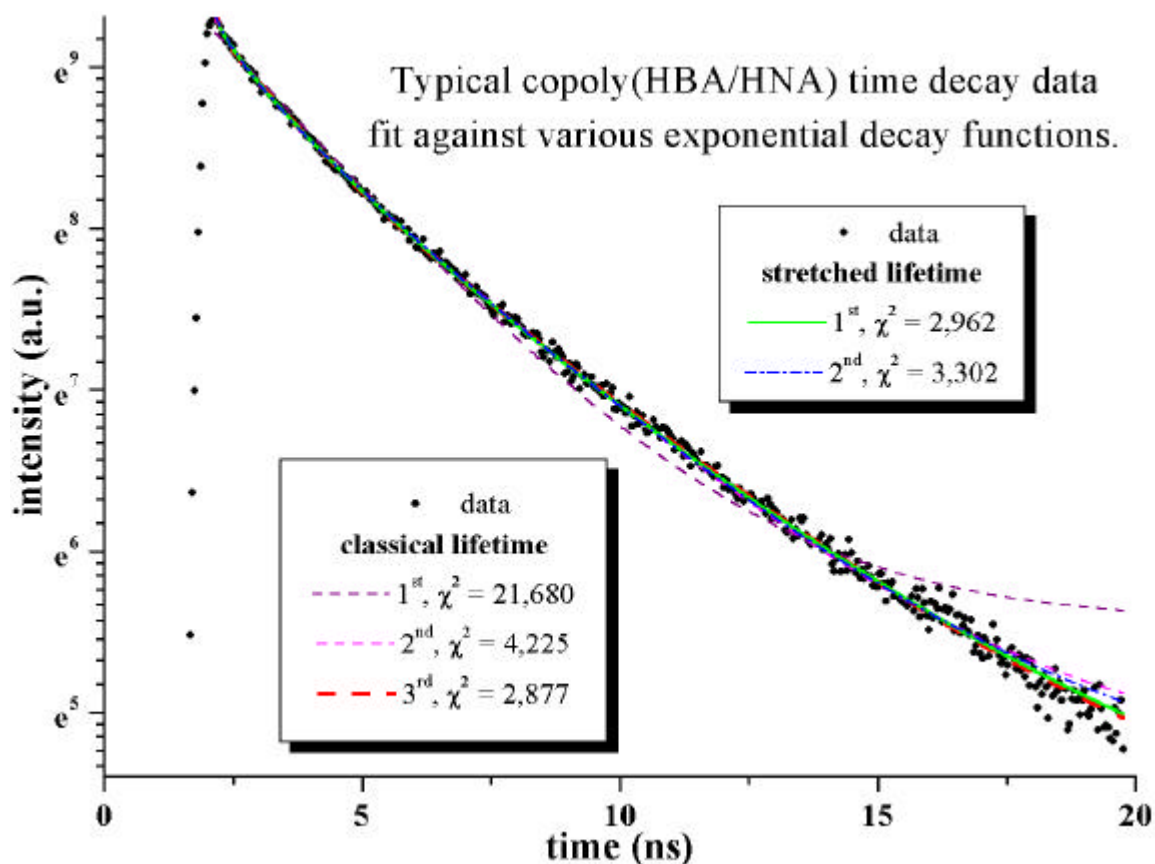


Figure 8.3.02. Typical copoly(HBA/HNA) time resolved decay data against various exponential decay functions.

The classical third-order decay did produce slightly better fits as compared with the stretched first-order decay, however, a visual inspection of the data did not clearly reveal the presence of three distinct lifetimes. Additionally, a third-order decay is widely accepted as an ungraceful method of fitting because of the large number of fitting parameters inherent in the equation. Therefore, the stretched first-order exponential decay was chosen as the fitting relaxation function for the copoly(HBA/HNA) samples.

Results

Once the stretched first-order exponential decay or the Williams-Watts relaxation was chosen, all time decay profiles were processed and linearized, as shown in Figure 8.3.03, and as outlined in Section 8.1 - General Foundations, Decay Profiling and Fitting. Taking the signal to noise ratio of the spectrum into consideration, all fits, thereafter, had a linear correlation of 0.94 or better.

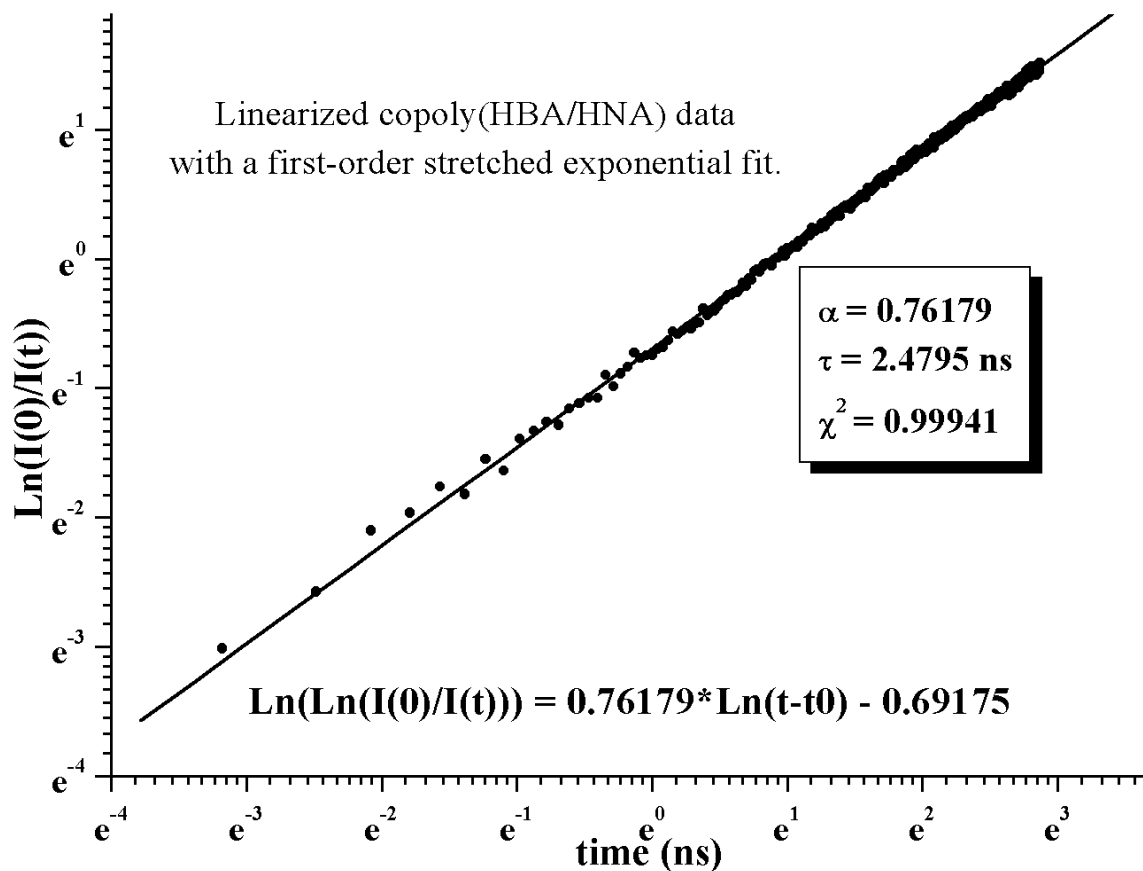


Figure 8.3.03. Typical copoly(HBA/HNA) time resolved decay data linearized and fit against a first- order stretched exponential decay function.

The equipment used is outlined in detail in 4.2 - Time-Resolved Fluorescence. To summarize this section, a 400 nm pulsed laser with a pulse width of 250 fs and a repetition rate of 250 kHz is incident on a sample of copoly(HBA/HNA) at ambient temperature and pressure. This light is collected from the sample and focused into a

streak camera, which generates a three dimensional contour plot of the spectrum and time decay versus intensity data.

Initially two sets of experiments were performed. The polymer's time-resolved response as a function of the thin film thickness and average incident laser power. The copoly(HBA/HNA) samples tested had a thickness range from 10 μm to 75 μm .

Although the intensity of the collected light varied, the Williams-Watts stretching coefficient α and the time decay τ did not appreciably vary with thickness. In a similar manner, the average incident laser power ranged from 0.25 mW to 20 W with no appreciable change in α or τ . Although some burning did occur on the sample at high energy, the time required to observe such damage was on the order of hours.

Polarization studies were then performed on the sample to observe if the fluorescence is sensitive to the relative angle between the incident electric vector and the molecular chain orientations. A Glan-Foucault prism was placed prior to the sample and rotationally oriented to maximize the laser output. This polarizer was used to ensure that the electric vector from the laser and incident on the sample was of a single direction. A sample of extruded 75 μm copoly(HBA/HNA) films was placed directly after this polarizer in which the molecular chain orientations were either rotationally parallel or perpendicular to the incident electric vector. A second Glan-Foucault prism was placed directly after the sample and possessed either a rotationally parallel or perpendicular orientation as compared to the first polarizer or incident polarization. Therefore, four orientations were studied, parallel/parallel, parallel/perpendicular, perpendicular/parallel, and

perpendicular/perpendicular, where each designation is the (molecular chain)/(collection polarizer) orientations relative to the incident polarizer.

Each polarization study revealed no appreciable change in α and τ between the different orientations. Therefore, the fluorescence excitation mechanism of copoly(HBA/HNA) is not dependent on the relative orientation between the incident electric field and the molecular chain axis. Additionally, the fluorescence emission dynamics are constant at various emission polarizations. The total collected power from each study did vary. The parallel/parallel study emitted the strongest signal, whereas the perpendicular/parallel emitted the weakest of the four configurations. This observation is simply understood by passing linearly polarized light through three polarizers. The greatest signal observed will be when the three polarizers are rotationally parallel or in perfect alignment, and the weakest signal will be when the neighboring polarizers are rotationally crossed or 90° out of alignment.

The parallel/parallel study provided the greatest signal, its streak contour was further studied to correlate an emissive wavelength dependence in α and τ , as shown in Figure 8.3.04.

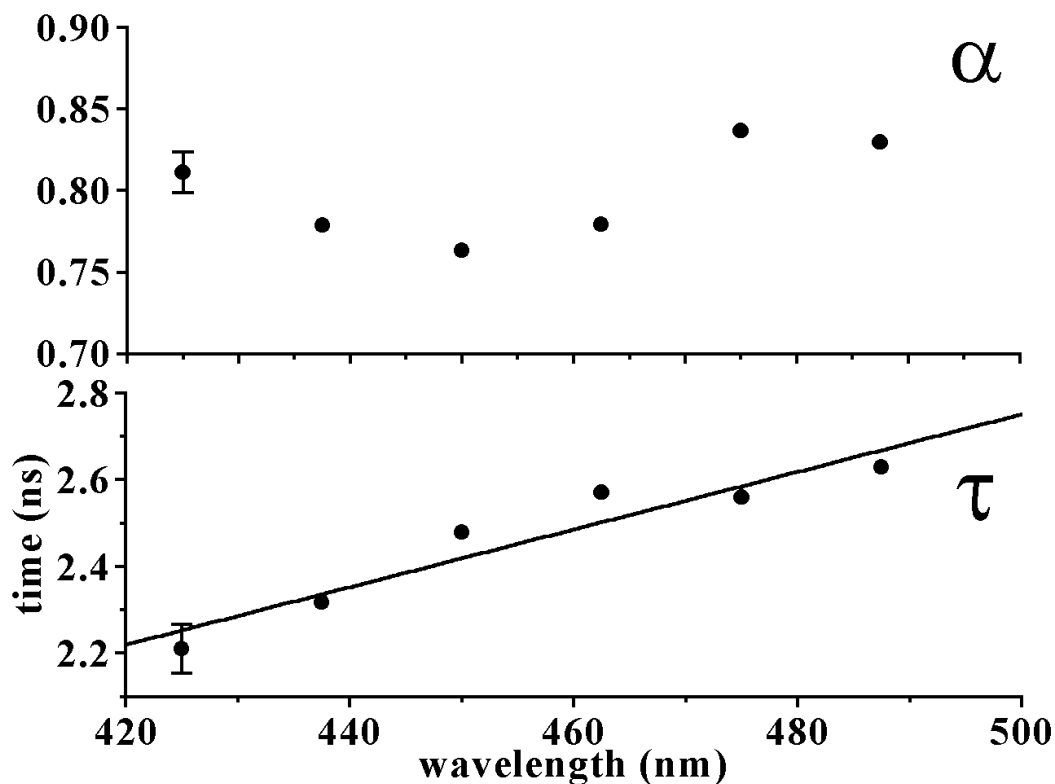


Figure 8.3.04. Wavelength dependence of the stretching coefficient α and the Williams-Watts lifetime τ for a 75 μm copoly(HBA/HNA) film under parallel molecular orientation/parallel emission polarization at ambient conditions.

Discussion

As can be seen in Figure 8.3.04, there does not exist an apparent trend in the stretching coefficient, α , with changing emissive wavelength. However, the Williams-Watts lifetime does possess an increase as the emission wavelength increases. Bässler's *et al.* time-resolved studies of PPV 110·104·102·105·111, suggested that this behavior can be due to migration or relaxation of the excited state in the tail region of the density of states (DOS).

In general, Fermi's Golden Rule is

$$\tau^{-1} = \text{rate} = \frac{2\pi}{h} \rho \langle H' \rangle^2$$

Equation 8.3.01

where h is Planck's constant, ρ is the density or number of final states capable of coupling to the initial state, and $\langle H' \rangle$ represents the matrix element for the perturbation coupling the initial and final states¹¹. This equation clearly states that as the number of excited to ground states decrease, then the lifetime increases. The steady-state emission spectrum of Figure 8.2.02 clearly shows that the emission maximum of copoly(HBA/HNA) is 422 nm (2.94 eV), and then decreases in emission intensity thereafter. This spectrum proves that the density of states ρ is decreasing with increasing wavelength after the maximum of 422 nm (2.94 eV). Therefore, the increasing trend of the Williams-Watts lifetime with wavelength, as shown in Figure 8.3.04, is simply a matter of a decrease in the number of coupled excited to ground states, as shown by Fermi's Golden Rule, Equation 8.3.01, and the emission spectrum for copoly(HBA/HNA), Figure 8.2.02.

As discussed and referenced in Section 8.1 - General Foundations, Stretched Exponential Lifetimes, the stretching coefficient is usually correlated with the presence of disordered relaxation. In the case of copoly(HBA/HNA), the relaxation is the optically based

fluorescent emission. A total of 45 experiments were performed, which included varying the sample thickness, incident and emissive polarization, and incident energy, to reveal that the average stretching coefficient α is 0.78 ± 0.06 with a Williams-Watts lifetime τ of 2.30 ± 0.24 ns for all samples. Therefore, copoly(HBA/HNA) possesses a fairly constant stretching coefficient and lifetime. Since the stretching coefficient is not unity, it is clear that this random liquid-crystalline copolyester possesses a fair amount of static and/or dynamic disorder. All of these experiments were performed at room temperature, approximately 25°C (298 K), in which a significant degree of intrachain monomeric rotations occur. The following section, 8.4 - Thermal Photoluminescence, temperature dependent experiments were performed to distinguish if the polymer possesses only static disorder, which is based on purely energetic or structural factors, or dynamic disorder, which may be based on exciton migration factors between a donor and acceptor functional group.

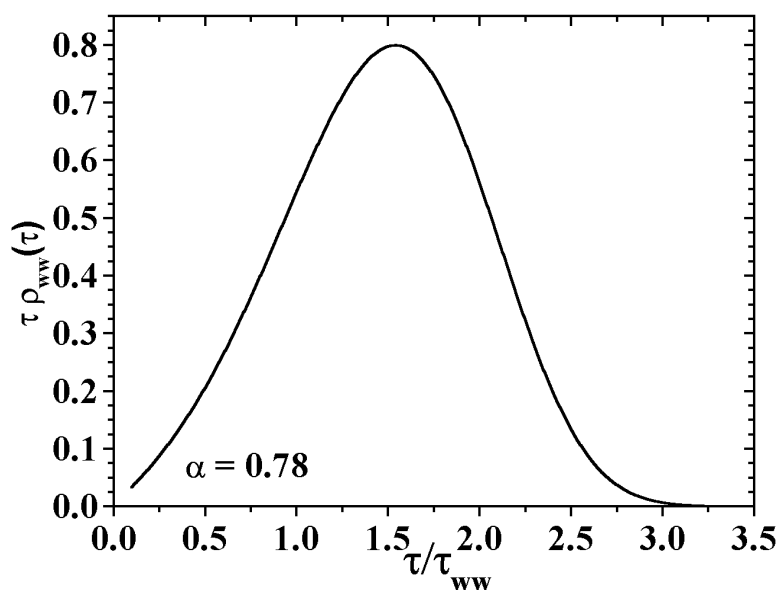


Figure 8.3.05. Probability density for copoly(HBA/HNA), assuming a William-Watts lifetime τ_{ww} of unity.

Figure 8.3.05 is simply shown to reveal the probability density for copoly(HBA/HNA) based on the above reported average result of 0.78 for the stretching coefficient. As can be seen, there exists a definite distribution of lifetimes with the most probable around 1.5 ns and a full width at half maximum of 1.4 ns.

8.4. Temperature Dependent Photoluminescence

Results

The temperature-dependent fluorescence emission energy and time-resolved spectra of copoly(HBA/HNA) were obtained using the Hamamatsu Streak Camera in a complete apparatus previously discussed in Section 4.2 - Time-Resolved Photoluminescence, with detailed data processing described in Section 8.3 - Time-Resolved Photoluminescence, Data Collection and Processing. All of these instrumental and data analysis techniques will be further employed in the following section to explore the temperature-dependent fluorescence emission of copoly(HBA/HNA).

Two temperature apparatuses were used to control the temperature of the copoly(HBA/HNA) sample. A nitrogen cooled cryostat and an oxygen-free copper sample mount coupled to a high temperature hotplate. The temperatures of both systems were monitored and controlled with calibrated thermocouples and temperature controllers. A total of seventy temperature-dependent experiments were performed on copoly(HBA/HNA) ranging in temperature from -180 to +398 °C. Except for the 398 °C run, all temperatures were

taken at 10 °C intervals. Since a large amount of data existed, the wavelength dependent spectra were first obtained from each run to derive the emission maximum. Figure 8.4.01 reveals the emission maxima versus temperature for these seventy experiments.

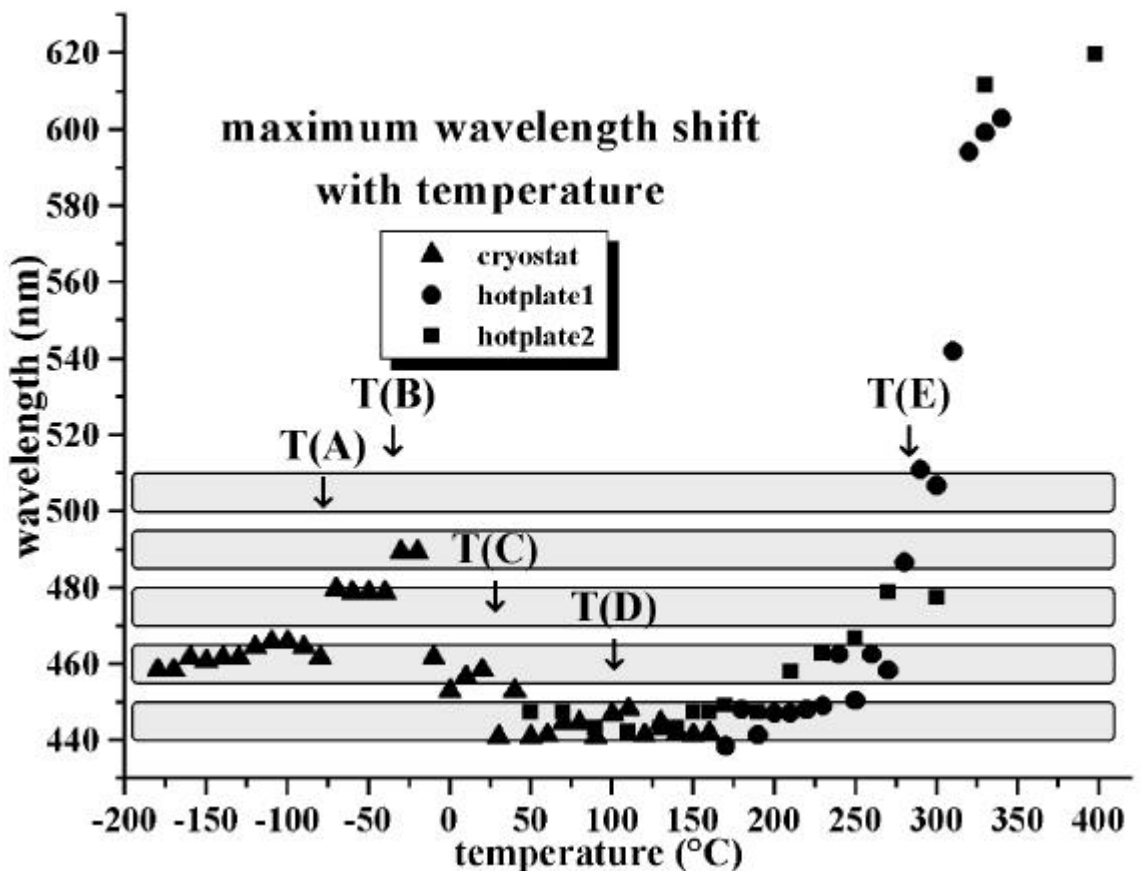


Figure 8.4.01. Temperature-dependent fluorescence emission maxima of a 75 μm copoly(HBA/HNA) extruded thin film.

The cryostat and hotplate had an overlapping temperature range from 50 to 160 °C. The temperature overlap proved that consistency existed between different runs and different temperature controller apparatus. This is clearly seen in Figure 8.4.01 where the overlapping temperature range has consistent maximum wavelength shifts with both controllers and as many as three separate runs for each temperature. Therefore, different

samples, or runs, of copoly(HBA/HNA) revealed consistent results at the indicated temperatures.

Phase transitions for copoly(HBA/HNA) are discussed in Section 6.3 - Phase Transitions. Each of the four phase transitions predominate in the wavelength maxima shifts of Figure 8.4.01. The huge red-shifted emission maxima increase at 280 °C, T(E), corresponds to the isotropic melt T_m . The flat area at 100 °C, T(D), corresponds to the α or T_g transition. The decrease in wavelength at room temperature T(C) corresponds to the local HNA rotations, or the β transition. And the γ transition can be seen in the region at T(A) and T(B) which may reveal two forms of local HBA or phenylene rotations.

Alhaj-Mohammed *et al.*⁶⁶ suggest two distinct forms of the γ phase transition. The first form would be a single local HBA rotation, and the second would be two neighboring HBA monomers counter rotating about each other. The latter may be considered an anti-torsional dimer. Alhaj-Mohammed suggested this scenario because of the low dielectric signal detected from the HBA rotation. The anti-torsional motion would essentially cancel the macroscopic signal, and thus decrease the dielectric detection of the γ phase. Figure 8.4.01 does reveal two distinct steps, T(A) and T(B), in the range of the local HBA rotations. Based on the relative temperatures and energy shifts, the T(A) may be attributed to the single HBA torsion and the T(B) may be attributed to the anti-torsional dimer rotation. Further experimentation and/or modeling would be required to concretely determine the latter assignments.

Figure 8.4.01 illustrates five horizontal bands. Each band represents a time-resolved study centered at the indicated wavelength with a width of ± 5 nm of all seventy temperature experiments. The five time-resolved studies ranged from 445 to 505 nm, in 15 nm increments. The 505 nm time-resolved band is below the phosphorescence emission, as shown in Figure 8.2.03, therefore all of the following time-resolved data acquisition and processing is based on only the fluorescence emission.

The following two graphs, Figures 8.4.02 and 8.4.03, reveal the temperature dependencies of the stretching coefficient α and the Williams-Watts lifetime, respectively. Careful inspection of the plots reveal that between the five bands, from 445 to 505 nm, there does exist the wavelength dependence as discussed in Section 8.3 - Time-Resolved Photoluminescence, Results and Discussion, and as illustrated in Figure 8.3.04. Therefore, the 0.4 ns increase versus wavelength dependence of Figure 8.3.04 is also seen in the wavelength versus lifetime plot of Figure 8.4.03.

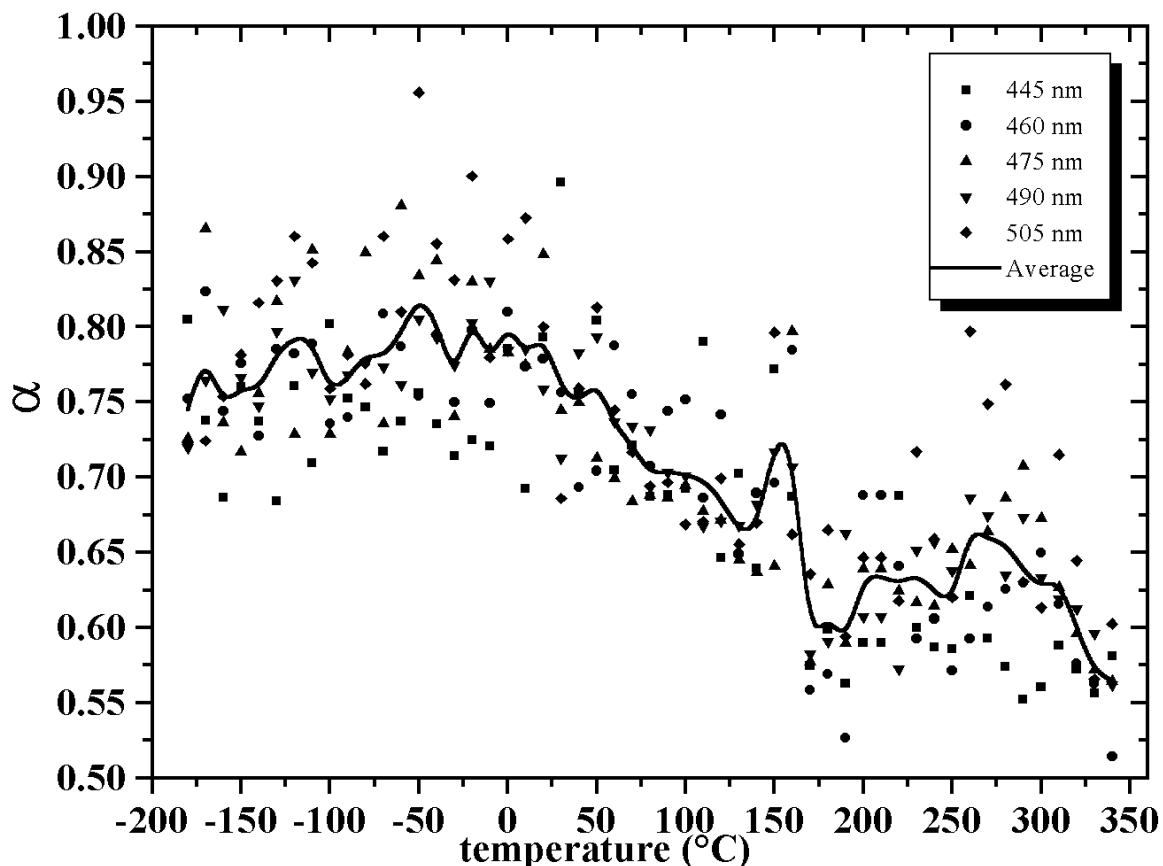


Figure 8.4.02. Temperature dependence of the stretching coefficient α for a 75 μm copoly(HBA/HNA) extruded thin film.

As can be seen in both figures, at low temperatures the data is basically constant, with a slight increase, up to room temperature. The plots then decrease with some variation and a possibility of a vertical asymptote at approximately 160 °C. The physical nature of this is currently unknown, it may be a sign of molecular or chain reorientation, a form of ionic conduction, the beginning of the isotropic melt T_m , the fluorescence emission is affected by intermolecular interactions or 3D reordering, or other excited state relaxation processes replacing or competing with the fluorescence emission. Further research in this temperature range may yield a more detailed understanding.

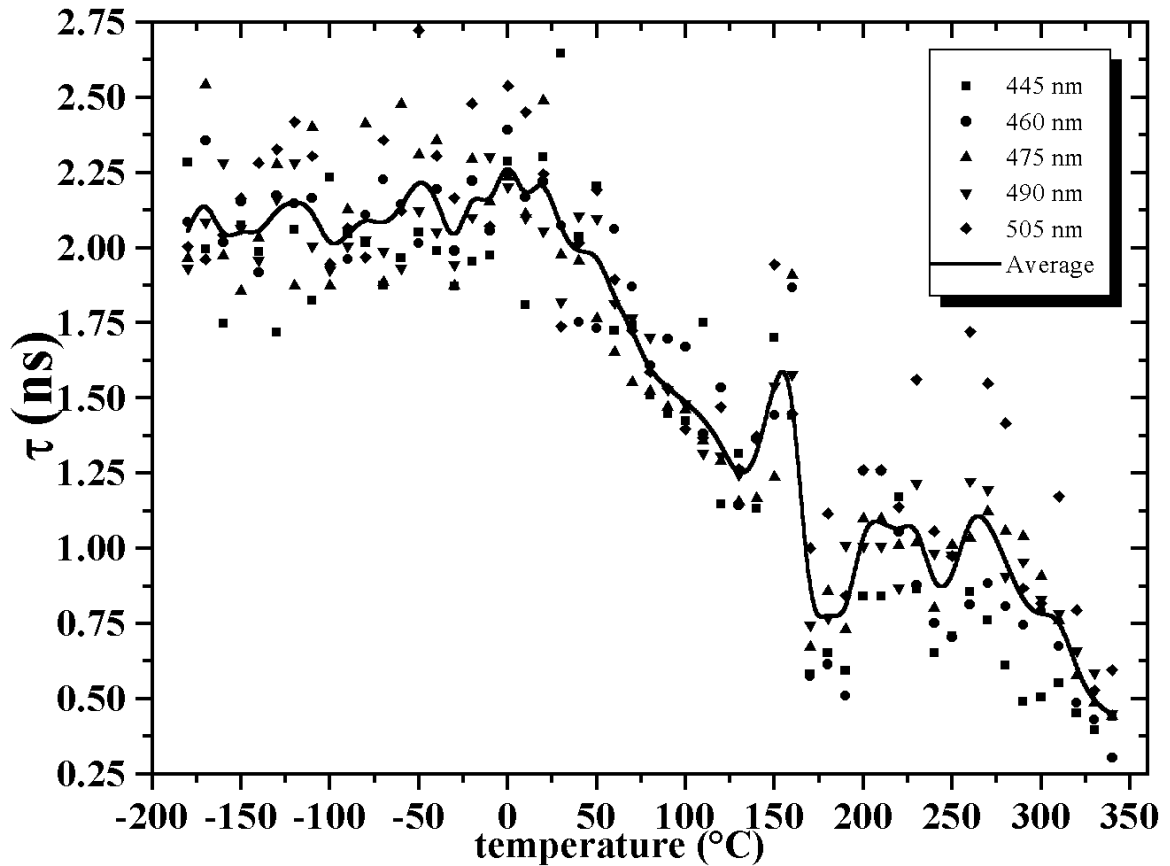


Figure 8.4.03. Temperature dependence for the Williams-Watts lifetime for a 75 μm copoly(HBA/HNA) extruded thin film.

In the 1880's, Svente Arrhenius developed an empirical equation relating the rate of a reaction to its temperature dependence. This equation is

$$\text{rate} = k_1 \exp\left(-\frac{E_a}{RT}\right)$$

Equation 8.4.01

where $\text{rate} = 1/\tau$, k_1 is the amplitude of the fit, E_a is the activation energy of the reaction, relaxation, or process, R is the gas constant, and T is the temperature. Figure 8.4.03 clearly shows two distinct, a constant and decreasing, temperature regions. Equation

8.4.01 can be rewritten in a natural log form to linearize the data. Figure 8.4.04 is the temperature-dependent copoly(HBA/HNA) Arrhenius plot of Ln(rate) versus the inverse of the temperature.

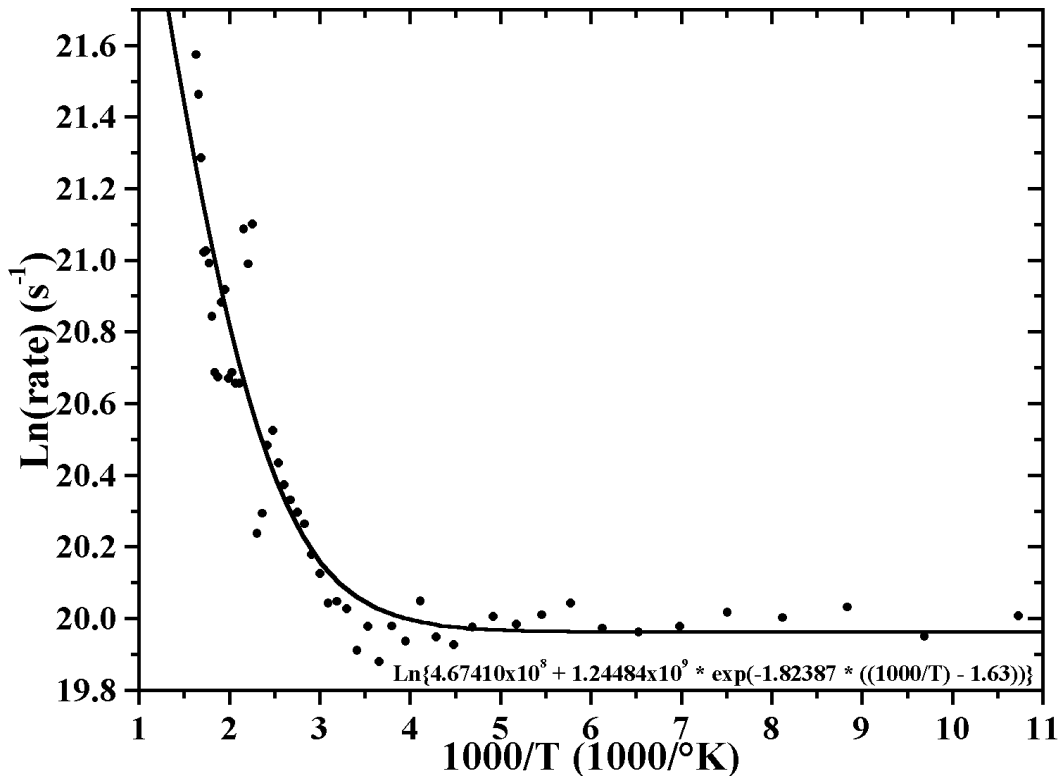


Figure 8.4.04. Arrhenius plot of the averaged five wavelength band Williams-Watts lifetime data for a 75 μm copoly(HBA/HNA) extruded thin film.

The above Figure 8.4.04 clearly distinguishes a constant horizontal region and a decreasing region. The above plot was fit against a modified Arrhenius equation.

$$\text{rate} = k_0 + k_1 \exp\left(-\frac{E_a}{RT}\right)$$

Equation 8.4.02

where the k_0 will allow the constant temperature region to fit in conjunction with the decreasing Arrhenius region. It also allows for the curved transition region between these two regions to aid in the demarcation of the of the decreasing Arrhenius region. Figure 8.4.05 shows the 35 data points of the decreasing region in a true Arrhenius plot and a linear least squares fit.

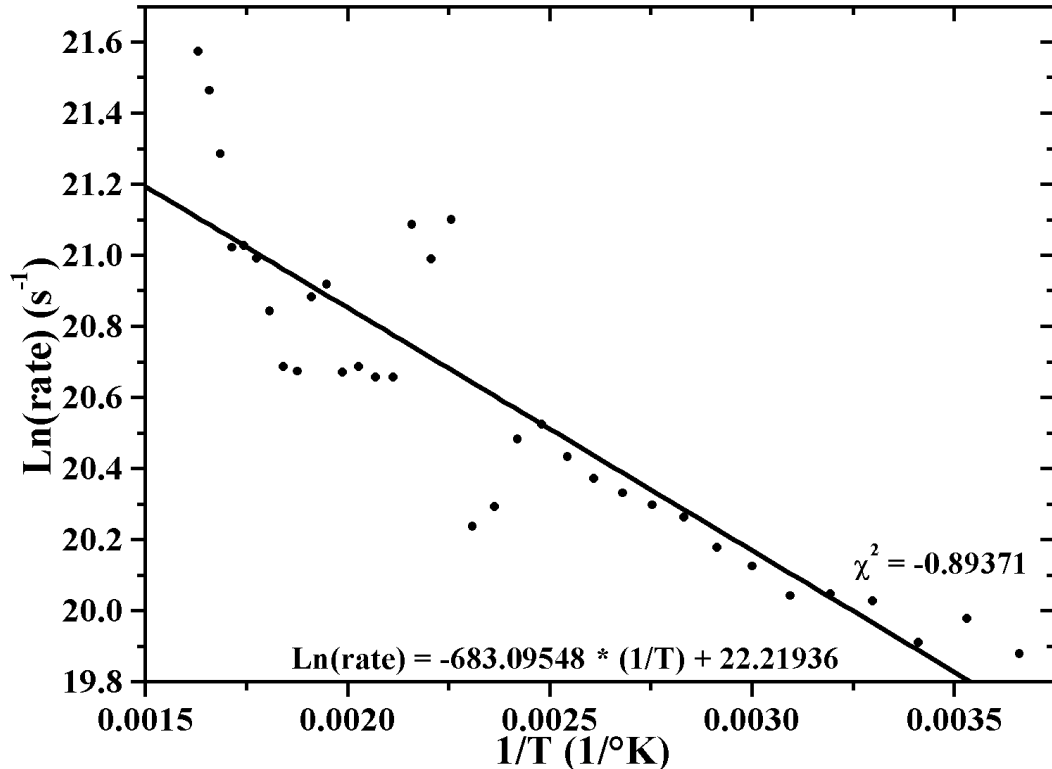


Figure 8.4.05. Arrhenius plot and linear regression of the temperature dependent data for a 75 μm copoly(HBA/HNA) extruded thin film.

The linear regression of Figure 8.4.05 will directly lead to the magnitude of the activation energy E_a via

$$E_a = -R \cdot (\text{slope}) = -(1.987 \times 10^{-3} \frac{\text{kcal}}{\text{K} \cdot \text{mol}}) \cdot (-683.09548 \cdot \text{K}) = 1.357 \frac{\text{kcal}}{\text{mol}} = E_a$$

Equation 8.4.03

therefore, the Arrhenius relationship of the decreasing temperature dependent region reveals an activation energy of 1.357 kcal/mole for the fluorescence emission within copoly(HBA/HNA). This energy is fairly low, hence copoly(HBA/HNA) proves to be a useful, stable, and high temperature material with a strong, low activation energy fluorescent emitter.

Discussion

The excitation of copoly(HBA/HNA) occurs with the copolyester absorbing energy from the incident light. The absorption edge of the HNA monomer terminates at approximately 350 nm (3.54 eV) as shown in the absorption spectrum of Figure 6.2.02.

This excited HNA monomer would have the form

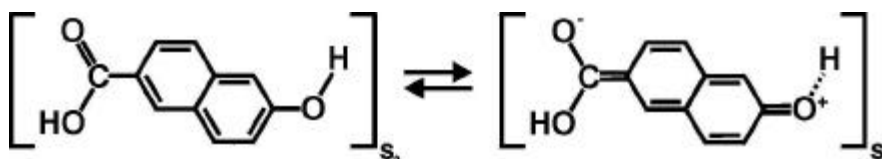


Figure 8.4.06. Ground and excited state of HNA upon optical absorption.

The incident light for all of the photoluminescence experiments presented, was at 400 nm (3.10 eV), which is beyond the absorption range for the pure HBA and HNA monomers. However, since the copolyester exhibits inherent strong π -orbital conjugation, then absorption of the 400 nm (3.10 eV) light is either through an extension of the absorption edge via perturbative conjugation of a single HNA monomer or through the absorption by

adjoining multiple HNA monomers, such as a conjugated dimer or trimer of HNAs. It is also conceivable to have a combination of the latter two effects.

The long absorption tail of copoly(HBA/HNA), as seen in Figure 6.2.02, that begins at 350 nm (3.54 eV) and extends into the near infrared reveals the extent of the conjugation effects, strengths, and/or lengths, and thus the broad-band absorbing strength of the HNA content within the copolyester. Figure 8.4.07 is a concept illustration to express the simplified basis of the energy continuum and the long absorption tail by revealing that the HNA monomers will have a lower energy than the HBA monomers, and increasing the number of adjacent multiple monomers will therefore decrease the energy within that spatial realm.

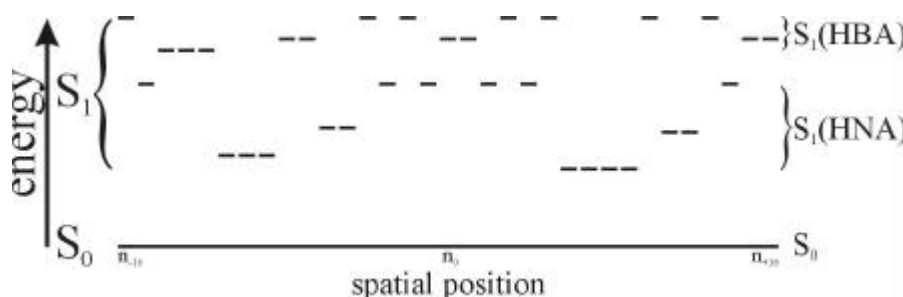


Figure 8.4.07. Generation of an energy continuum in a random copoly(HBA/HNA) molecule of 37 monomeric subunits. HNA subunits are lower in energy than the HBA subunits; neighboring combinations of the same monomer would be lower in energy than a stand alone monomer.

The excited state HNA monomer, or combinations thereof, can then dissipate the energy optically, via fluorescence or phosphorescence, or by thermal coupling. Figures 8.2.01 and 8.2.03 reveal that the copolyester takes an active part in both the fluorescence and phosphorescence optical routes, with the fluorescence strongly predominating over the phosphorescence.

Figure 8.3.04 revealed that there was no apparent emissive wavelength trend with the stretching coefficient α . This is equally true for all of the temperature dependent experiments. Since there is no wavelength dependence of the stretching coefficient α , and hence the degree of disorder within the copolyester, then it can be concluded that the fluorescence emission is not based on any form of energy migration or exciton-exciton annihilation. Additionally, if excited states were mobile or migrating intra or intermolecularly, then the fluorescence emission would be affected by the local HBA rotations, and thus would be readily observed in Figures 8.4.03 and 8.4.04 at the γ phase transition, or around -60 °C.

Figures 8.4.02, 8.4.03, and 8.4.04 clearly indicate the presence of two regions, a temperature independent and temperature dependent region. The transition between the two temperature realms lies in the range of the local HNA torsional motions, which corresponds to the room-temperature β phase transition. The constant temperature independent realm includes the γ phase transition of the local HBA torsional motions. Therefore the HBA rotations do not affect the fluorescence emission within the temperature independent realm. The linearly temperature dependent, Figure 8.4.05, follows the classical Arrhenius equation in which the rate of the relaxation is inversely proportional to the temperature. The Arrhenius fit of the temperature dependent realm revealed an activation energy of 1.357 kcal/mole for the fluorescence emission.

Based on the data presented in this thesis, it is clear that single or adjoining multiple subunits of HNA absorb the 400 nm (3.10 eV) incident energy. If the temperature of the copolyester lies within the temperature independent realm, or less than the temperature of the β phase transition, then the S_1 excited state is coupled to these rotationally frozen, yet vibrationally adjacent nearest HNA neighbors. This vibrational coupling is based on the fact that there exists a fair degree of disorder within the polymer, owing to static energetic and/or structural disorder. Since copoly(HBA/HNA) is a random copolyester, then both of the latter forms of disorder correspond to varying microscopic or local π -orbital conjugation degrees, strengths, and/or lengths. However, the macroscopic response will result in the observation of an average or most probable conjugation strength and/or length with a corresponding distribution therein. Hence the observation of the stretched exponential relaxation and a stretching coefficient α of 0.78 for the fluorescence emission in copoly(HBA/HNA).

Once the temperature of the copoly(HBA/HNA) sample lies within the temperature dependent realm, or greater than the temperature of the β phase transition, then the disorder of the copolyester increases, or α decreases, and the lifetime correspondingly decreases. This observation is consistent with the introduction of the local HNA rotations of the β phase transition. Therefore, the fluorescence emission is not only vibrationally coupled, but also rotationally coupled to the adjacent HNA subunits. The HNA rotations will exhibit various torsional rates based on the classical Boltzmann distribution. The HNA torsional rate distribution will lead to increased disorder of the π -orbital conjugation degrees, strengths, and/or lengths. As the local conjugation strengths and/or

lengths modulate, then throughout the chain length, the conjugation strengths and/or lengths will appear to move throughout the molecular chain, hence owing to dynamic disorder. This dynamic disorder will lower the activation energy of the emission, as compared with the rotationally frozen HNA subunits, to decrease the emission lifetime and exhibit a temperature dependent 1.357 kcal/mole activation energy for the fluorescence emission.

In summary, copoly(HBA/HNA) can produce a strong fluorescence emission that exhibits disordered decay based on the random ordering of the HBA and HNA subunits and the degree, strength, and/or length of the local π -orbital conjugation effects within the copolyester chain. These local conjugation effects will vary in strength and/or length with the introduction of the HNA rotations. These dynamic local conjugation effects will increase the macroscopically observed disorder of the copolyester, and therefore decrease the lifetime of the fluorescence emission decay profiles. The rotation motion of the HNA subunits will induce or stimulate a faster emission, as compared to the rotationally frozen fluorescence emission.

9. Summary and Future Work

In conclusion, copoly(HBA/HNA) possesses a main chain or linear array of partial or full permanent dipole moments colinearly oriented with the nematic or chain direction and connected via π orbital conjugation through the ester bond. The inherent π orbital conjugation strengths and/or lengths are founded on a statistical distribution and the dynamics between adjacent monomeric subunits within copoly(HBA/HNA). The distribution of the conjugation strengths and/or lengths are based, in part, on the planarity of adjacent ring systems, which corresponds to the alignment of the π orbitals of the phenyl and naphthyl rings. Complete alignment of neighboring π orbitals lends itself to the least resistive charge or electron transfer, therefore, the greatest resonance stabilization and conjugation strength and/or length will be observed in the absorption band width, the nonlinear response, and photoluminescence emissions.

Copoly(HBA/HNA) revealed strong evidence of inherent static energetic and structural disorder. This disorder was founded on the basic physical model of the first order stretched exponential decay. For all samples studied less than room temperature, the average stretching coefficient was 0.78 with an average lifetime of 2.30 ns. The HNA torsional motions, or the β phase transition, occurs at room temperature, therefore, the inherent static energetic and/or structural disorder is based on the torsionally frozen HNA monomeric subunits. Fluorescence emission studies performed above room temperature, or after the introduction of the HNA torsional motions, revealed an additional dynamic disorder. The dynamic disorder is temperature dependent and conform to the classical

Arrhenius model. Based on the Arrhenius model, the activation energy of the fluorescence emission is 1.357 kcal/mole. Since the temperature dependent realm occurs at or greater than the HNA torsional phase transition, it can be observed and concluded that the torsional motion of the HNA induce a faster fluorescence emission lifetime, introduce the dynamic disorder, and thus increase the total temperature dependent disorder of the bulk random copolyester material.

Immediate research can be performed, using the instrumentation discussed herein, on samples of copoly(HBA/HNA) that vary in monomeric ratios and molecular chain length. Additionally, a more detailed temperature dependent study can be performed on the fluorescence emission. In general, future work of the optical properties of copoly(HBA/HNA) can extend the understanding of the intra and interchain π orbital overlap, and thus the conjugation effects, strengths, and/or lengths in one and three dimensions, respectively. This type of work may provide a greater understanding of chain-chain registration and the role of the crystallite and amorphous domains found on the nanometer realm. Copoly(HBA/HNA) can be used as a chemically or optically stable material to study the details of static and dynamic disorder currently found within the structure of this material. And finally, new processing techniques of copoly(HBA/HNA) may optimize the mechanical, chemical, and/or optical structure and mechanisms to allow for practical use in electrical or optical devices in harsh environmental conditions, such as outer space.

References

- (1) Symon, K. R. *Mechanics*; Addison-Wesley Publishing Company: Reading, MA, 1971.
- (2) Koenig, J. L. *Spectroscopy of Polymers*; American Chemical Society: Washington, D.C., 1992.
- (3) Bower, D. I.; Maddams, W. F. *The vibrational spectroscopy of polymers*; Cambridge University Press: New York, 1989.
- (4) Cooley, J. W.; Tukey, J. W. *Mathematics of Computation* **1965**, *19*, 297-301.
- (5) Raman, C. V.; Krishnan, K. S. *Nature* **1928**, *121*, 501.
- (6) Wilson, E. B.; Decius, J. C.; Cross, P. C. *Molecular vibrations. The theory of Infrared and Raman Vibrational Spectra.*; Dover Publications, Inc.: New York, 1955.
- (7) Burton, J. C.; Sun, L.; Pophristic, M.; Lukacs, S. J.; Long, F. H. *Journal of Applied Physics* **1998**, *84*, 6268-73.
- (8) Bloembergen, N. *Nonlinear Optics*; The Benjamin/Cummings Publishing Company, Inc.: London, 1982.
- (9) Mills, D. L. *Nonlinear Optics*; Springer-Verlag: New York, 1991.
- (10) Shen, Y. R. *The Principles of Nonlinear Optics*; John Wiley & Sons: New York, 1984.
- (11) Turro, N. J. *Modern Molecular Photochemistry*; The Benjamin/Cummings Publishing Co., Inc.: Reading, MA, 1978.

- (12) Phillips, D. *Polymer Photophysics - luminescence, energy migration, and molecular motion in synthetic polymers.*; Chapman and Hall: New York, 1985.
- (13) Synge, E. H. *Phil. Mag.* **1928**, *6*, 356-62.
- (14) Ash, E. A.; Nichols, G. *Nature* **1972**, *237*, 510-6.
- (15) Fischer, U. C.; Zingsheim, H. P. *J. Vac. Sci. Technol.* **1981**, *19*, 881-5.
- (16) Fischer, U. C. *J. Vac. Sci. Technol.* **1985**, *B3*, 386-90.
- (17) Fischer, U. C.; Durig, U. T.; Pohl, D. W. *Applied Physics Letters* **1988**, *52*, 249-51.
- (18) Fischer, U. C.; Pohl, D. W. *Physical Review Letters* **1989**, *62*, 458-61.
- (19) Harootunian, A.; Betzig, E.; Isaacson, M.; Lewis, A. *Applied Physics Letters* **1986**, *49*, 674-6.
- (20) Betzig, E.; Isaacson, M.; Lewis, A. *Applied Physics Letters* **1987**, *51*, 2088-90.
- (21) Courjon, D.; Sarayedine, K.; Spajer, M. *Optics Communications* **1989**, *71*, 23-8.
- (22) Reddik, R. C.; Warmack, R. H.; Ferrell, T. L. *Physical Review B* **1989**, *39*, 767-770.
- (23) Hulst, N. F. V.; Boer, N. P. D.; Bolge, B. *J. Micr.* **1991**, *163*, 117-30.
- (24) Rather, H. *Springer Tracts in Modern Physics*, 1988; Vol. 111.
- (25) Moller, R.; Albrecht, U.; Boneberg, J.; Koslowski, B.; Leiderer, P.; Drawfeld, K. *J. Vac. Sci. Technol.* **1991**, *B9*, 506-9.
- (26) Specht, M.; Pedarnig, J. D.; Heckl, W. M.; Hänsch, T. W. *Physical Review Letters* **1992**, *68*, 476-9.
- (27) Coombs, J. H.; Gimzewski, J. K.; Reihl, B.; Sass, J. K.; Schlittler, R. R. *J. Micr.* **1988**, *152 Part 2*, 325-36.

- (28) Abraham, D. L.; Veider, A.; Schonenberger, C.; Meier, H. P.; Arant, D. J.; Alvarado, S. F. *Applied Physics Letters* **1990**, *56*, 1564-6.
- (29) Vertikov, A.; Ozden, I.; Nurmikko, A. V. *Applied Physics Letters* **1999**, *74*, 850-2.
- (30) Vertikov, A.; Kuball, M.; Nurmikko, A. V.; Chen, Y.; Wang, S. Y. *Applied Physics Letters* **1998**, *72*, 2645-7.
- (31) Young, R. J.; Lovell, P. A. *Introduction of Polymers*; 2nd ed.; Chapman and Hall: London, 1991; pp 154-6.
- (32) Williamson, R. L.; Miles, M. J. *Journal of Vacuum Science Technology B* **1996**, *14*, 809-11.
- (33) Trautman, J. K.; Macklin, J. J.; Brus, L. E.; Betzig, E. *Nature* **1994**, *369*, 40-2.
- (34) Moers, M. H. P.; Ruiter, A. G. T.; Jalocha, A.; Hulst, N. F. *Ultramicroscopy* **1995**, *61*, 279-83.
- (35) Moers, M. H. P.; Kalle, W. H. J.; Ruiter, A. G. T.; Wiegant, J. C. A. G.; Raap, A. K.; Greve, J.; Grooth, B. G. D.; Hulst, N. F. V. *Journal of Microscopy* **1996**, *182*, 40-5.
- (36) Schoch, B.; Jones, B. E.; Frank, A. *Measurement Science and Technology* **1994**, *5*, 663-6.
- (37) Valaskovic, G. A.; Holton, M.; Morrison, G. H. *Applied Optics* **1995**, *34*, 1215-28.
- (38) Betzig, E.; Trautman, J. K.; Harris, T. D.; Weiner, J. S.; Kostelak, R. L. *Science* **1991**, *251*, 1468-70.

- (39) McCulloch, S.; Uttamchandani, D. *Measurement Science and Technology* **1995**, *6*, 1157-62.
- (40) Bozhevolnyi, S. I.; Keller, O.; Xiao, M. *Applied Optics* **1993**, *32*, 4864-8.
- (41) Bozhevolnyi, S. I.; Smolyaninov, I. I.; Keller, O. *Applied Optics* **1995**, *34*, 3793-9.
- (42) Toledo-Crow, R.; Yang, P. C.; Vaez-Iravani, M. *Applied Physics Letters* **1992**, *60*, 2957-9.
- (43) O'Shea, S. J.; Welland, M. E. *Applied Physics Letters* **1992**, *60*, 2356-8.
- (44) Tarrach, G.; Bopp, M. A.; Zeisel, D.; Meixner, A. J. *Review of Scientific Instruments* **1995**, *66*, 3569-75.
- (45) Sadrid, D. *Scanning Force Microscopy*; Oxford University Press: New York, 1994.
- (46) Froehlick, F. F.; Milster, T. D. *Applied Physics Letters* **1997**, *70*, 1500-1502.
- (47) Moyer, P. J.; Paesler, M. A. *Proc. SPIE* **1993**, 1855.
- (48) Burnham, N. A.; Cotton, R. J. *Scanning Tunneling Microscopy and Spectroscopy: Theory, Techniques, and Applications*; VCH: New York, 1993.
- (49) Erlandsson, R.; McClelland, G. M.; Mate, C. M.; Chiang, S. J. *Vac. Sci. Technol.* **1988**, *A6*, 266.
- (50) Cox, M. K. *Liquid crystal polymers*; Pergamon Press: New York, 1987; Vol. 1, No. 2.
- (51) Prasad, P. N.; Williams, D. J. *Introduction to nonlinear optical effects in molecules and polymers*; John Wiley & Sons, Inc.: New York, 1991.

- (52) Donald, A. M.; Windle, A. H. *Liquid Crystalline Polymers*; Cambridge University Press: Great Britain, 1992.
- (53) Nicolson, T. M.; Mackley, M. R.; Windle, A. H. *Polymer* **1992**, *33*, 434-5.
- (54) Isayev, A. I.; Kyu, T.; Cheng, S. Z. D. *Liquid-Crystalline Polymer Systems, Technological Advances*; American Chemical Society: Washington, D.C., 1996; Vol. 632.
- (55) Blackwell, J.; Gutierrez, G. A.; Chivers, R. A. *Macromolecules* **1984**, *17*, 1219-1224.
- (56) Viney, C.; Mitchell, G. R.; Windle, A. H. *Mol. Cryst. Liq. Cryst.* **1985**, *129*, 75-108.
- (57) Hofmann, D.; Schneider, A. I.; Blackwell, J. *Polymer* **1994**, *35*, 5603-5610.
- (58) Spontak, R. J.; Windle, A. H. *Journal of Polymer Science: Part B: Polymer Physics* **1992**, *30*, 60-9.
- (59) Kaito, K.; Kyotani, M.; Nakayama, K. *Journal of Polymer Science: Part B: Polymer Physics* **1993**, *31*, 1099-1108.
- (60) Ruiten, J. v.; Meier, R. J.; Hahn, C.; Mosell, T.; Sariban, A.; Brickmann, J. *Macromolecules* **1993**, *26*, 1555-63.
- (61) Watanabe, T.; Miyata, S.; Furukawa, T.; Takezoe, H.; Nishi, T.; Sone, M.; Migita, A.; Watanabe, J. *Japanese Journal of Applied Physics* **1996**, *35*, L505-7.
- (62) Hermann, J. P.; Ducuing, J. *Journal of Applied Physics* **1974**, *45*, 5100-2.
- (63) Green, D. I.; Orchard, G. A. J.; Davies, G. R.; Ward, I. M. *Journal of Polymer Science: Part B: Polymer Physics* **1990**, *28*, 2225-31.
- (64) Troughton, M. J.; Davies, G. R.; Ward, I. M. *Polymer* **1989**, *30*, 58-62.

- (65) Takase, Y.; Mitchell, G. R.; Odajima, A. *Polymer Communications* **1986**, *27*, 76.
- (66) Alhaj-Mohammed, M. H.; Davies, G. R.; Jawad, S. A.; Ward, I. M. *Journal of Polymer Science: Part B: Polymer Physics* **1988**, *26*, 1751-60.
- (67) Kalika, D. S.; Yoon, D. Y. *Macromolecules* **1991**, *24*, 3404-12.
- (68) Cheng, S. Z. D.; Janimak, J. J.; Zhang, A.; Zhou, Z. *Macromolecules* **1989**, *22*, 4240-6.
- (69) Flores, A.; Ania, F.; Calleja, F. J. B.; Ward, I. M. *Polymer* **1993**, *34*, 2915-2920.
- (70) McCullagh, C. M.; Blackwell, J.; Jamieson, A. M. *Macromolecules* **1994**, *27*, 2996-3001.
- (71) McCullagh, C. M.; Yu, Z.; Jamieson, A. M.; Blackwell, J.; McGervey, J. D. *Macromolecules* **1995**, *28*, 6100-7.
- (72) Hummel, J. P.; Flory, P. J. *Macromolecules* **1980**, *13*, 479-84.
- (73) Dulcic, A.; Sauteret, C. *J. Chem. Phys.* **1978**, *69*, 3453-7.
- (74) Terhune, R. W.; Maker, P. D.; Savage, C. M. *Physical Review Letters* **1965**, *14*, 681-4.
- (75) Clays, K.; Persoons, A. *Physical Review Letters* **1991**, *66*, 2980-3.
- (76) Clays, K.; Persoons, A. *Review of Scientific Instruments* **1992**, *63*, 3285-9.
- (77) Ray, P. C.; Das, P. K. *J. Phys. Chem.* **1995**, *99*, 17891-5.
- (78) Ray, P. C.; Das, P. K. *J. Phys. Chem.* **1996**, *100*, 15631-3.
- (79) Ray, P. C. *Chemical Physics Letters* **1996**, *248*, 27-30.
- (80) Ray, P. C.; Das, P. K.; Ramasesha, S. *J. Chem. Phys.* **1996**, *105*, 9633-9.
- (81) Dulcic, A.; Flytzanis, C.; Tang, C. L.; Pepin, D.; Fetizon, M.; Hoppilliard, Y. *J. Chem. Phys.* **1981**, *74*, 1559-63.

- (82) Asada, T. *Molecular Crystals and Liquid Crystals* **1994**, 254, 125-35.
- (83) Furukawa, T.; Ishikawa, K.; Takezoe, H.; Fukuda, A.; Watanabe, T.; Miyata, S.; Nishi, T.; Sone, M.; Watanabe, J. *Nonlinear Optics* **1996**, 15, 167-70.
- (84) Furukawa, T.; Takezoe, H.; Nishi, T.; Mitsukuchi, T.; Migita, A.; Watanabe, J.; Watanabe, T.; Miyata, S. *Molecular Crystals and Liquid Crystals* **1997**, 299, 105-9.
- (85) Asada, T.; Tanaka, H. "Nonlinear optical properties of the main-chain type liquid crystalline polymers"; SPIE, 1997.
- (86) Butzback, G. D.; Wendorff, J. H.; Zimmermann, H. J. *Polymer* **1986**, 27, 1337-44.
- (87) Jansen, J. A. J.; Paridaans, F. N.; Heynderickx, I. E. J. *Polymer* **1994**, 35, 2970-6.
- (88) Lukacs, S. J.; Cohen, S. M.; Long, F. H. *Journal of Physical Chemistry B* **1999**, 103, 6648-6652.
- (89) Williams, G.; Watts, D. C. *Trans. Faraday Soc.* **1970**, 66, 80.
- (90) Williams, G.; Watts, D. C.; Dev, S. B.; North, A. M. *Trans. Faraday Soc.* **1977**, 67, 1323.
- (91) Gilard, P.; deBast, J. *Advances in Glass Technology*; Plenum: New York, 1962; Vol. pg. 442.
- (92) Kolrausch, F. *Pogg. Ann. Phys.* **1863**, 119, 352.
- (93) Shlesinger, M. F. *Ann. Rev. Phys. Chem.* **1988**, 39, 269-90.
- (94) Shlesinger, M. F.; Klafter, J. *J. Phys. Chem.* **1989**, 93, 7023-6.
- (95) Klafter, J.; Shlesinger, M. F.; Zumofen, G. *Physics Today* **1996**, 33-9.
- (96) Klafter, J.; Shlesinger, M. F. *Proc. Natl. Acad. Sci.* **1986**, 83, 848-51.

- (97) Bendler, J. T.; Shlesinger, M. F. *J. Phys. Chem.* **1992**, *96*, 3970-3.
- (98) Pavesi, L.; Ceschini, M. *Physical Review B* **1993**, *48*, 17625-8.
- (99) Kauffmann, H. F.; Mollay, B.; Weixelbaumer, W.-D.; Burbaumer, J.; Riegler, M.; Meisterhofer, E.; Aussenegg, F. R. *J. Chem. Phys.* **1986**, *85*, 3566-84.
- (100) Muller-Horsche, E.; Haarer, D.; Scher, H. *Physical Review B* **1987**, *35*, 1273-80.
- (101) Tao, W. C.; Frank, C. W. *J. Phys. Chem.* **1989**, *93*, 776-84.
- (102) Mollay, B.; Lemmar, U.; Kersting, R.; Mahrt, R. F.; Kurz, H.; Kauffmann, H. F.; Bäessler, H. *Physical Review B* **1994**, *50*, 10769-79.
- (103) Kersting, R.; Mollay, B.; Rusch, M.; Wenisch, J.; Leising, G.; Kauffmann, H. F. *J. Chem. Phys.* **1997**, *106*, 2850-64.
- (104) Kersting, R.; Lemmer, U.; Mahrt, R. F.; Leo, K.; Kurz, H.; Bäessler, H.; Gobel, E. O. *Physical Review Letters* **1993**, *70*, 3820-3.
- (105) Bäessler, H.; Brandl, V.; Deussen, M.; Gobel, E. O.; Kersting, R.; Kurz, H.; Lemmer, U.; Mahrt, R. F.; Ochse, A. *Pure and Applied Chemistry* **1995**, *67*, 377-95.
- (106) Bendler, J. T.; Shlesinger, M. F. *Physics Today* **1989**, S31-2.
- (107) Scher, H.; Shlesinger, M. F.; Bendler, J. T. *1991* **1991**, 26-34.
- (108) Lindsey, C. P.; Patterson, G. D. *Journal of Chemical Physics* **1980**, *73*, 3348-57.
- (109) Montroll, E. W.; Bendler, J. T. *Journal of Statistical Physics* **1984**, *34*, 129-62.
- (110) Lemmer, U.; Mahrt, R. F.; Wada, Y.; Greiner, A.; Bäessler, H.; Gobel, E. O. *Chemical Physics Letters* **1993**, *209*, 243-6.
- (111) Barth, S.; Bäessler, H. *Physical Review Letters* **1997**, *79*, 4445-8.

Curriculum Vitae

Stephen J. Lukacs Jr.
22 Marvin Lane
Piscataway, NJ 08854
(732) 878 – 2227

Education

- 1991 University of Central Florida, Three B.S. Degrees.
 B.S. Microbiology/Molecular Biology.
 B.S. Chemistry.
 B.S. Physics, minor in Mathematics.
- 1999 Ph.D. Candidate in Physical Chemistry at Rutgers University.
 Advisor: Frederick H. Long.

Experience, Teaching

- 1994-1995 Chemistry teacher at St. Peter's High School in New Brunswick, NJ.
- 1993-1999 Teaching Assistant at Rutgers University. Courses taught include General Chemistry Recitation and Laboratory (3 years), Analytical (2 years), Instrumental (2 years), and Physical Chemistry (2 years). The General Chemistry Recitation is a special Rutgers course designed to be an entry level class for students with little or no background in mathematics and science.

Experience, Work

- 1985-1992 Gained experience in several university and industrial research laboratories and computer facilities while completing my B.S. degrees.
- 1993-1999 Rutgers University, Laser Spectroscopy, AFM, and NSOM.
- 1991-Present Infinite Quanta, Inc., Head Database Developer and Programmer.

Publications

- Lukacs, S.L. Cohen, S.M., Long, F.H., *Journal of Physical Chemistry*, Optical properties of a liquid-crystalline random copolyester, **1999**, 103, 6648-6652.
- Burton, J.C., Sun, L., Pophristic, M., Lukacs, S.J., Long, F.H., *Journal of Applied Physics*, Spatial characterization of doped SiC wafers by Raman spectroscopy, **1998**, 84(11), 6268-6273.
- U.S. Copyright. Fleet Dynamics Client/Server 32 version 2. **1999**.
- U.S. Copyright. Fleet Dynamics Client/Server 32 version 1. **1998**.
- U.S. Copyright. Fleet Dynamics. **1994**.
- U.S. Patent #4,772,274. Feminine Hygiene Apparatus. **1988**.
- Chow, L., Lukacs, S., Hopkins, K., *European Journal of Physics*, "Speed of Light" measurement using BaF₂ scintillation detectors, **1994**, 15, 49-52.